

# STARS

University of Central Florida  
STARS

---


Electronic Theses and Dissertations, 2004-2019

---

2017

## Charge and Spin Transport in Low-Dimensional Materials

Amin Ahmadi  
*University of Central Florida*

 Part of the [Physics Commons](#)

Find similar works at: <https://stars.library.ucf.edu/etd>

University of Central Florida Libraries <http://library.ucf.edu>

This Doctoral Dissertation (Open Access) is brought to you for free and open access by STARS. It has been accepted for inclusion in Electronic Theses and Dissertations, 2004-2019 by an authorized administrator of STARS. For more information, please contact [STARS@ucf.edu](mailto:STARS@ucf.edu).

---

### STARS Citation

Ahmadi, Amin, "Charge and Spin Transport in Low-Dimensional Materials" (2017). *Electronic Theses and Dissertations, 2004-2019*. 5406.

<https://stars.library.ucf.edu/etd/5406>



CHARGE AND SPIN TRANSPORT IN LOW-DIMENSIONAL MATERIALS

by

AMIN AHMADI  
M.S. University of Central Florida, 2013

A dissertation submitted in partial fulfilment of the requirements  
for the degree of Doctor of Philosophy  
in the Department of Physics  
in the College of Sciences  
at the University of Central Florida  
Orlando, Florida

Spring Term  
2017

Major Professor: Eduardo Mucciolo

© 2017 Amin Ahmadi

## **ABSTRACT**

My research has been focused on two main areas. First, electronic transports in chiral carbon nanotubes in the presence of charged adatoms. To study such systems we employed recursive Greens function technique to evaluate the conductance using the Landauer formula. Comparing with the experimental data, we determined the effective amplitude and the range of scattering potentials. In addition, using a similar approach we explained qualitatively an unusual conductance feature in a metallic carbon nanotube. The second part of my study was concerned to the dynamical spin injection and spin currents in low-dimensional materials. We have developed an atomistic model to express the injected spin current in terms of the systems Greens function. The new formulation provides a framework to study the spin injection and relaxation of a system with an arbitrary structure.

To my parents, with love.

## **ACKNOWLEDGMENTS**

I would like to express the deepest appreciation to my advisor Prof. Eduardo Mucciolo, who has the attitude and the substance of a genius. Without his encouragement, advice and persistent helps, this dissertation would not have been possible. I appreciate all his contributions of time, patience and ideas to make my Ph.D. experience productive.

I do not know how to express my sincere gratitude to my family, especially my parents. They taught me to walk and they were delighted when I took the first shaky steps, they taught me to run and encouraged me to run faster, their hearts were full of joy when I held a pen in my hand for the first time. I can not imagine a more passionate teacher and mentor than my mom and dad who have sacrificed everything to see our happiness. I am deeply thankful to my wonderful sister and brother, Elaheh and Mahdi who have always been encouraging. I am very lucky to be your brother.

And most of all to my loving, supportive, encouraging, and patient wife Marjan whose faithful support during these years of this Ph.D. is so appreciated. Words cannot describe how lucky I am to have her in my life. I love you, and look forward to our lifelong journey!

## TABLE OF CONTENTS

LIST OF FIGURES . . . . .	ix
CHAPTER 1: INTRODUCTION . . . . .	1
CHAPTER 2: AD-ATOM SCATTERING STRENGTH . . . . .	6
Motivation . . . . .	6
Approach and Formulation . . . . .	8
The Lead Green's Function and Decimation Technique . . . . .	9
Recursive Algorithm . . . . .	11
Implementation . . . . .	14
Testing the Code . . . . .	16
Where is the Fermi Level? . . . . .	18
Impurity Potential . . . . .	20
Results . . . . .	21
Summary . . . . .	22
CHAPTER 3: UNUSUAL CONDUCTANCE OF METALLIC CNT . . . . .	27

Motivation . . . . .	27
Metallic CNT, Test and Simulations . . . . .	29
Physical Interpretation: Robustness of the First Band . . . . .	34
Summary . . . . .	38
<b>CHAPTER 4: DYNAMICAL SPIN INJECTION IN LOW-DIMENSIONAL MATERIALS</b>	<b>39</b>
Introduction . . . . .	39
FM/Gr FMR Measurements and Standard Theory of Dynamical Spin Injection . . . . .	42
One-Dimensional Model . . . . .	44
Equations of Motion . . . . .	46
Fourier Transform of the Equations of Motion . . . . .	49
Charge and Spin Currents . . . . .	50
Spin Pumping in the Absence of a Chain . . . . .	54
Perturbative Expansion in $\Omega_{\perp}$ . . . . .	59
Spin Current Components . . . . .	60
Interface Parameters . . . . .	62
Spin Pumping with a Finite Chain . . . . .	64
Current in the Presence of Spin-Orbit Coupling . . . . .	66



Extension to Two-Dimensional Systems . . . . .	73
Summary and Discussion . . . . .	78
APPENDIX A: SUPPLEMENTARY MATERIALS . . . . .	80
Reservoir Green's Function . . . . .	81
Noise-Like Correlator . . . . .	81
$s$ -Component of the Spin Current . . . . .	84
Spin Current for 2D Systems . . . . .	85
LIST OF REFERENCES . . . . .	88

## LIST OF FIGURES

<p>Figure 2.1: The experimental conductance as a function of gate voltage for a <math>6\ \mu\text{m}</math> (7,6) carbon nanotube segment in ultra high vacuum. (left) Hole conductance at 9 K and (right) electron conductance at 16 K before and after dosing with potassium. Data first presented in Ref. [1]. . . . .</p>	6
<p>Figure 2.2: The experimental length dependence of the resistance for multiple devices (left) at <math>V_g - V_{\text{onset}} = -60\ \text{V}</math> and (right) at <math>V_g - V_{\text{onset}} = 60\ \text{V}</math> before and after dosing with potassium. Data first presented in Ref. [1]. . . . .</p>	7
<p>Figure 2.3: By slicing the device region between two leads, the full Green’s function can be calculated efficiently. The computation cost scales linearly with the length of device. . . . .</p>	11
<p>Figure 2.4: The flowchart of the recursive Green’s function algorithm. . . . .</p>	14
<p>Figure 2.5: The band structure of a semiconductor (7, 6) CNT. The minimum main band gap appears at <math>\frac{ka}{2} = \frac{\pi}{3}</math>. . . . .</p>	16
<p>Figure 2.6: (a) The quantum conductance of a pristine (7, 6) CNT as a function of energy evaluated by the recursive Green’s function technique. One quantum of conductance is added at every opening of a nw channel. (b) The DOS of the same CNT. The positions of the van Hove singularities exactly coincide with the opening of conducting channels in Fig 2.5. . . . .</p>	17
<p>Figure 2.7: By integrating over the DOS from the neutrality point to the Fermi level, one can find the number of carriers for a given gate voltage. . . . .</p>	19

Figure 2.8: The single impurity analysis for negative carriers. . . . .	24
Figure 2.9: The single impurity analysis for positive carriers. . . . .	25
Figure 2.10: To explore possible ranges and amplitudes for the simulation of adatoms, we performed a series of calculations for a single impurity placed on a CNT segment. The data points are the comparison of the calculation with the experimental data at energy $E = \pm 1.5 \text{ eV}$ . At short range, the data point for electrons and holes are inconsistent, but starting around $\xi = 18 \text{ \AA}$ convergence indicates possible range and amplitude, which are then used to for further simulations. . . . .	26
Figure 2.11: The resistance of electrons and holes in a (7, 6) chiral CNT in the presence of charged impurities. The scattering strength of positively charged adatoms is $7.32 \pm 0.42 \text{ k}\Omega$ for holes and $0.31 \pm 0.01 \text{ k}\Omega$ for electrons. . . . .	26
Figure 3.1: The experimental data for a quasi-metallic CNT (22, 4) show an unusual conductance versus gate voltage behavior. (left) A suppression around the Dirac point is expected due to the curvature-induced gap. However, by increasing the gate voltage, another suppression appears. (right) The unusual form of conductivity confirms that the feature is intrinsic, independent of length and contacts. . . . .	28
Figure 3.2: The band structure of a metallic (22, 4) CNT. . . . .	29
Figure 3.3: The quantized conductance and the density of state of a pristine quasi-metallic (22, 4) CNT. . . . .	30

Figure 3.4: The conductance of a metallic (22, 4) CNT in the presence of adatoms with scattering range $\xi = 9 \text{ \AA}$ (left) and $\xi = 18 \text{ \AA}$ (right). The results were produced by averaging over 400 samples. . . . .	31
Figure 3.5: (left) The conductance for different length of a metallic (22, 4) CNT in the presence of positive impurities. Here the amplitude and the range of impurities are $V_0 = 0.4t$ and $\xi = 8 \text{ \AA}$ . (right) The conductance of a metallic (22, 4) CNT in the presence of adatoms with different scattering range. . . . .	33
Figure 3.6: (left)The effect of defects on the conductance of a metallic (22, 4) CNT. In contrast to long-range impurities, defects affect the electronic transport in the first band and it is symmetric between electrons and holes. (right)The resistivity of a metallic CNT in the presence of both long range impurities and defects. . . . .	34
Figure 3.7: (left) A massless particle encounters a rectangular barrier or well in analogy of the scattering of positive and negative carriers in presence of a positive charged adatom. (right) The transmission probability for positive and negative carriers are presented as a function of the effective range $\xi$ of impurities. . . . .	36
Figure 4.1: (left)A schematic structure of dynamical spin injection in FM/Gr setup. A part of graphene sheet is covered by a FM. A time-dependent magnetic field compensates the damping of the precession of the magnetization in FM. (right) The FMR measurements on three setups Py, Py/Gr, and Py/Gr(extended) confirms that an extra damping of magnetization precession in FM is induced by pumped spin current into the graphene layer. . . . .	40

Figure 4.2: An schematic presentation of the theory of dynamical spin injection into NM. In this theory the FM region is act as an dynamical scatterer between two metallic reservoirs. If the spin relaxation rate is smaller than the spin injection rate in NM, a backflow spin current decrease the damping of magnetization precession. . . . .	44
Figure 4.3: Scheme of the one-dimensional model of spin pumping from a magnetic site representing a ferromagnet (FM) to a nonmagnetic (NM) chain connected to a reservoir. . . . .	45
Figure 4.4: Two electrons with opposite spin states travel in opposite direction. The net charge current is zero, but two units of angular momentum are transferred to the right. . . . .	51
Figure 4.5: (upper panel) Spin-diagonal components of the Green's function across the chain, $G_{N,s;0,s}$ , in a clean (translation invariant) chain in the absence of spin-orbit coupling as a function of energy. (lower panel) The dependence of the $z$ -component of the spin current on the reservoir's Fermi energy. Both plots were obtained using parameters value such that $\gamma_\alpha^2 \Omega_\perp^2 \Omega = 2$ . . . . .	71
Figure 4.6: (left) Diagonal spin component of the Green's function across the chain, $G_{N,\uparrow;0,\uparrow}$ , as a function of energy, in the presence of a random spin-dependent site potential. The chain length is 300 sites and the Green's function is averaged over 10 and 50 realizations of the random potential. (right) The off-diagonal spin component of the Green's function, $G_{N,\uparrow;0,\downarrow}$ . . . . .	72

Figure 4.7: Average dc spin current current injected into the reservoir as a function of chain length in the presence of spin-dependent, random on-site potential. The data points are obtained after averaging over 300 samples to minimize quantum interference fluctuations. The solid lines are fittings to the data. The field  $a_z$  varied within the range  $[0, 0.1t]$  while the  $a_x$  field range changed for each data set, as indicated in the legend. The simulations are performed at  $E = 0$  (middle of the band). . . . . 73

Figure 4.8: The two-dimensional FM/NM/reservoir system. The magnetic region comprises a column of sites whose magnetizations are synchronized. The non-magnetic sheet is decomposed in  $N$  slices. . . . . 75

## CHAPTER 1: INTRODUCTION

Among the greatest discoveries of twentieth century two stand out: the theory of relativity and quantum mechanics. Even though both give us better understanding of the world, the theory of relativity barely touches our day-to-day life, except for the precision that is needed for GPS navigation systems. On the other hand, applications of quantum mechanics are more ubiquitous and are powering the advance of the modern way-of-life further. The CPU of a smartphone that fits in our pocket can beat the speed, price, and size of vacuum-tube-era computer, thanks to exploitation of quantum phenomena in materials used in the computing elements.

Since the invention of the transistor at Bell Laboratories, the search for new materials for faster and cheaper computing units, and increasing memory reliability and capacity, has never stopped. Among the different elements of periodic table, carbon, the building block of life on Earth, shows fascinating electronic properties. Different forms and structures of carbon such as diamond, graphite, fullerene, and, most recently, carbon nanotubes and graphene, always captured scientists' attention in their quest to advance our understanding of solid-state physics. Although the quantum mechanical features are already manifest in confined electronic system fabricated with a thin layer of Si on SiO<sub>2</sub> [2], the first truly two-dimensional (2D) and one-dimensional (1D) systems were realized after the discovery of graphene [3] and carbon nanotubes [4].

This dissertation focuses on electronic and spin transport in low-dimensional materials. Although carbon nanotubes (CNTs) have been around and well studied for more than two decades [5], there is still more to understand due to their fascinating atomic and electronic structure. Besides their unique chemical, mechanical, and optical properties, they can behave as a metal or a semiconductor with different band gaps, depending on their chirality and diameter. One interesting aspect of CNTs is that their conductance changes in the presence of different adatoms [6]. This discovery provides

a new application of CNTs as a high-precision sensor device for detecting chemical elements.

The first part of my dissertation is devoted to the electronic properties of semiconductor and metallic CNTs in the presence of charged adatoms. The main idea behind these studies was to measure and quantify the scattering strength of positive and negative carriers of a single-wall CNT in the presence of charged adatoms [1]. In Chapter 2, I start with a brief description of the measurements and experimental results, then present the model that I chose for studying the problem. For a full quantum mechanical calculation I use the Landauer-Büttiker formula to evaluate the conductance. The relation between the conductance and the system's Green's function is presented in Sec. 2. To be able to compute the Green's function of a large system efficiently, I introduce the recursive Green's function (RGF) technique in Sec. (2). To explore a wide range of impurities' amplitude and range, I performed many calculations for short segments of a CNT with a single impurity. Long segments were simulated as well and the results of these simulations compared to experimental data obtained by the Ishigami group at UCF. Based on these calculations we were able to determine the effective amplitude and range of the impurities present in the experimental device.

In Chapter 3, a novel study of metallic CNT is presented. An unusual conductance behavior has been observed experimentally in quasi-metallic CNTs (22,4) by the Ishigami group. I believe that this feature is related to the Dirac nature of the charge carriers around the neutrality point of a metallic CNT. For this studies, I employed the same numerical approach that was used in Chapter 2. I examined the effect of long- and short-range impurities on the conductivity of a metallic CNT. Short- and long-range impurities affect the first and higher conduction bands differently due to the linear dispersion of the first band. I show that the unusual shape of the conductance versus gate voltage curve in metallic CNT is related to the presence of impurities and defects. I end this Chapter by presenting a toy model for the scattering of a massless carrier through a barrier to better understanding the underlying physics.



The second part of my dissertation is a formulation of dynamical spin injection in a low dimensional system. By shrinking the size of Si MOSFET transistors we are approaching Moore's law limit. Yet, the energy consumption of today CPUs is still much higher than the minimum energy that was proposed by Landauer [7]. Thus, there is plenty of space for developing more efficient and faster technologies. Spintronics seems to be the next stages of evolution in computing.

A reliable source of spin current is the most important building block of spintronics. Among different techniques such as nonlocal spin injection, spin Hall effect, and ferromagnet filtering, dynamical spin pumping by means of magnetization precession has attracted a lot of attention [8, 9, 10, 11, 12, 13]. A series of measurements and experimental realizations have proved the plausibility and efficiency of this technique. In ferromagnet/nonmagnet (FM/NM) materials, the injected current can be detected indirectly via the broadening of ferromagnetic resonance (FMR) or directly via the conversion of spin currents into lateral electric potentials by the inverse spin Hall effect.

In 2012, the dynamical spin injection in a hybrid 2D system of combining a ferromagnet and graphene was proposed and observed experimentally [14]. The unique electronic properties of a graphene sheet, such as high mobility, tunable carrier density with applied gate voltage, and local the enhancement of spin-orbit coupling by defects and adatoms, encouraged extending dynamical spin injection to such a 2D system.

The standard theory developed to describe the spin injection in metals by a resonant ferromagnet was developed by Tserkovnyak and Brataas [15, 16, 8]. In this theory, the amount of spin currents injected into the NM metal is quantified in terms of a parameter called *mixing conductance*. The mixing conductance is a sum of the opposite-spin reflection coefficients between different conducting channels.

As reported in Ref. [17], the mixing conductance extracted from the Py/graphene experiments was comparable to the value that found for Py/Pt and Py/Pd samples (here Py stands for permalloy).

However, following the theory of Tserkovnyak and Brataas, the mixing conductance is roughly proportional to the number of conducting channels at the interface; since the interface between the FM and the graphene protruding away from the FM is one-dimensional, the mixing conductance found in the experiments is orders of magnitude higher than expected. The spin-scattering rate in a graphene layer is expected to be rather low, lower than the spin injection rate. Based on an argument presented in Ref. [15], this should cause a spin density to build up near the NM layer; the difference of chemical potentials for spin up and down then generates a backflow spin current that decreases the effective mixing conductance. The backflow that was estimated theoretically for a graphene layer was large enough to make the effective mixing conductance negative! Thus, it was difficult to reconcile an analysis based on the scattering theory with the experimental data.

To address these problems I developed an atomistic formulation of the injected current in terms of the Green's function of the NM region. The atomic structure of the NM region, its geometry, as well as the presence of adatoms or any other mechanism that can induce spin-orbit interaction can be readily taken into account in this formalism. The spin current relaxation and injection can be evaluated at the same time. Another advantage of this Green's function-based approach is the possibility to use recursive methods to achieve fast and efficient computations of large systems.

In Chapter 4, I present this novel formulation of dynamical spin injection due to the proximity of a 2D system to a FM with precessing magnetization. In Sec. 4, I introduce a 1D chain of sites with a time-dependent boundary condition to model the spin injection. The equations of motion for this system are presented in Sec. 4. Then I discuss an appropriate definition of spin current in Sec. 4 and develop an expression for the spin current in terms of the system Green's function. The simple example of a zero-length chain is presented to provide some insight into the formalism. In Sec. 4 the spin current for a finite-length chain in the presence of spin scattering processes is given in Sec. 4. Some simulations are presented in Sec. 4 to illustrate the analytical results. Finally, in Sec. 4 we extend the formalism to 2D systems. Some long derivations of Chapter 4 are presented in the

appendices. In Appendix A, the decoupled reservoir Green's function is given. Appendix A is devoted to the derivation of the correlation between particle operators of the reservoir. Appendices A, and A contain the details of the derivation of the spin current in 1D chain and 2D systems.

## CHAPTER 2: AD-ATOM SCATTERING STRENGTH

### Motivation

A better understanding of electronic transport properties of CNTs in the presence of charged adatoms can pave the way toward CNT-based sensing technology. While previous studies have mainly focused on the effect of charged impurities on the width of Schottky barrier on and screening effects [18, 19], the interaction of carriers with the adatoms has been usually neglected. The initial motivation for our study came after a series of measurements performed on single-wall carbon nanotube (SWCNT) [1].

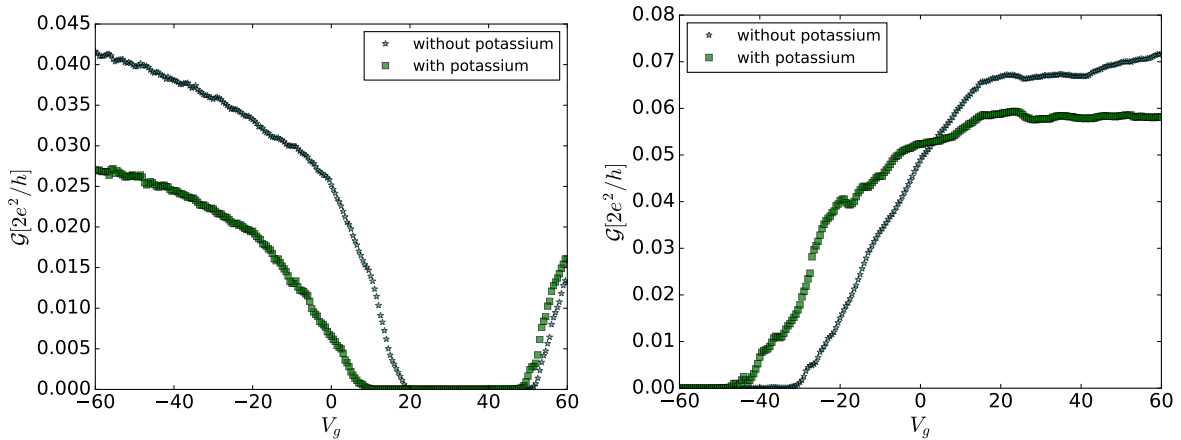


Figure 2.1: The experimental conductance as a function of gate voltage for a  $6 \mu\text{m}$  (7,6) carbon nanotube segment in ultra high vacuum. (left) Hole conductance at 9 K and (right) electron conductance at 16 K before and after dosing with potassium. Data first presented in Ref. [1].

In these experiments, a few charged potassium adatoms were placed on a CNT of known chirality. The type and density of carriers were controlled by an applied gate voltage; see Fig. 2.1 for a plot of their conductance versus gate voltage before and after dosing with potassium. Then, by evaluating

the resistivity from the experimental data, the scattering strength per adatom was estimated. The known chirality of the CNT, which was determined using Rayleigh scattering spectroscopy [20] allowed one to determine the actual band structure and conducting channels, thus guiding the theoretical calculations. The scattering strength that was obtained from the measurements was 37 times stronger for holes than for electron carriers [1].

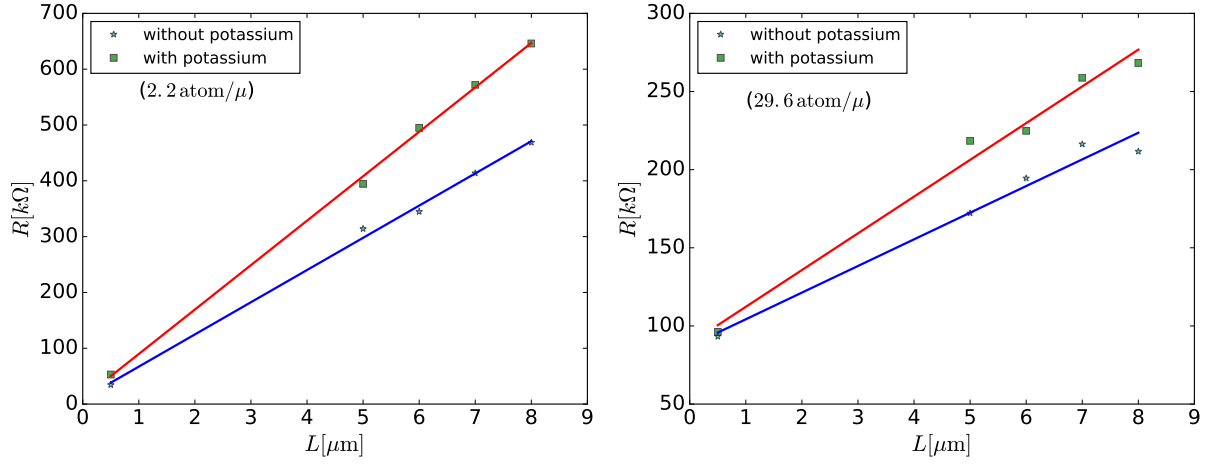


Figure 2.2: The experimental length dependence of the resistance for multiple devices (left) at  $V_g - V_{\text{onset}} = -60 \text{ V}$  and (right) at  $V_g - V_{\text{onset}} = 60 \text{ V}$  before and after dosing with potassium. Data first presented in Ref. [1].

In this Chapter, we start by briefly introducing the Landauer formulation used to evaluate the dc conductance. Next, the relation between system's full Green's function and its transmission matrix is provided. A decimation technique is employed to emulate the metallic lead and a recursive algorithm is implemented to calculate the full Green's function. The code is tested and benchmarked against analytical results before being used to the problem in hand. At the end of the Chapter, we compare the results from simulations to those from the measurements. From this comparison, we determine the amplitude and range of the scattering potential in semiconductor (7, 6) CNT.

## Approach and Formulation

A single-band *tight-binding model* is chosen to describe the electronic transport in SWCNTs, with the Hamiltonian defined as

$$\mathcal{H} = - \sum_{\langle ij \rangle} [t_{ij}|i\rangle\langle j| + H.c.] + \sum_i V_i|i\rangle\langle i|, \quad (2.1)$$

where  $t_{ij}$  is the hopping amplitude between the nearest neighbor sites  $i$  and  $j$ , and  $V_i$  is the on-site energy modulated by the presence of impurities or an applied gate voltage. The CNT is placed between two metallic leads which can be modeled using two semi-infinite lattices with the same structure of the CNT to eliminate any extra scattering at the lead interface due to channel mismatch [21].

To evaluate the electronic transport across the system in the presence of a small applied bias (i.e, in the linear regime), we use the Landauer-Bütiker formulation [22, 23] which describes the conductance in terms of the transmission probability of the device,

$$\mathcal{G} = \frac{2e^2}{h} \text{Tr}_c [t^\dagger t], \quad (2.2)$$

where the subscript  $c$  indicates a sum over conducting channels and  $t(t')$  is the transmission matrix across the system from left to right (right to left). Combining with the reflection matrices  $r$  ( $r'$ ), a  $S$ -matrix can be constructed,

$$S = \begin{pmatrix} r & t' \\ t & r' \end{pmatrix}. \quad (2.3)$$

The elements of the  $S$  matrix in the tight-binding basis are given in terms of the system's full

retarded Green's function [24],

$$S_{ab}(E) = -\delta_{ab} + i\hbar \frac{\sqrt{v_a v_b}}{a_0} \sum_{i \in p} \sum_{j \in q} \chi_a^*(i) G_{qp}^r(i, j) \chi_b(j), \quad (2.4)$$

where  $v_c$  is the longitudinal propagation velocity and  $\chi_c(i)$  is the transverse wavefunction of the leads in channel  $c$ . Here, the sums run over all sites at the contacts  $p$  and  $q$  where the propagating channels  $a$  and  $b$  are defined, respectively. For, such a systems, the conductance can also be expressed as

$$\text{Tr}_c [t^\dagger t] = \text{Tr}_s [\Gamma_L G_{LR}^r \Gamma_R G_{RL}^a], \quad (2.5)$$

where the *level width* matrices  $\Gamma$  are given by

$$\Gamma_{L,R} = i \left[ \Sigma_{L,R}^r(E) - \Sigma_{L,R}^{r\dagger}(E) \right] \quad (2.6)$$

which involves retarded *surface self-energies*,

$$\Sigma_{L,R}^r(E) = u_L g_L^r(E) u_L^\dagger. \quad (2.7)$$

Here,  $u_L$  is the connection matrix between the left lead and the device region, and  $g_L^r(E)$  is the retarded Green's function of the decoupled lead.

Based on this formulation, the calculation of the dc conductance of the system is reduced to determining the system's full Green's function across the conducting channel,  $G_{LR}$ .

### *The Lead Green's Function and Decimation Technique*

The system under study is connected to metallic leads. A metallic lead provides conducting channels with a high density of states. To simulate the contact, the lead can be viewed as an infinite,

translational invariant extension of the actual lattice to eliminate any mismatch between conducting channel of the lead and the device. In few simple structures such as square lattice or a zigzag graphene strip, it is possible to derive analytical expressions for the semi-infinite chain's Green's function [25, 21]. However, in the case of a general chiral CNT, we have chosen a decimation algorithm to derive the lead's Green's function. This technique is discussed in details in Ref. [26]. In this approach, four recursive matrices are initialized as

$$\alpha_0 = u, \quad (2.8)$$

$$\beta_0 = u^\dagger, \quad (2.9)$$

$$\epsilon_0^s = h, \quad (2.10)$$

and

$$\epsilon_0 = h, \quad (2.11)$$

where  $u$  is the connection matrix between two neighboring unit cells and  $h$  is the Hamiltonian of a single unit cell. Then, a recursion is used to determine new matrices; the  $k$ th recursive step is given in terms of the previous  $k - 1$  step by the relations

$$\epsilon_k^s = \epsilon_{k-1}^s + \alpha_{k-1}(E - \epsilon_{k-1})^{-1}\beta_{k-1}, \quad (2.12)$$

$$\epsilon_k = \epsilon_{k-1} + \alpha_{k-1}(E - \epsilon_{k-1})^{-1}\beta_{k-1} + \beta_{k-1}(E - \epsilon_{k-1})^{-1}\alpha_{k-1}, \quad (2.13)$$

$$\alpha_k = \alpha_{k-1}(E - \epsilon_{k-1})^{-1}\alpha_{k-1}, \quad (2.14)$$

and

$$\beta_k = \beta_{k-1}(E - \epsilon_{k-1})^{-1}\beta_{k-1}. \quad (2.15)$$



When  $||\alpha_k||$  and  $||\beta_k||$  are sufficiently small, the solution converges with exponential accuracy and the lead Green's function can be approximated by

$$g_{\text{lead}}(E) \approx (E - \epsilon_k^s)^{-1}. \quad (2.16)$$

### *Recursive Algorithm*

In theory, one can evaluate the full Green's function simply by calculating

$$G = (E - \mathcal{H}_D - \Sigma_L - \Sigma_R)^{-1}, \quad (2.17)$$

where  $\mathcal{H}_D$  is the Hamiltonian of the device under study,  $\Sigma_{L,R}$  are the self-energies of the left and right leads that can be calculated via  $\tau^\dagger g_L \tau$ , and  $\tau$  is the connection matrix between the left lead and the device. However, since the number of operations for a matrix inversion problem is proportional to  $N^3$ , where  $N$  is the size of matrix (i.e., proportional to the number of sites inside the device), for the calculation of a realistic mesoscopic system, the time of calculation would be huge, as well as the amount of RAM memory required, and thus impossible to implement in practice. An efficient way to evaluate the system's Green's function can be achieved via a recursive implementation.

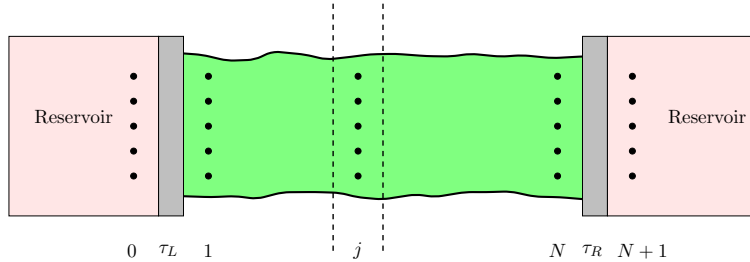


Figure 2.3: By slicing the device region between two leads, the full Green's function can be calculated efficiently. The computation cost scales linearly with the length of device.

This technique is presented in details in Ref. [27]. In this technique the device is broken up into the smallest possible transverse slices. In the most general cases, the slices can have different number of sites or shape; see Fig. 2.3. The basic idea is to transfer the Green's function of the previous slice, starting from the left lead, to the next one as a self energy, and continue this procedure from left to right, sweeping the conducting region until a desired location is reached. This results in the left-to-right Green's function. Following the same procedure, one can start from the right lead and continue to sweep from right to left until the desired location, resulting in a second Green's function, from right to left. With the combination of *left Green's function*  $G^L$  and *right Green's function*  $G^R$ , one can derived the full Green's function at any lattice point. To transfer the Green's function from one slice to the next, the Dyson's formulas [28]

$$G = G^{(0)} + G^{(0)} V G \quad (2.18)$$

$$G = G^{(0)} + G V G^{(0)} \quad (2.19)$$

can be used, where  $G^{(0)}$  is the unperturbed Green's function (corresponding to a decoupled segment in the absence of the rest of the system),  $G$  is the full Green's function, and  $V$  is the perturbative potential (i.e., the coupling between previous slice and the next). Let assume that we want to calculate the left Green's function at site  $j$ , that means the site  $j - 1$ 's left Green's function is already calculated. The unperturbed Green's function is

$$G^{(0)} = G_{j-1,j-1}^L + g_j \quad (2.20)$$

where  $g_j$  is the Green's function of the  $j$ th slice in isolation  $g_j = (E - h_j)^{-1}$ , and  $G^L$  is the left Green's function evaluated up to slice  $j - 1$ . The perturbation is the connection between slice  $j - 1$  and  $j$ ,

$$V = |j - 1\rangle\tau_j\langle j| + |j\rangle\tau_j^\dagger\langle j - 1|. \quad (2.21)$$

Therefore, we can write

$$G_{jj}^L = g_j + g_j \tau_j^\dagger G_{j-1,j}^L, \quad (2.22)$$

$$G_{j-1,j}^L = G_{j-1,j-1}^L \tau_j G_{jj}^L, \quad (2.23)$$

and solve the equations for  $G_{jj}^L$  to get

$$G_{jj}^L = [I - g_j \tau_j^\dagger G_{j-1,j-1}^L \tau_j]^{-1} g_j, \quad (2.24)$$

$$G_{j-1,j}^L = G_{j-1,j-1}^L \tau_j G_{jj}^L. \quad (2.25)$$

This procedure starts from the first slice on the left and sweeps over the whole system up to the last slice on the right incorporating the self-energy due to the right lead. Combining that with the right Green's function, the whole Green's function can be calculated. By doing that, the computational cost scales with  $\mathcal{O}(M \times (N/M)^3)$  instead of  $\mathcal{O}(N^3)$  for direct calculation, where  $M$  is the number of slices. It is clear that a smart choice of the slicing can speed up the calculation tremendously. The algorithm is pictured in Fig. 2.4.

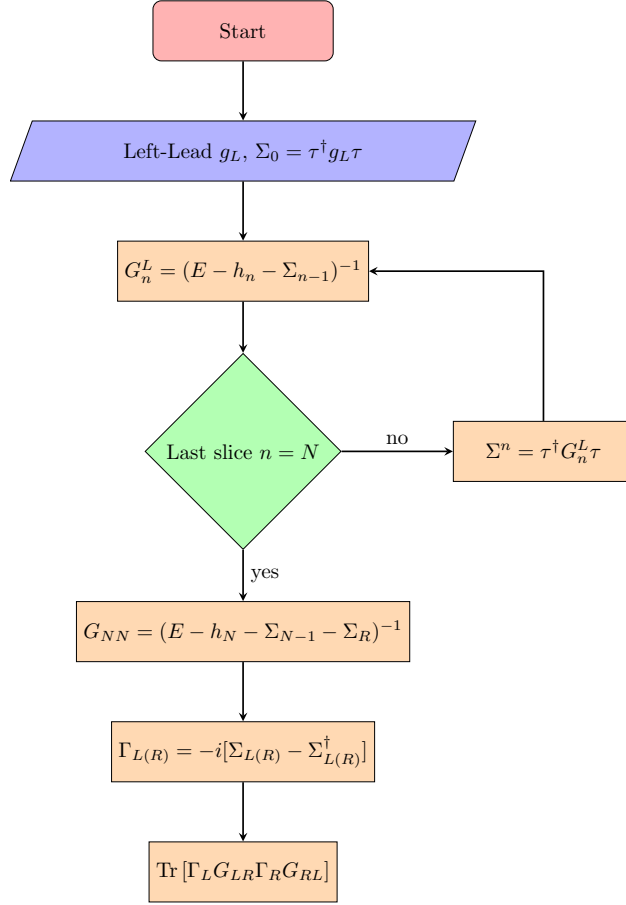


Figure 2.4: The flowchart of the recursive Green's function algorithm.

### Implementation

Based on the recursive Green's function algorithm, I developed a generic computational code to evaluate the whole Green's function by providing the unit cell structure of the lead and the system. In the case of SWCNT, the coordinates of all carbon atoms in a translational unit cell for a given chirality vector  $\mathbf{C} = m\mathbf{a}_1 + n\mathbf{a}_2$  ( $m, n$  are integers and  $\mathbf{a}_1, \mathbf{a}_2$  are lattice vectors) are generated using the recipe provided in Ref. [29]. To determine the hopping parameter  $t_{ij}$  of the unit cell, the following procedure was adopted. The distance between carbon-carbon sites on the lattice is computed and if it matches the bond length, the hopping between two sites in the Hamiltonian is

permitted. The big advantage of this approach is that it makes the rest of the code generic and applicable to other types of lattices when the atomic structure is provided. In addition, following the same procedure, one can go beyond the nearest-neighbor approximation. To build the connection matrix between two sequential unit cells, a translational vector is applied to a unit cell to generate the second unit cell; comparing these two unit cells gives us the connection matrix. To simulate the curvature effect, the angle of a carbon-carbon bond is calculated with respect to the principal axis of the CNT. A bond parallel to the principal axis is not affected but one with a component along the circumference undergoes maximum alteration.

The next step is to calculate the Green's function of an isolated lead using the decimation technique that was outlined in Sec. 2. Since the size of the unit cell can be quite large for chiral CNTs (e.g., the translational unit cell of a  $(7, 6)$  CNT has 508 sites per cell), it is often efficient to save the lead's Green's function for a large set of energy values once and read it from disk memory upon demand.

To introduce impurities and adatoms to the device, sites are randomly chosen according to a uniform distribution of a given density. The electrostatic potential that is felt on the other sites due to the adatoms is calculated by knowing the real-space coordinates of the sites. Different electrostatic potential profiles such as Gaussian, Lorentzian, and Coulomb have been considered in the simulations that we discuss later. The reason for considering profiles other than resulting from a bare Coulomb's interaction is the screening effect. A local accumulation of carrier density around the charged adatoms changes the potential profiles and their effect on carriers around them.

Finally, the constructed Hamiltonian in the presence of adatoms and an applied gate voltage is inserted into the recursive Green's function algorithm calculation the dc conductance.

We note that an applied magnetic or electric field can also be implemented very easily in this approach, although they were not required for the simulation of the experiments.

### Testing the Code

To test the code, we compare the quantum conductance and the density of states evaluated numerically with analytical expressions derived from the band structure. One can derive the bands of a chiral CNT by applying the chiral vector  $\mathbf{C} = m\mathbf{a}_1 + n\mathbf{a}_2$  as a periodic boundary condition to the dispersion relation of an infinite graphene sheet to get [30]

$$E_j(k) = \pm t \sqrt{1 + 4 \cos\left(\frac{2j\pi}{m+n} + \frac{m-n}{m+n} \frac{ka}{2}\right) \cos\left(\frac{ka}{2}\right) + 4 \cos^2\left(\frac{ka}{2}\right)}, \quad (2.26)$$

where  $j$  is the band index and  $-\frac{\pi}{2} \leq k < \frac{\pi}{2}$  is the longitudinal Bloch momentum. The band structure for a (7, 6) carbon CNT is presented in Fig. 2.5.

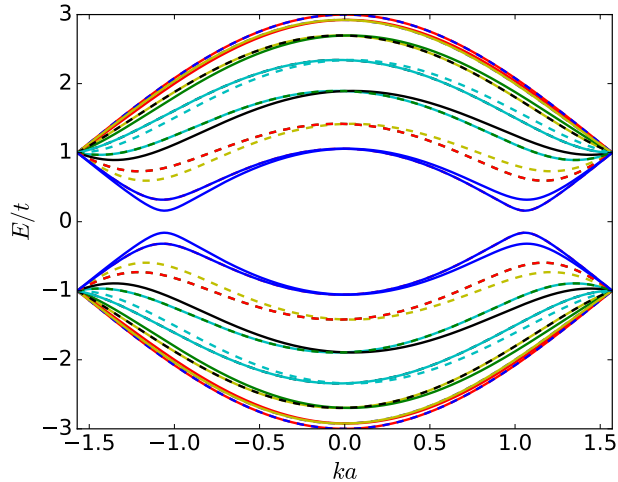


Figure 2.5: The band structure of a semiconductor (7, 6) CNT. The minimum main band gap appears at  $\frac{ka}{2} = \frac{\pi}{3}$ .

According to the Landauer formula, Eq. (2.2), for a ballistic system without any scattering processes, one expects the addition of a quantum of conductance for each opening of a new conducting channel. In Fig. 2.5 the band structure of the (7, 6) CNT is plotted based on the analytical expres-

sion (2.26). We can obtain the position of the steps in energy where new conducting channels open by sweeping over the energy axis with a straight line parallel to the momentum axis.

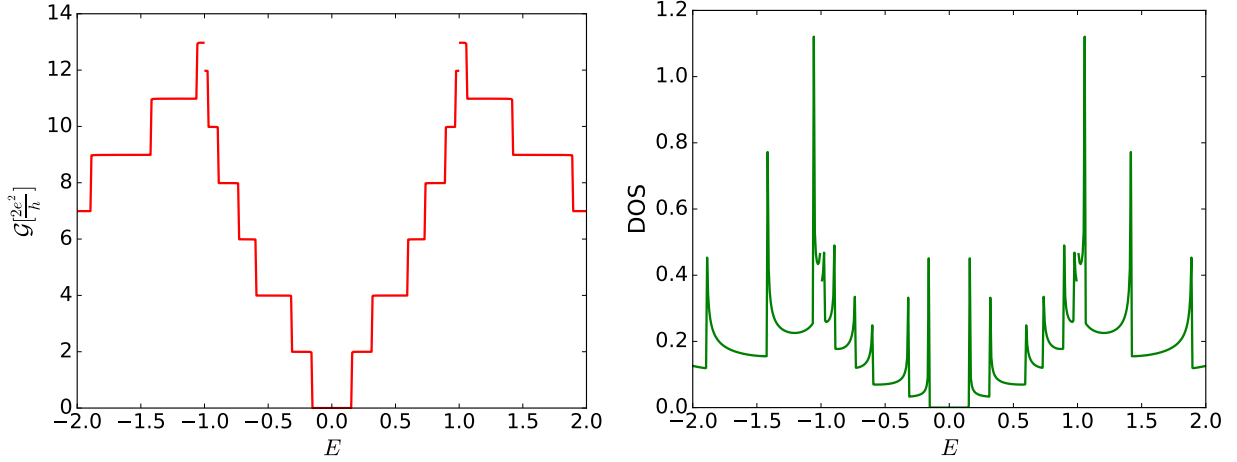


Figure 2.6: (a) The quantum conductance of a pristine (7, 6) CNT as a function of energy evaluated by the recursive Green's function technique. One quantum of conductance is added at every opening of a new channel. (b) The DOS of the same CNT. The positions of the van Hove singularities exactly coincide with the opening of conducting channels in Fig 2.5.

The density of state can be derived from the band structure using the relation

$$\rho(\epsilon) = \frac{2}{\Delta k} \sum_j \left| \frac{\partial E_j(k)}{\partial k} \right|^{-1}, \quad (2.27)$$

where  $\Delta k$  is the volume of the Brillouin zone. Alternatively, by evaluating the full Green's function for all sites, one can find the local density of state (LDOS) at each site through the expression

$$\rho_i(\epsilon) = -\frac{1}{\pi} \Im [G_{ii}^r(\epsilon)]. \quad (2.28)$$

By summing over all sites  $\text{Tr} [G^r(\epsilon)]$ , the total density of states (DOS) at energy  $\epsilon$  can be calculated. The plotted DOS is shown in Fig. 2.6. The peaks at the opening of the channels are van Hove

singularities due to the zeros of  $\left| \frac{\partial E_j}{\partial k} \right|^{-1}$  and are characteristic of such a system [20]. The positions of the van Hove singularities match the band structure and the DOS.

### Where is the Fermi Level?

The experimental results are in terms of applied gate voltage. However, it is the Fermi energy that determines the number of carriers and conducting channels in the system. Therefore, a conversion between the gate voltage to Fermi level is needed for the a comparison between simulations and experiments. In three-dimensional, extende metal, the conduction bands are close together, resulting in a high density of state that makes them a continuous reservoir of electrons. Extra charge on a metal increases the electrostatic potential due to the geometrical capacitance. However, for a low-dimensional system such as a carbon nanotube, an extra effect must be considered due to the finite DOS and the gap between the filled band and the next one. To find the chemical potential for a given gate voltage, these two contributions have to be taken into account, one from the geometrical capacitance and the other from a shift in the chemical potential, namely,

$$V_g = \frac{Q}{C_g} + \frac{\mu}{e}, \quad (2.29)$$

where  $C_g$  is the geometrical capacitance of an infinite metallic cylinder in the vicinity of an infinite metal plate,

$$C_g = \frac{2\pi\epsilon L}{\ln(4h/d)}, \quad (2.30)$$

$L$  is the length of tube,  $h$  is the distance between the center of tube and plate, and  $d$  is the diameter of the tube. On the other hand, the total charge on the CNT can be written as

$$Q = n(\mu)Le = Le \int_{-\infty}^{\infty} \rho(\epsilon) d\epsilon [f_{T,\mu}(\epsilon) - f_{T,0}(\epsilon)], \quad (2.31)$$



where  $n(\mu)$  is the charge density at chemical potential  $\mu$ ,  $f_{T,\mu}(\epsilon)$  is the Fermi-Dirac distribution function, and  $\rho(\epsilon)$  is the density of state.

A numerical integration of the DOS over energy at a given temperature must be performed to establish a conversion function, as shown in Fig. 2.7.

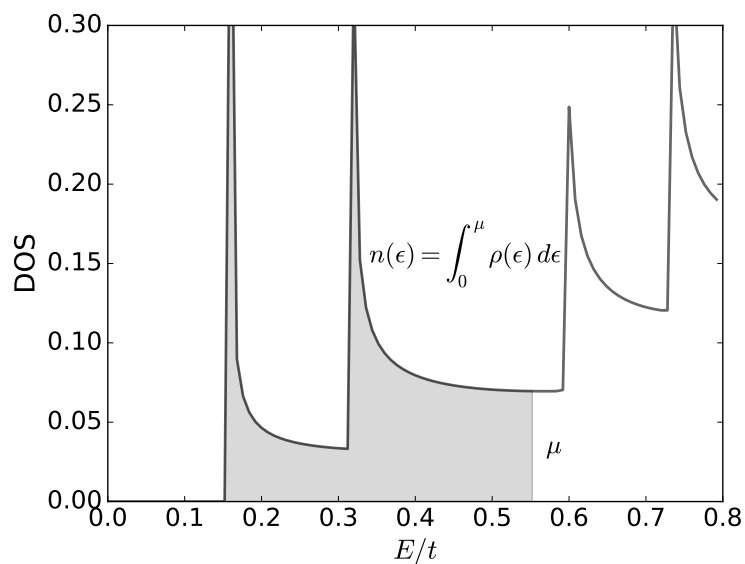


Figure 2.7: By integrating over the DOS from the neutrality point to the Fermi level, one can find the number of carriers for a given gate voltage.

We found that the experimental measurements at gate voltages of  $\pm 60$  V are equivalent to  $\pm 1.5$  eV in energy, and thus adopted the latter in the simulations.

### *Impurity Potential*

The strength of the scattering potential imposed by potassium was determined by a direct comparison of the numerical calculation with the experimental data. We started from a pristine CNT and added Gaussian potential scatterers of the form

$$V_i(\mathbf{R}) = V_0 \exp(-|\mathbf{R} - \mathbf{R}_i|/\xi^2) \quad (2.32)$$

uniformly distributed along the nanotube. Here,  $\mathbf{R}_i$  denotes the lattice location of the scatterer,  $V_0$  its (positive) strength, and  $\xi$  represents the scattering potential range. As expected, we found that the resistance of the nanotube varies considerably with  $V_0$  and  $\xi$ . We adopted the following procedure in order to find values for these parameters.

First, we evaluated the change in the average resistance when a single scatterer was added to a short nanotube segment at random locations.

When the length of nanotube was just three translation unit cells, a single adatom was added randomly in the central unit cell and the extra left and right cells kept the adatom far from contacts. For every simulation we kept the effective range of impurity fixed and varied the impurity's amplitude. The result was averaged over 200 samples with random locations of the impurity. The effective range was varied from 8.0 Å to 30.0 Å for both positive and negative carriers. We fit an parabolic curve to the resistance versus effective amplitude of the impurity and the intersection with experimental data was recorded. The analysis from single impurity simulations is presented in Figs. 2.8, and 2.9. We notice that even after averaging over 200 random locations of the adatom, the data are oscillating around the parabolic curve for negative carriers. The fluctuations are attributed to the strong quantum interference due to weak scattering and the short length of CNT segments. The fluctuation is damped in the case of positive carriers due to strong scattering rate

(see Fig. 2.9. Such simplified model enables a rapid exploration of a wide range of values for  $V_0$  and  $\xi$ .

Second, for a fixed value of  $\xi$ , we varied  $V_0$  until the change in average resistance at  $E = \pm 1.5$  eV matched the corresponding experimental value within its numerical uncertainty. The result is shown in Fig. 2.10. The data points for electrons and holes differ substantially for short scattering ranges, indicating an inconsistency with the experimental data. The data points eventually begin to converge at increasing values of the scattering range before starting to separate again. As such, our analysis indicates that  $\xi = 18 \sim 28$  Å and  $V_0 = 1.0 \sim 1.1$  eV are the choice of parameter values producing the most consistent results with the experimental data at  $E = \pm 1.5$  eV. Using the ranges of values identified for  $\xi$  and  $V_0$  by this method, we performed more in-depth calculations that yielded results that closely matched the experiments.

## Results

We evaluated the linear conductance for a wide range of nanotube lengths and scatterer concentrations, averaging each case over 600 random samples to wash away fluctuations due to phase-coherent interference. The scatterer concentration was varied within a range that kept transport diffusive (ohmic) and avoided Anderson localization of carriers. For this reason, the variation ranges for electrons and holes were different. The nanotube resistivity was obtained numerically following a procedure similar to that adopted in the experiments, namely, by varying the nanotube length, see Fig. 2.11.

The scatterer resistance was then determined by considering the change of the average resistivity with scatterer density. We find that the values of  $\xi = 20$  Å and  $V_0 = 1.1$  eV for the spatial extent and the amplitude parameters of the impurity potential produce the closest results to

the experimental values at the reference energies  $E = \pm 1.5 \text{ eV}$ , yielding a scattering strength of  $6.71 \pm 0.13 \text{ k}\Omega/\text{scatterer}$  for holes and  $0.357 \pm 0.003 \text{ k}\Omega/\text{scatterer}$  for electrons, close to the experimentally observed values. A finer match might be possible by employing numerical techniques that systematically avoid Anderson localization. However, we circumvent the localization problem by keeping the simulations away from high density of adatoms. The values of  $\xi$  and  $V_0$  identified by our theoretical analysis are significantly larger than those calculated for doped graphene where screening is expected to be stronger. Such weak screening even in the second subband, attested by the long scattering potential range, defies expectations from previous calculations [18, 19] of the electron-electron screening. In Ref. [19], the screening effect was calculated for a metallic CNT in the first-band approximation. The long-range Coulomb interaction was applied to the electrons due to the fixed-position external charge and the distribution of electrons was calculated. The result was a screening length about the diameter of a CNT. Two assumptions in that study may be the origin of discrepancy between their results and ours: (i) The limitation to low excitation energy in a metallic CNT, which constrains the current along the tube axis because the higher degrees of freedom are frozen by a wide energy gap. In contrast, the CNT that we simulated is a semiconductor and in the second band. (ii) A cutoff energy is proposed to evade the divergence of the Coulomb energy when two charges are at zero distance, and this cutoff energy is set to the diameter of the tube, which seems a plausible assumption for a low-energy system. However, in a chiral semiconductor the contribution of the circumference degree of freedom to the current is not negligible, therefore carriers can interact with the potential of adatoms at very close distance.

## Summary

We simulated the electronic transport of a semiconductor (7, 6) chiral carbon nanotube. The simulation was done using the recursive Green's function algorithm. To study the system, a general For-

tran code was developed to calculate the conductivity and density of state for an arbitrary atomic structure within the tight-binding approximation. The effect of charged adatoms on a CNT was studied by modeling the charged impurity as a Gaussian potential that is randomly placed on the CNT's lattice. Using a single impurity in a short segment, we explored a wide range of effective potential range and amplitude of charged impurity to find parameters that can fit both negative and positive carrier transport and match the experimental data. Using the single impurity analysis, we simulated large CNTs of up to length  $1.5 \mu\text{m}$ . We found a charged impurity range of  $\xi = 20 \text{ \AA}$  and an amplitude of  $1.1 \text{ eV}$  that matched the experimental data for different scattering rates for positive and negative carrier in presence of charged impurities.

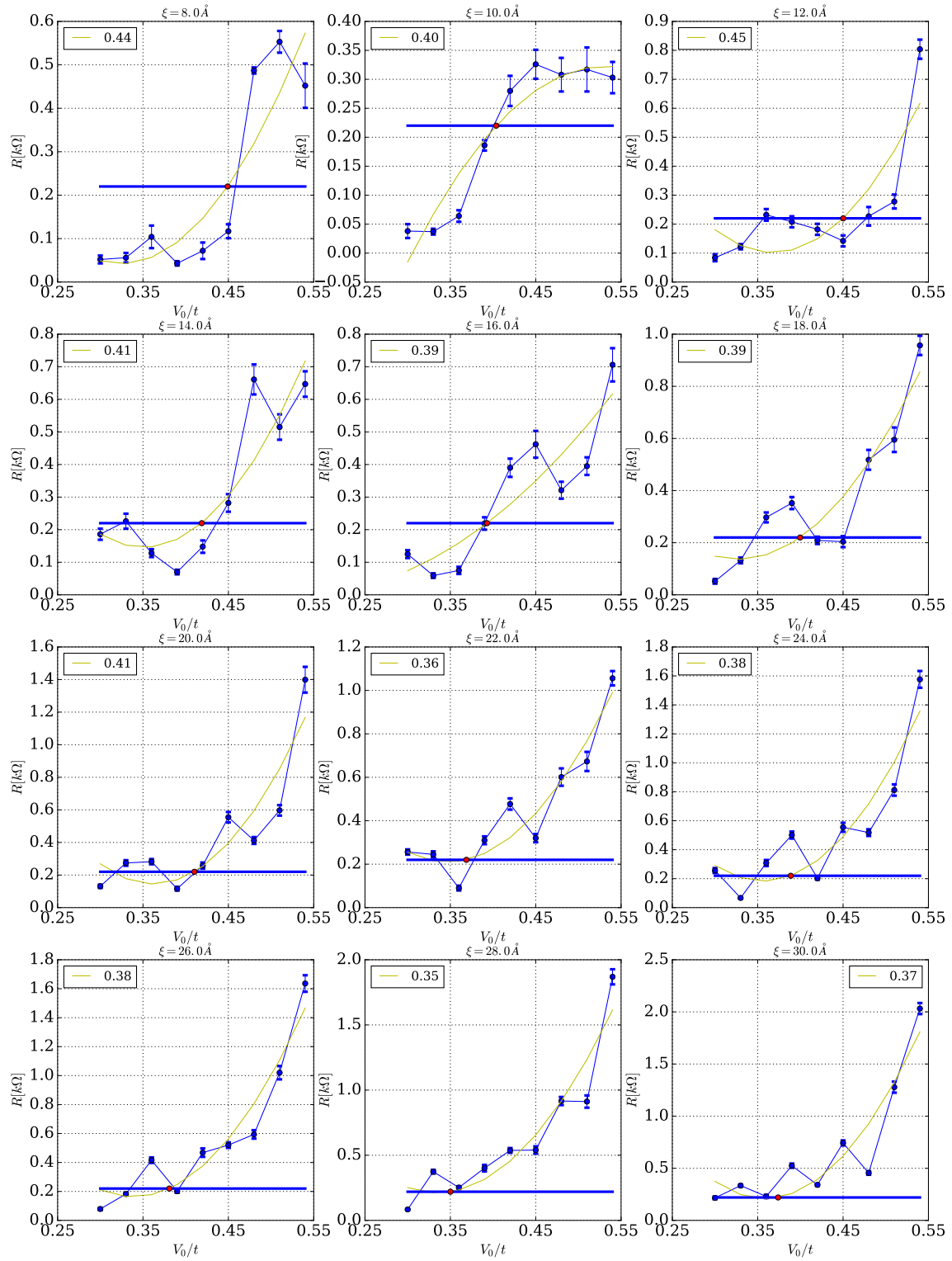


Figure 2.8: The single impurity analysis for negative carriers.

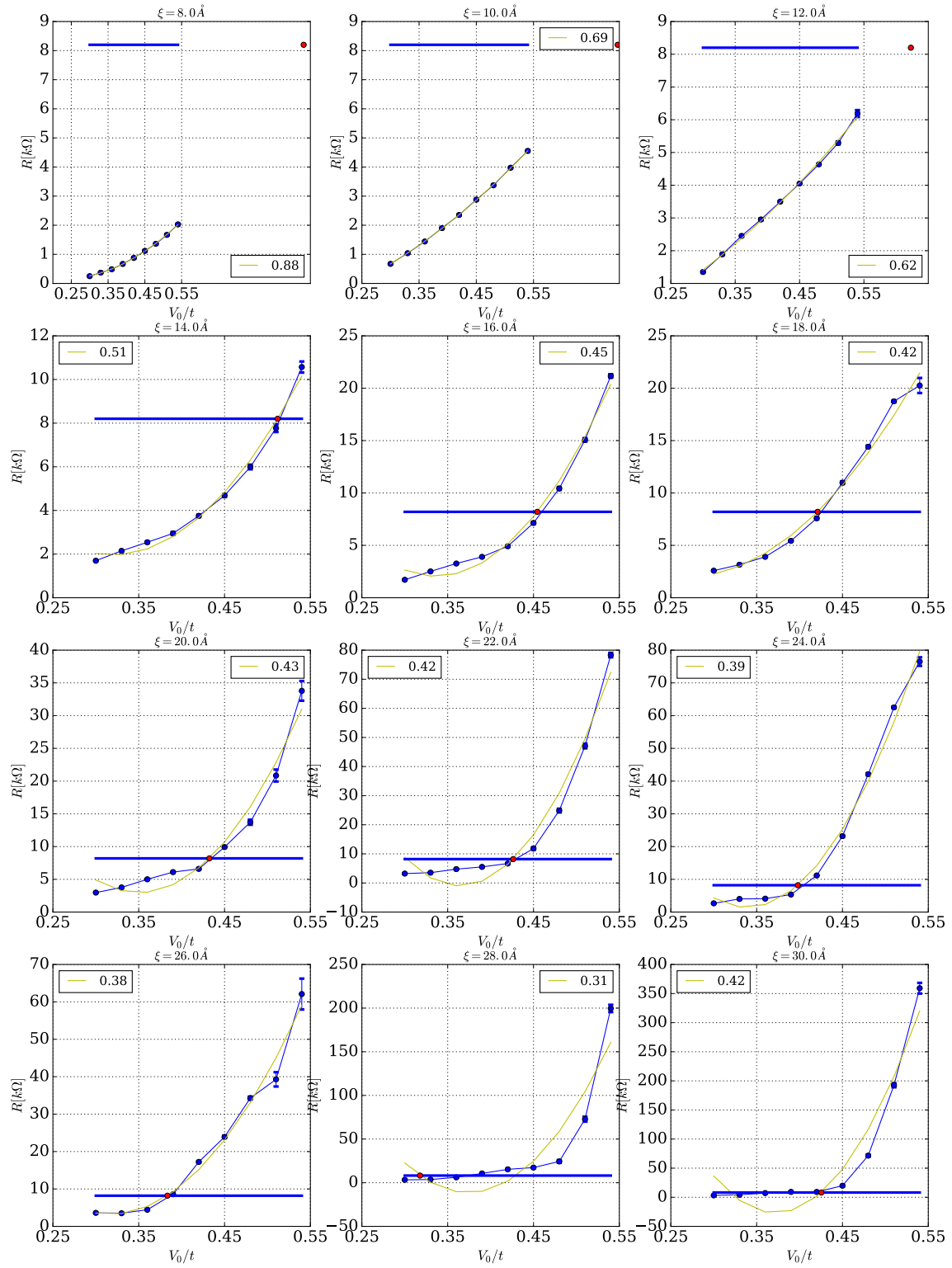


Figure 2.9: The single impurity analysis for positive carriers.

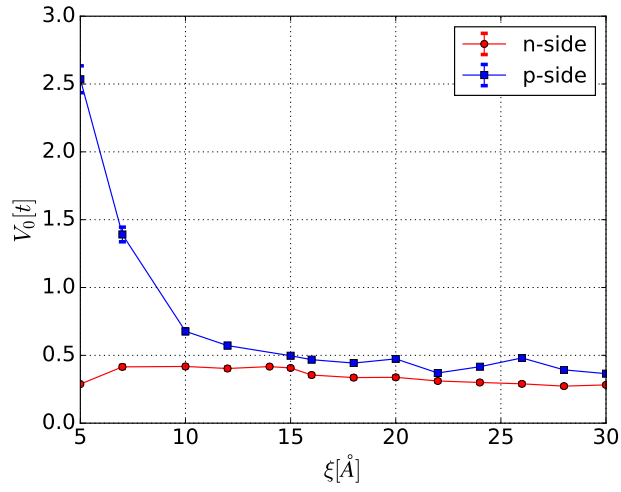


Figure 2.10: To explore possible ranges and amplitudes for the simulation of adatoms, we performed a series of calculations for a single impurity placed on a CNT segment. The data points are the comparison of the calculation with the experimental data at energy  $E = \pm 1.5$  eV. At short range, the data point for electrons and holes are inconsistent, but starting around  $\xi = 18$  Å convergence indicates possible range and amplitude, which are then used to for further simulations.

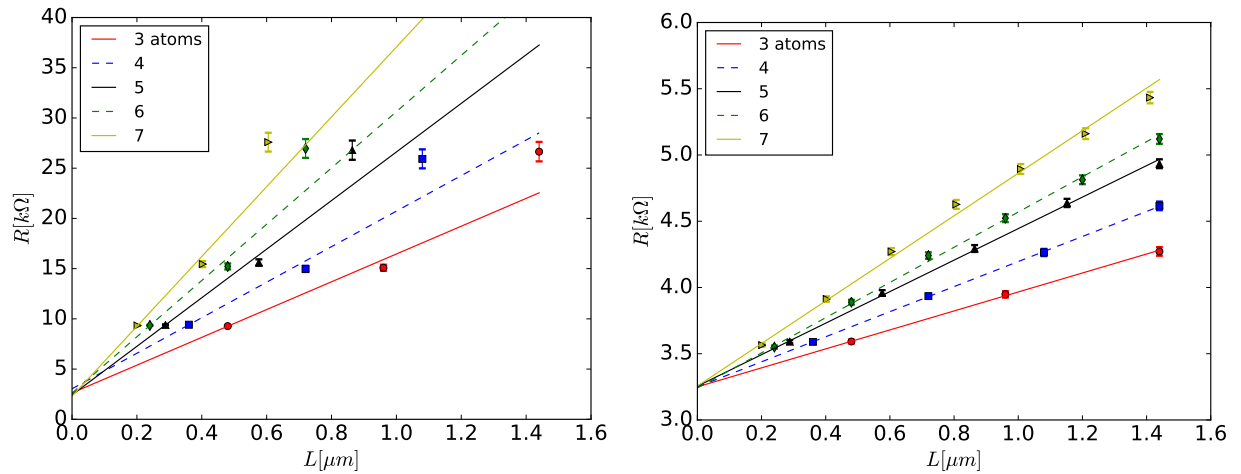


Figure 2.11: The resistance of electrons and holes in a (7, 6) chiral CNT in the presence of charged impurities. The scattering strength of positively charged adatoms is  $7.32 \pm 0.42$  k $\Omega$  for holes and  $0.31 \pm 0.01$  k $\Omega$  for electrons.



## CHAPTER 3: UNUSUAL CONDUCTANCE OF METALLIC CNT

### Motivation

Metallic CNTs are formed when the chiral indices  $(m, n)$  satisfy the relation  $m - n = 3l$ , where  $l$  is an integer number. The dispersion relation of a chiral CNT has a zero gap at  $\frac{ka}{2} = \frac{\pi}{3}$ , where  $k$  is the Bloch momentum along the CNT symmetry axis and  $a$  is the carbon-carbon bond length. However, in reality, all non-armchair metallic CNTs are quasi-metallic due to a curvature-induced gap [31]. The gap in quasi-metallic CNTs comes from the fact that the carbon-carbon bond along the tube circumference has a different length and hybridization than along the CNT's principal axis. In experimental measurements, a conductance suppression is expected around the Dirac point due to the curvature-induced gap. However, measurements on metallic (22,4) CNT show another suppression away from the Dirac point. The conductance increases from the minimum conductance point but begins to decrease as the gate voltage increases, as shown in Fig. 3.1. Notice that the minimum conductance associated with the Dirac point is located around  $V_g = 13$  V for all segment lengths. The conductance starts to decrease around  $V_g = 2$  V, forming a hump-like feature. This shape is present regardless of the segment length, indicating that this anomalous suppression is not arising from the contact resistance. To produce Fig. 3.1(right), the conductance of different segments in Fig. 3.1(left) are shifted by  $V_{\min}$  to align the minima, then the conductivity was calculated at every points of gate voltage  $V_g$  using liner fit. The unusual shape still remains, implying the intrinsic nature of this feature.

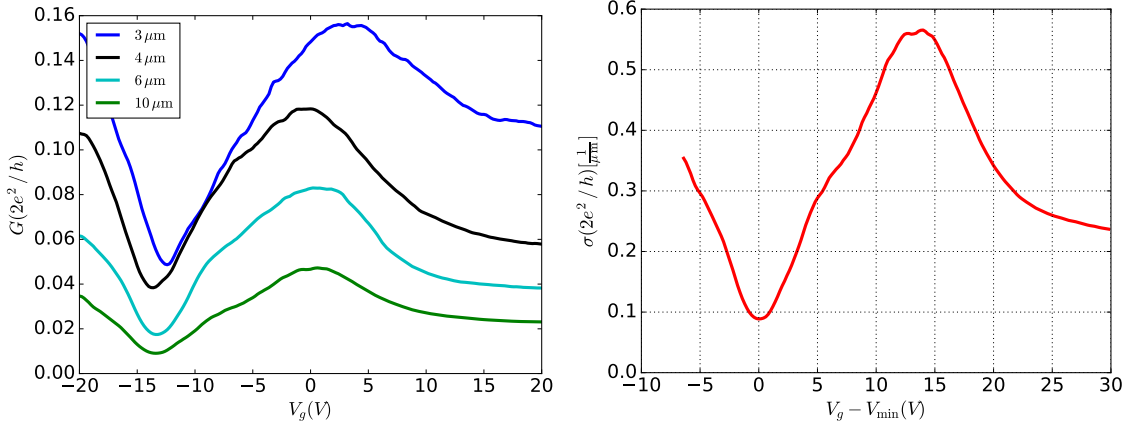


Figure 3.1: The experimental data for a quasi-metallic CNT (22, 4) show an unusual conductance versus gate voltage behavior. (left) A suppression around the Dirac point is expected due to the curvature-induced gap. However, by increasing the gate voltage, another suppression appears. (right) The unusual form of conductivity confirms that the feature is intrinsic, independent of length and contacts.

To understand the nature of this unusual behavior in the conductance, we have performed a series of simulations on quasi-metallic (22, 4) SWCNTs. The theoretical approach to the problem is based on single particle tight-binding Hamiltonian, as described in Chapter 2. The electronic transport was calculated using the Ladauer-Büttiker formula. The transmission amplitude was calculated in terms of the system's Green's function which was implemented using the *recursive Green's function* (RGF) algorithm. The technical details of this approach are similar to those presented in Chapter 2. The effect of *short-range* and *long-range* impurities are examined.

At the end of this Chapter, we present a toy model for the scattering of a massless carrier through a potential barrier. The scattering amplitudes for positive and negative carriers and the difference of scattering for a carrier on the first band of metallic CNT and on the higher conduction bands are discussed.

## Metallic CNT, Test and Simulations

The band structure of the quasi-metallic  $(22, 4)$  CNT is shown in Fig. 3.2. The Dirac point is located at  $\frac{ka}{2} = \frac{\pi}{3}$  where the bands cross the zero-energy Fermi level. By introducing curvature into the calculation of the bands, a small gap opens at the Dirac point and transforms the CNT into a quasi-metallic system. The translational unit cell of  $(22, 4)$  CNT contains 392 carbon atoms and its length is 3.44 nm. The radius of the  $(22, 4)$  CNT is 9.49 Å.

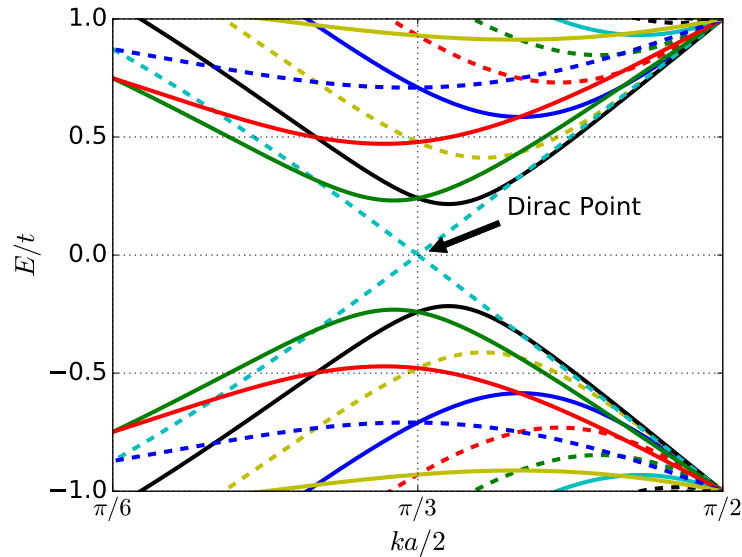


Figure 3.2: The band structure of a metallic  $(22, 4)$  CNT.

The main difference in electronic transport between metallic and semiconductor CNTs comes from the shape of the first conduction and valence bands. We notice that the minimum of the first band in a semiconductor CNT can be approximated by a parabola with a non-zero effective mass, with the carrier Hamiltonian taking the form  $\frac{p^2}{2m}$ . In contrast, the band around the Fermi level in a metallic carbon nanotube is linear, with a zero effective mass (i.e., it describes “massless fermions”). In the latter case, electronic transport is governed by a Dirac equation, which will be employed later in this Chapter.

The same computational code developed for Chapter 2 can be applied to this problem. Using the  $xyz$  coordinates of the carbon atoms in one translational unit cell, the Hamiltonian  $h$  and the connection matrices  $\tau$  are constructed and fed into the RGF code. First, we performed a few tests on pristine  $(22, 4)$  CNT and compared the results to known features that can be derived analytically to make sure that the code performed correctly. As we did in Chapter 2, we compared the energies where a new quantum of conductance is added to the opening of the channels that we obtain from the analytical band structure. The conductance and the density of state of a pristine  $(22, 4)$  CNT are presented in Fig. 3.3. As we can see, an additional quantum of conductance is added exactly at the opening of a new conducting band. The van Hove singularities that are characteristic of low-dimension systems can be seen at the opening of each band due to the zero derivative of  $\frac{\partial \epsilon}{\partial k}$  at the minima of the bands.

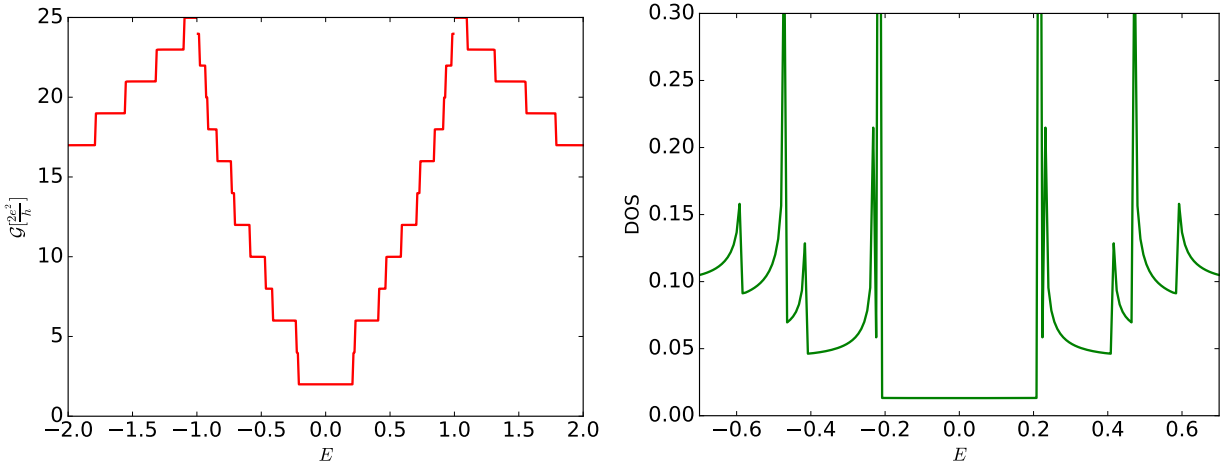


Figure 3.3: The quantized conductance and the density of state of a pristine quasi-metallic  $(22, 4)$  CNT.

In this series of simulations the role of the CNT curvature on the conductance was also investigated. The hopping amplitude on C–C bonds was determined by

$$t_{\text{eff}} = t_0 + \delta \sin \theta, \quad (3.1)$$

where  $\theta$  is the angle of the bond with respect to the CNT's principal axis. The next crucial information that was needed to study this problem was a good estimate of the chemical energy due to applied gate voltage. As we will explain later, the scattering amplitude shows different behavior in the first channel compare to the higher channels. To determine the chemical potential, we follow the same recipe that was developed in the Chapter 2. The density of state can be evaluated using the imaginary part of the total Green's function

$$\rho_i(E) = -\frac{1}{\pi} \Im [G_{ii}^r(E)], \quad (3.2)$$

where  $\rho_i$  is the LDOS at site  $i$  and  $G_{ii}^r$  is the retarded total Green's function at site  $i$ . By summing over all sites in one unit cell, the total DOS as a function of energy is determined. The conversion between applied gate voltage and chemical potential can be performed by integrating over the DOS to the point that the contribution due to the geometrical capacitance and the shift in the band is equivalent to the applied gate voltage.

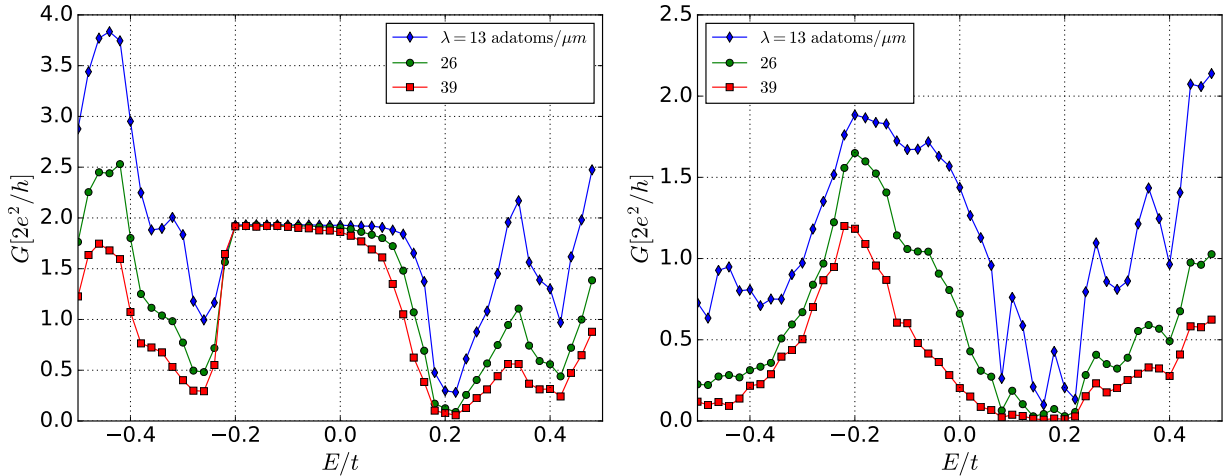


Figure 3.4: The conductance of a metallic  $(22, 4)$  CNT in the presence of adatoms with scattering range  $\xi = 9 \text{ \AA}$  (left) and  $\xi = 18 \text{ \AA}$  (right). The results were produced by averaging over 400 samples.

First, we performed a number of simulations in the presence of Gaussian impurities with different amplitudes and ranges. In Fig. 3.4, the results for impurities with the effective ranges of  $\xi = 9 \text{ \AA}$  and  $\xi = 18 \text{ \AA}$  are presented. A few features deserve attention:

- The asymmetry between positive and negative energies (i.e., electrons and holes carriers) due to the sign of charged impurities.
- The robustness of the first channel compare to the higher channels in the presence of impurities.
- The dramatic decrease in conductance with increasing effective range of impurities, which can be seen by comparing left and right panels, showing that the positive region of the first band is more affected.
- Finally, the shift toward negative energies of the conductance minimum for positive impurities.

The resistivity that was extracted from the experimental measurements shows the same hump shape, implying that the feature is intrinsic to the device, independent of the quality of the contacts. To test this observation, we calculated the conductance for different length of the nanotube in the presence of same impurity profile and density. As one can see in Fig. 3.5(left), the minima of the conductance are located at the two ends of the first band, independently of the CNT length.

We note that the experimental measurement shows the same hump shape even below 10 K, when phonons are virtually suppressed. The scattering due to defects or extrinsic charged impurities is still effective at low temperature. We thus believe that the hump is caused by elastic scattering of carriers along the nanotube. The measured carbon nanotube device shows relatively higher resistance than defect-free, ultra-clean nanotubes. It implies that the nanotube has some atomic defects or extrinsic charged impurities that cause the anomalous suppression.

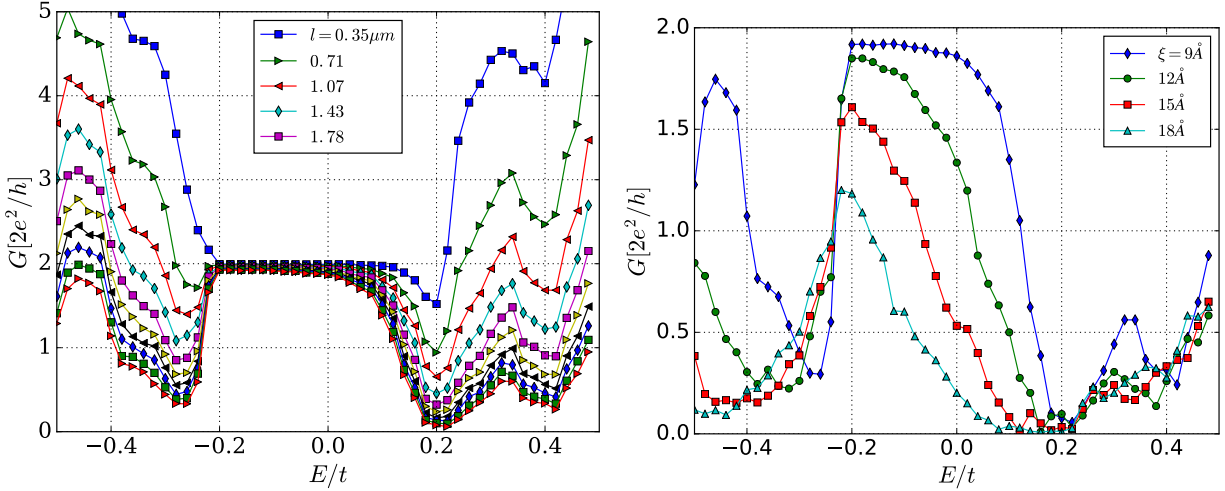


Figure 3.5: (left) The conductance for different length of a metallic  $(22, 4)$  CNT in the presence of positive impurities. Here the amplitude and the range of impurities are  $V_0 = 0.4t$  and  $\xi = 8 \text{ \AA}$ . (right) The conductance of a metallic  $(22, 4)$  CNT in the presence of adatoms with different scattering range.

Results for fixed length and impurity density for several impurity ranges are presented in Fig. 3.5(right).

The interesting feature in this plot is that the negative edge of the first band is very robust to the impurities; and the sharp edge of the conductance does not shift, only the amplitude decreases.

Finally to understand the effect of defects, we performed some calculations in the presence of very short range impurities with high amplitudes. In contrast to a long range impurity, the first band is affected by short range impurities dramatically. The effect is symmetric between electrons and holes. The result of simulations are shown in Fig. 3.6. The right panel shows the conductance in presence of both short and long range impurities. The short range impurities suppress the conductance at the Dirac point, while the long range impurities affect the transport in the higher bands. In Fig. 3.6(right) the conductivity versus applied gate voltage in the presence of mixture of short range and long range impurities is plotted. The result is qualitatively close to the experimental observations.

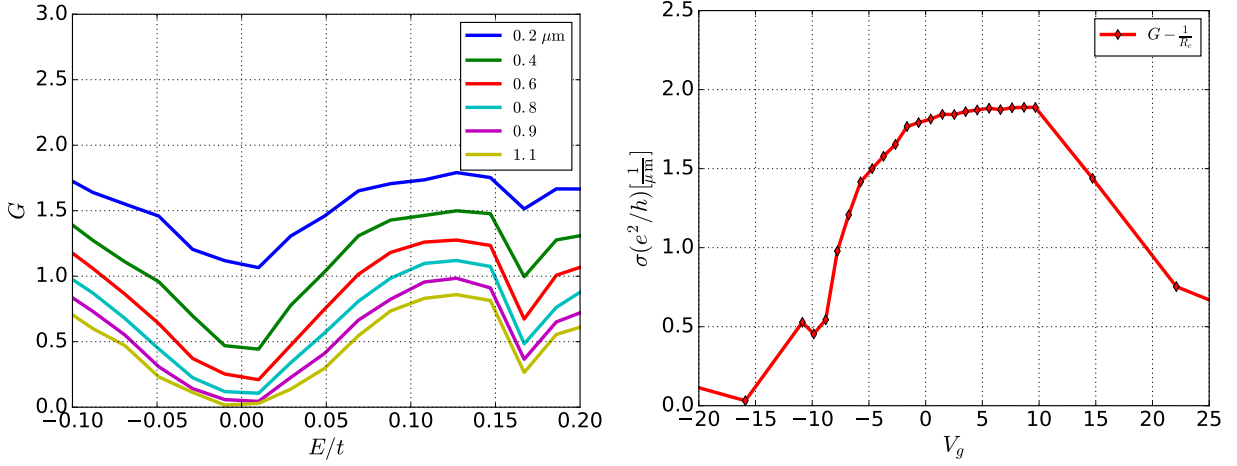


Figure 3.6: (left) The effect of defects on the conductance of a metallic  $(22, 4)$  CNT. In contrast to long-range impurities, defects affect the electronic transport in the first band and it is symmetric between electrons and holes. (right) The resistivity of a metallic CNT in the presence of both long range impurities and defects.

### Physical Interpretation: Robustness of the First Band

To gain some insight about the scattering behavior in the first band, it is worth looking at the electronic transport around the Dirac point. The conductance of the first conducting channel in the presence of charged impurities remains almost intact. We believe that this characteristic comes from the massless nature of carriers around the Dirac points. Let us start with the band structure of pristine graphene layer,

$$\epsilon(\mathbf{k}) = \pm t \sqrt{1 + 4 \cos\left(\frac{a\sqrt{3}}{2}k_x\right) \cos\left(\frac{a}{2}k_y\right) + 4 \cos^2\left(\frac{a}{2}k_y\right)}. \quad (3.3)$$

Using a Taylor expansion around the Dirac point, the Hamiltonian can be approximately written as

$$H = v_F \boldsymbol{\sigma} \cdot \mathbf{k}, \quad (3.4)$$



where  $\sigma$  contains Pauli matrices describing the pseudo-spin and  $v_F$  is the Fermi velocity of the carriers in graphene. By solving the Dirac equation

$$-iv_F \begin{bmatrix} 0 & \partial_x - i\partial_y \\ \partial_x + i\partial_y & 0 \end{bmatrix} \begin{bmatrix} \phi_1(x, y) \\ \phi_2(x, y) \end{bmatrix} = \epsilon \begin{bmatrix} \phi_1(x, y) \\ \phi_2(x, y) \end{bmatrix}, \quad (3.5)$$

the eigenstates are found to be

$$\psi = \frac{1}{\sqrt{2}} \begin{pmatrix} 1 \\ \pm e^{i\phi} \end{pmatrix} e^{i(k_x x + k_y y)}, \quad (3.6)$$

where  $\phi = \tan^{-1} \left( \frac{k_y}{k_x} \right)$  and  $\frac{\epsilon}{v_F} = k = \sqrt{k_x^2 + k_y^2}$ . Now, let us find the transmission probability of a massless carrier through a rectangular barrier around the Dirac points, as shown in Fig. 3.7. The wave function can be written in the form

$$\psi_i = \frac{1}{\sqrt{2}} \begin{pmatrix} 1 \\ s e^{i\phi} \end{pmatrix} e^{i(k_x x + k_y y)} + \frac{r}{\sqrt{2}} \begin{pmatrix} 1 \\ -s e^{-i\phi} \end{pmatrix} e^{i(k_x x + k_y y)}, \quad (3.7)$$

on the left of the barrier; inside the barrier region we have

$$\psi_{ii} = \frac{a}{\sqrt{2}} \begin{pmatrix} 1 \\ s' e^{i\theta} \end{pmatrix} e^{i(q_x x + k_y y)} + \frac{b}{\sqrt{2}} \begin{pmatrix} 1 \\ -s' e^{-i\theta} \end{pmatrix} e^{i(q_x x + k_y y)}, \quad (3.8)$$

where  $s = \text{sign}(E)$ ,  $s' = \text{sgn}(E - V_0)$ ,  $\theta = \tan^{-1} \left( \frac{k_y}{q_x} \right)$  and  $q_x = \sqrt{(V_0 - \epsilon)^2 / v_F^2 - k_y^2}$ . Notice that during the scattering process  $k_y$  is conserved. Finally, in the third region we have

$$\psi_{iii} = \frac{t}{\sqrt{2}} \begin{pmatrix} 1 \\ s e^{i\phi} \end{pmatrix} e^{i(k_x x + k_y y)}. \quad (3.9)$$

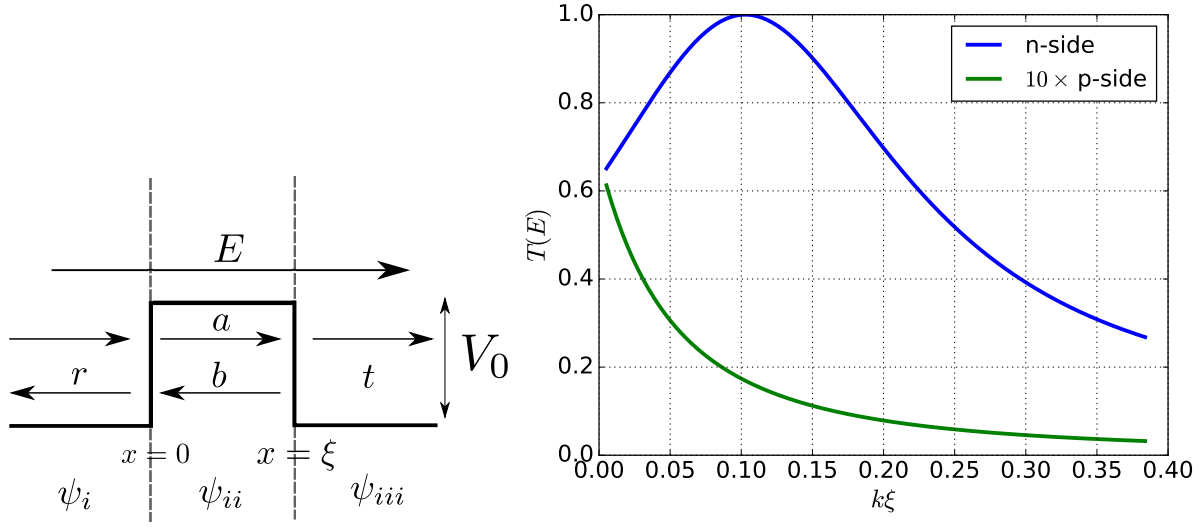


Figure 3.7: (left) A massless particle encounters a rectangular barrier or well in analogy of the scattering of positive and negative carriers in presence of a positive charged adatom. (right) The transmission probability for positive and negative carriers are presented as a function of the effective range  $\xi$  of impurities.

The transmission and reflection coefficients are determined by imposing continuity of the wave function at boundaries,

$$\psi_i(x = 0, y) = \psi_{ii}(x = 0, y) \quad (3.10)$$

$$\psi_{ii}(x = \xi, y) = \psi_{iii}(x = \xi, y) \quad (3.11)$$

where  $\xi$  is the width of barrier which can be considered as the range of the impurities. The four following equations give us the transmission coefficient:

$$1 + r = a + b, \quad (3.12)$$

$$e^{i\phi} - re^{-i\phi} = ae^{i\theta} - be^{-i\theta}, \quad (3.13)$$

$$ae^{iq_x\xi} + be^{-iq_x\xi} = te^{ik_x\xi}, \quad (3.14)$$

and,

$$ae^{i\theta}e^{iq_x\xi} - be^{-i\theta}e^{-iq_x\xi} = te^{i\phi}e^{ik_x\xi}. \quad (3.15)$$

The easiest way to find  $T = tt^*$  is to find  $a$  and  $b$  from the first two and the last two equations separately. Then, the reflection coefficient can be derived in terms of the transmission coefficient from both equations as

$$r(e^{i\theta} + e^{-i\phi}) = (e^{i\theta} - e^{i\phi}) [te^{i(k_x+q_x)\xi} - 1], \quad (3.16)$$

$$r(e^{-i\theta} - e^{-i\phi}) = (e^{-i\theta} + e^{i\phi}) [te^{i(k_x-q_x)\xi} - 1]. \quad (3.17)$$

By canceling  $r$  between these two equations we get

$$t = \frac{2 \cos \theta \cos \phi e^{-ik_x\xi}}{[1 + \cos \theta + \cos \phi]e^{-iq_x\xi} - [1 - \cos(\theta - \phi)]e^{iq_x\xi}}. \quad (3.18)$$

Finally, the transmission probability is found to be

$$T = |t|^2 = \frac{\cos^2 \theta \cos^2 \phi}{(\cos \theta \cos \phi \cos q_x\xi)^2 + [1 - \cos(\theta - \phi)]^2 \sin^2 q_x\xi}. \quad (3.19)$$

In the case of a CNT, we consider the  $x$  direction as the direction along the CNT's symmetry axis and  $y$  as the direction of the circumference, yielding

$$\mathbf{C} = m\mathbf{a}_1 + n\mathbf{a}_2. \quad (3.20)$$

Close to the Dirac points,  $E = 0$  implies  $k_y = 0$ . As a result, both phase angles  $\theta$  and  $\phi$  are zero. It is easy to see that the transmission probability approaches  $T = 1$  and it is independent of the energy as far as the dispersion relation can be considered linear.

This picture explains the asymmetry between scattering strength of electrons and holes in the presence of charged adatoms at the first band. Also it confirms that the carriers in the first band can experience a transparent scattering with  $T = 1$ .

### Summary

In this Chapter we presented a study of the unusual behavior in the electronic transports of a metallic CNT. The importance of this study comes from the fact that it reveals the manifestation of the nature of charge carriers around the neutrality point. We have shown that a conductance suppression far away from the neutrality point is due to the fact that carriers obey a massless Dirac equation. The applied gate voltage determines the conducting band where carriers come from. The transport of carriers from higher bands is affected heavily by the presence of impurities and defects. On the contrary, the carriers from the first conducting band experience less scattering. As a result we see an extra suppression at the opening of the second channel. Our results are backed by experimental observations on the quasi-metallic CNT (22, 4).

# CHAPTER 4: DYNAMICAL SPIN INJECTION IN LOW-DIMENSIONAL MATERIALS

## Introduction

One of the key elements in any implementation of spintronics is an efficient source of spin current [32]. Among the different methods available, dynamical spin injection from a ferromagnetic metal (FM) into an adjacent nonmagnetic metal (NM) has been theoretically proposed [8] and experimentally observed [9, 10, 11, 12, 13]. In this method, in addition to a longitudinal static magnetic field, an oscillating transverse magnetic field is applied, inducing a magnetization precession in the FM. Most of the angular momentum transferred to the FM by the oscillating field is dissipated through spin-relaxation processes in the bulk, but a small part survives as a spin current injected into the NM.

The exotic electronic properties of graphene have captured the attentions of the physics community since the first experiments with this material [33, 34]. High mobility and a long spin-relaxation length are features that make graphene a promising passive element for spintronics [35]. In addition, the enhancement of spin-scattering processes in graphene by adatoms or defects [36], which also yield the spin Hall effect [37] and the inverse spin Hall effect, have led to proposals of graphene-based spin-pumping transistors [38, 39].

Recent experimental studies [17, 14] show an increase in the ferromagnetic resonance (FMR) damping when a graphene sheet is placed in contact with a FM subject to an oscillating magnetic field, see Fig. 4.1. One interpretation of the phenomenon is that part of the precessing magnetization leaks into the graphene sheet as a spin current, effectively leading to an additional channel of magnetization damping.

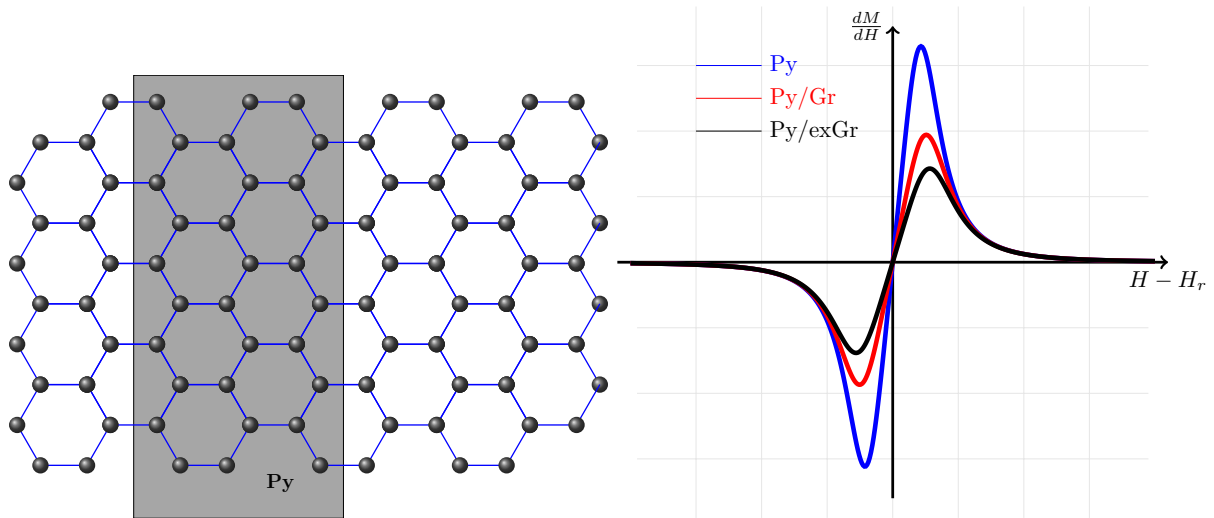


Figure 4.1: (left) A schematic structure of dynamical spin injection in FM/Gr setup. A part of graphene sheet is covered by a FM. A time-dependent magnetic field compensates the damping of the precession of the magnetization in FM. (right) The FMR measurements on three setups Py, Py/Gr, and Py/Gr(extended) confirms that an extra damping of magnetization precession in FM is induced by pumped spin current into the graphene layer.

While time-dependent scattering theory [15, 8] based on the general theory of adiabatic quantum pumping [40] relates the increase in the FMR damping to the interface mixing conductance, further effort is necessary to describe microscopically spin pumping into two-dimensional (2D) materials. A recent study [41] applied the time-dependent scattering theory to spin pumping in a insulating ferromagnet laid on top of a 2D metal. While insightful, this approach is not suitable for including disorder and spatial inhomogeneities such as adatoms; and when applied to graphene, it was confined to the vicinity of the neutrality point.

Another aspect that can be addressed with this formulation is the distinction between the angular momentum that relaxes at the interface and the part that flows into the NM. As it was shown in the first experiment by Singh *et. al.*, [14] even without graphene protruding away from the FM (when no spin current injection is possible), the enhancement of damping is significant. This enhancement has been associated to two-magnon scattering at the interface [42]. However, in systems where

graphene protrudes away from the FM, an extra damping has been measured due to the flow of spin current into graphene. An atomistic study of such phenomenon is needed to discriminate the contribution of spin current and the surface relaxation in enhancement of damping.

Here, we develop a microscopical formulation of spin pumping from a FM into a NM material. Both the atomic structure of the materials and the particular geometry of the system can be taken into account exactly in this formulation. The spin current expression is written in terms of the Green's function of the NM portion, allowing one to apply efficient recursive numerical methods for the computation of spin currents [27]. Another advantage of the formulation we present is the possibility to include accurate, microscopic models of spin-orbit coupling in the NM portion, as it relies on a spatial tight-binding representation of the system.

This chapter is organized as follows. We start this chapter with a brief review of the FM/Gr dynamical spin injection experiment, then we discuss the standard theory that was developed by Brataas and Tserkovnyak [16] which is widely accepted in the spintronics community to describe the dynamical spin current. Then the failure of the theory when it is applied to a FM/Gr device is discussed. In Sec. 4, we use a one-dimensional, tight-binding chain coupled to a magnetic site to introduce the time-dependent boundary condition problem and to derive an expression for the spin current based on an equation-of-motion formulation. The definition of charge and spin current appropriate to the problem in hand are discussed in Sec. 4. We apply the formulation to a zero-length system in Sec. 4 and a finite-length chain in Sec. 4. In Sec. 4 the general expression for the spin current in 2D system, including spin-orbit mechanisms is derived. In Sec. 4 we summarize the results and point to future some work. Details of the formulation and some derivations are presented in the Appendices.

## FM/Gr FMR Measurements and Standard Theory of Dynamical Spin Injection

A dynamical spin injection setup consists of two materials, a ferromagnet and a non-magnetic medium. A time-dependent magnetic field is applied to the FM to induce magnetization precession and to compensate the damping of the precession. Electrons from the NM region come to the FM/NM interface and their spin states are scattered by FM layer depends on the magnetization direction to return to the NM region with altered spin states. The result would be a spin current with zero net charge current. There are two indirect mechanisms to detect the spin current in such devices, one is FMR measurement to determine the enhancement of the damping. Second, *Inverse Spin Hall Effect* (ISHE) that converts the spin current into a lateral electric voltage in NM region in the presence of strong spin-orbit interactions.

When the dynamical spin injection in FM/Gr was reported for the first time [14], it was not clear what is the origin of an extra damping in FMR experiments. The damping could be because of the enhancement of spin relaxation at the FM surface in the proximity of graphene layer, or spin currents were actually pumped into the graphene and responsible for an extra damping. In an upgraded version of measurements [17], different samples were prepared to identify the source of damping. When a layer of copper was placed on FM, no enhancement were detected as it was expected due to the small spin relaxation of Cu. However, when a buffer layer of Cu was sandwiched between Py and graphene the enhancement was significant. In this measurement, the area of graphene covered just the Py interface which eliminates any possibility of the spin current pumping. In the last setup, the graphene was protruded out of the FM interface. The extra damping compared to the previous experiments confirmed the spin current pumping in graphene.

The theory of dynamical spin injection is an extension of the adiabatic pumping of charge in mesoscopic systems [43]. Since the precession of magnetization is very slow compared to the other electronic dynamics of the system, the adiabatic approximation was applied to the problem



from the beginning. In this theory the amount of pumped spin current is expressed in term of a parameter called *mixing conductance*  $g^{\uparrow\downarrow}$  and it is defined

$$g^{\uparrow\downarrow} = \sum_{m,n} (\delta_{m,n} - r_{mn}^{\uparrow} r_{mn}^{\downarrow}). \quad (4.1)$$

where  $r_{mn}^s$  is the spin-s reflection amplitude between  $m$  and  $n$  conducting channels at the interface. This theory has been successful to quantify the dynamical spin injection in bulk FM/NM systems. However, when we applied the formalism to the FM/Gr measurements, the value of mixing conductance  $g^{\uparrow\downarrow} = 6.68 \times 10^{18} \text{ m}^{-2}$  was comparable to those found in Py/Pt or Py/Pd samples. From the definition, one expects that the mixing conductance to be proportional to the number of conducting channels at the interface. In a one dimensional interface between graphene underneath and the extended part, the mixing conductance is expected to be orders of magnitude smaller. The second difficulty that we encountered is to explain a large backflow of spin current that is expected in a system with a long spin relaxation length, see Fig. 4.2. When the spin current injection is faster than the spin relaxation rate in the NM, a spin-dependent chemical potential builds up in NM and diffuses back a spin backflow current into the FM that decrease the effective mixing conductance

$$\frac{1}{g_{\text{eff}}^{\uparrow\downarrow}} = \frac{1}{g^{\uparrow\downarrow}} - \beta, \quad (4.2)$$

The value of  $\beta \approx 4 \times 10^{-12} \text{ m}^2$  that was calculated for the graphene sample is orders of magnitude larger than the measured mixing conductance. That leads to a negative value for the effective mixing conductance.

These two problems motivated us to look for an atomistic model of dynamical spin injection problem to quantify the amount of spin current and expected enhancement of damping in such systems. In the next section, we introduce our model and proceed to derive an expression for spin currents in such systems.

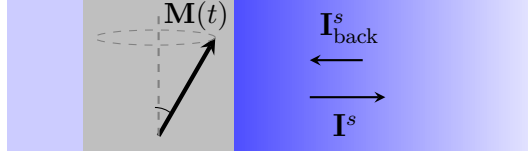


Figure 4.2: An schematic presentation of the theory of dynamical spin injection into NM. In this theory the FM region is act as an dynamical scatterer between two metallic reservoirs. If the spin relaxation rate is smaller than the spin injection rate in NM, a backflow spin current decrease the damping of magnetization precession.

### One-Dimensional Model

Here, we address the problem of spin pumping in low-dimensional materials in contact with a FM where a precessing magnetization is induced. In such systems, itinerant electrons travel from the NM portion into the FM with a random spin orientation and back. The magnetization of FM changes the orientation of the spin of the returning electrons, and angular momentum leaks out of the FM and into the NM region as a spin current. To model such hybrid FM/NM system, the FM region can be viewed as a time-dependent boundary condition to the NM region.

We begin by considering the idealized situation of a one-dimensional system, see Fig. 4.3. We adopt the transport formulation developed by Dhar and Shastry [44] as the starting point and extend it to include spin-dependent and time-dependent boundary conditions in the special case of a single reservoir attached to the nonmagnetic metal region.

Consider a one-dimensional chain where the site at  $j = 1$  is connected to a magnetic site at  $j = 0$  as shown in Fig. 4.3. At the magnetic site, itinerant electrons interact with the time-dependent magnetization of the FM,

$$\mathbf{M}(t) = M_{\parallel} \hat{\mathbf{z}} + M_{\perp} (\hat{\mathbf{x}} \cos \Omega t - \hat{\mathbf{y}} \sin \Omega t). \quad (4.3)$$

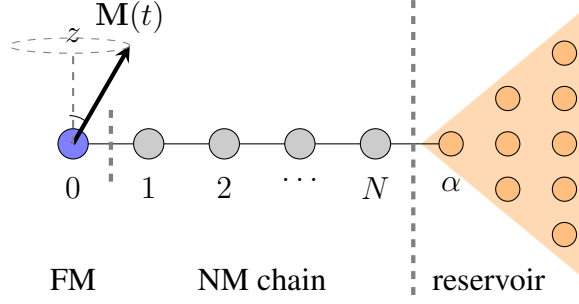


Figure 4.3: Scheme of the one-dimensional model of spin pumping from a magnetic site representing a ferromagnet (FM) to a nonmagnetic (NM) chain connected to a reservoir.

The dynamics of the magnetization is determined by the Landau-Lifshitz-Gilbert equation, where a damping term is introduced phenomenologically to account for magnetization losses.[45] Here, we assume that Eq. (4.3) describes the stationary state of the magnetization and includes any damping. The opposite end of the chain, at the site  $j = N$ , is connected to a reservoir via a site  $\alpha$ . A hopping term describes the itinerant electronic motion along the chain, where no spin-orbit mechanism is present at this point. The Hamiltonian of each segment reads

$$\mathcal{H}_{\text{mag}} = -\frac{J}{2} \mathbf{M}(t) \cdot \sum_{s,s'} a_s^\dagger \boldsymbol{\sigma}_{ss'} a_{s'}, \quad (4.4)$$

$$\mathcal{H}_{\text{chain}} = -\sum_{j=1}^{N-1} \sum_{s,s'} \left( c_{j+1,s}^\dagger \tau_{j;s,s'} c_{j,s'} + c_{j,s}^\dagger \tau_{j;s',s}^* c_{j+1,s'} \right) + \sum_{j=1}^N \sum_s V_{j,s} c_{j,s}^\dagger c_{j,s}, \quad (4.5)$$

and

$$\mathcal{H}_{\text{res}} = -\sum_{\lambda,\eta} \sum_s T_{\lambda\eta} d_{\lambda,s}^\dagger d_{\eta,s}, \quad (4.6)$$

where  $s, s' = \uparrow, \downarrow$ . The fermionic operators  $a_s$ ,  $c_{j,s}$ , and  $d_{\lambda,s}$  act on the magnetic, chain, and reservoir sites, respectively and obey the standard anticommutation relations.  $\boldsymbol{\sigma} = (\sigma^x, \sigma^y, \sigma^z)$  are

Pauli matrices. The parameters  $\tau_{j;s,s'} = \tau_{j;s',s}^*$  describe the hopping amplitude between neighboring sites  $j$  and  $j + 1$  in the chain and could be spin dependent; in the absence of spin-orbit coupling,  $\tau_{j;s,s'} = \delta_{s,s'} \tau_j$ . The on-site potential  $V_{j,s}$  is included to account for inhomogeneities in the chain. Finally, the matrix elements  $T_{\lambda\eta}$  describe the site connectivity in the reservoir, which can be complex.

The coupling between the magnetic site and the chain and between the chain and the reservoir are assumed spin independent and are given by the Hamiltonians

$$\mathcal{H}_{\text{mag-chain}} = -\gamma_0 \left( a_s^\dagger c_{1,s} + c_{1,s}^\dagger a_s \right) \quad (4.7)$$

and

$$\mathcal{H}_{\text{chain-res}} = -\gamma_\alpha \left( c_{N,s}^\dagger d_{\alpha,s} + d_{\alpha,s}^\dagger c_{N,s} \right), \quad (4.8)$$

respectively.

### *Equations of Motion*

Equations of motion for the fermionic particle operators are obtained using the standard Heisenberg equation of motion, e.g.,  $\dot{c}_{j,s} = i[\mathcal{H}, c_{j,s}]$ , where

$$\mathcal{H} = \mathcal{H}_{\text{mag}} + \mathcal{H}_{\text{chain}} + \mathcal{H}_{\text{res}} + \mathcal{H}_{\text{mag-chain}} + \mathcal{H}_{\text{chain-res}} \quad (4.9)$$

(we assume  $\hbar = 1$ ). To simplify the notation, the time-dependent and time-independent amplitudes in Eq. (4.4) resulting after the insertion of Eq. (4.3) can be cast as frequency parameters  $\Omega_{\parallel} =$

$-\frac{J}{2}M_{\parallel}$  and  $\Omega_{\perp} = -JM_{\perp}$ . We then obtain

$$\dot{\mathbf{a}}(t) = -i\Omega_{\parallel}\sigma_z\mathbf{a}(t) - i\Omega_{\perp}(\sigma^+e^{i\Omega t} + \sigma^-e^{-i\Omega t})\mathbf{a}(t) + i\gamma_0\mathbf{c}_1(t) \quad (4.10)$$

for the magnetic site and

$$\dot{\mathbf{c}}_1(t) = -i\mathbf{V}_1\mathbf{c}_1(t) + i\gamma_0\mathbf{a}(t) + i\boldsymbol{\tau}_1\mathbf{c}_2(t), \quad (4.11)$$

$$\dot{\mathbf{c}}_j(t) = -i\mathbf{V}_j\mathbf{c}_j(t) + i\boldsymbol{\tau}_{j-1}\mathbf{c}_{j-1}(t) + i\boldsymbol{\tau}_j\mathbf{c}_{j+1}(t), \quad (4.12)$$

with  $1 < j < N$ , and

$$\dot{\mathbf{c}}_N(t) = -i\mathbf{V}_N\mathbf{c}_N(t) + i\boldsymbol{\tau}_{N-1}\mathbf{c}_{N-1}(t) + i\gamma_{\alpha}\mathbf{d}_{\alpha}(t) \quad (4.13)$$

for the chain sites. In the expressions above, we introduced the spinor particle operators  $\mathbf{a} = \begin{pmatrix} a_{\uparrow} \\ a_{\downarrow} \end{pmatrix}$ ,  $\mathbf{c}_j = \begin{pmatrix} c_{j,\uparrow} \\ c_{j,\downarrow} \end{pmatrix}$ , and  $\mathbf{d}_{\alpha} = \begin{pmatrix} d_{\alpha,\uparrow} \\ d_{\alpha,\downarrow} \end{pmatrix}$  and the matrices

$$\boldsymbol{\tau} = \begin{pmatrix} \tau_{\uparrow,\uparrow} & \tau_{\uparrow,\downarrow} \\ \tau_{\downarrow,\uparrow} & \tau_{\downarrow,\downarrow} \end{pmatrix} \quad (4.14)$$

and

$$\mathbf{V}_j = \begin{pmatrix} V_{j,\uparrow} & 0 \\ 0 & V_{j,\downarrow} \end{pmatrix}. \quad (4.15)$$

For the equations of motion of the reservoir operators, we get homogeneous equations for the bulk

and an equation containing an inhomogeneous term due to the coupling to the chain,

$$\dot{\mathbf{d}}_\eta(t) = i \sum_\nu T_{\eta\nu} \mathbf{d}_\nu(t), \quad \eta \neq \alpha, \quad (4.16)$$

and

$$\dot{\mathbf{d}}_\alpha(t) = i\gamma_\alpha \mathbf{c}_N(t) + i \sum_\nu T_{\alpha\nu} \mathbf{d}_\nu(t). \quad (4.17)$$

Combining Eqs. (4.16) and (4.17), we can express the general solution for the operator of the site  $\alpha$  with spin state  $s$  in the integral form

$$d_{\alpha,s}(t) = i \sum_\eta g_{\alpha\eta}^r(t-t_0) d_{\eta,s}(t_0) - \gamma_\alpha \int_{t_0}^\infty g_{\alpha\alpha}^r(t-t') c_{N,s}(t') dt', \quad (4.18)$$

where the homogeneous part of the solution,

$$h_s(t) = i \sum_\eta g_{\alpha\eta}^r(t-t_0) d_{\eta,s}(t_0), \quad (4.19)$$

plays the role of a noise-like term and the inhomogeneous part in Eq. (4.18) is dissipative in nature.[44] In Eqs. (4.18) and (4.19),  $g_{\lambda\eta}^r$  denotes the retarded Green's function of the decoupled reservoir and reads

$$g_{\lambda\eta}^r(t-t') = -i\theta(t-t') \sum_n \phi_n^*(\lambda) \phi_n(\eta) e^{-iE_n(t-t')}, \quad (4.20)$$

where  $\{\phi_n\}$  are the single-particle eigenfunctions of the reservoir with eigenenergy  $\{E_n\}$  (see Appendix A).

In the following, we assume that at a time  $t = t_0$  the reservoir is in thermal equilibrium, such that

$$\langle d_{n,s}^\dagger(t_0) d_{n',s'}(t_0) \rangle = \delta_{n,n'} \delta_{s,s'} f(E_n), \quad (4.21)$$

where  $d_{n,s}(t) = \sum_{\lambda} d_{\lambda,s} \phi_n(\lambda)$ ,  $f(\varepsilon) = 1/[e^{(\varepsilon-\mu)/T} + 1]$  is the Fermi-Dirac distribution, and  $T$  and  $\mu$  and the reservoir's temperature and chemical potential, respectively (we assume  $k_B = 1$ ).

### *Fourier Transform of the Equations of Motion*

It is useful to express the equations of motion in frequency domain. For that purpose, let us use the following convention for the Fourier transform of the particle operators and other time-dependent terms:

$$a_s(t) = \int \frac{d\omega}{2\pi} a_s(\omega) e^{-i\omega t}, \quad (4.22)$$

$$c_{j,s}(t) = \int \frac{d\omega}{2\pi} c_{j,s}(\omega) e^{-i\omega t}, \quad (4.23)$$

$$d_{\lambda,s}(t) = \int \frac{d\omega}{2\pi} d_{\lambda,s}(\omega) e^{-i\omega t}, \quad (4.24)$$

$$h_s(t) = \int \frac{d\omega}{2\pi} h_s(\omega) e^{-i\omega t}, \quad (4.25)$$

and

$$g_{\lambda\eta}^r(t) = \int \frac{d\omega}{2\pi} g_{\lambda\eta}^r(\omega) e^{-i\omega t}. \quad (4.26)$$

Inserting these definitions into Eqs. (4.10) to (4.19), we obtain

$$(\omega - \Omega_{\parallel} \sigma_z) \mathbf{a}(\omega) - \int d\omega' \mathcal{H}_1(\omega, \omega') \mathbf{a}(\omega') = -\gamma_0 \mathbf{c}_1(\omega), \quad (4.27)$$

$$\omega \mathbf{c}_1(\omega) = \mathbf{V}_1 \mathbf{c}_1(\omega) - \gamma_0 \mathbf{a}(\omega) - \tau_1 \mathbf{c}_2(\omega), \quad (4.28)$$

$$\omega \mathbf{c}_j(\omega) = \mathbf{V}_j \mathbf{c}_j(\omega) - \boldsymbol{\tau}_{j-1} \mathbf{c}_{j-1}(\omega) - \boldsymbol{\tau}_j \mathbf{c}_{j+1}(\omega), \quad (4.29)$$

with  $1 < j < N$ ,

$$\omega \mathbf{c}_N(\omega) = \mathbf{V}_N \mathbf{c}_N(\omega) - \boldsymbol{\tau}_{N-1} \mathbf{c}_{N-1}(\omega) - \gamma_\alpha \mathbf{d}_\alpha(\omega), \quad (4.30)$$

and

$$\mathbf{d}_\alpha(\omega) = \mathbf{h}(\omega) - \gamma_\alpha g_{\alpha\alpha}^r(\omega) \mathbf{c}_N(\omega), \quad (4.31)$$

where the Fourier transform of time-dependent part of the Hamiltonian is given by the expression

$$\mathcal{H}_1(\omega, \omega') = \Omega_\perp [\sigma^+ \delta(\omega' - \omega + \Omega) + \sigma^- \delta(\omega' - \omega - \Omega)], \quad (4.32)$$

with  $\sigma^\pm = (\sigma^x \pm i\sigma^y)/2$ , and  $\mathbf{h} = \begin{pmatrix} h_\uparrow \\ h_\downarrow \end{pmatrix}$ . Notice that  $\mathcal{H}_1$  is a  $2 \times 2$  matrix in spin space.

### Charge and Spin Currents

The expression for the charge current follows from the continuity equation in a discrete one-dimensional lattice,

$$\frac{\partial \rho_j}{\partial t} + (J_{j+1}^c - J_j^c) = 0, \quad (4.33)$$

where  $\rho_j = \mathbf{c}_j^\dagger \mathbf{c}_j$  is the charge density operator at the site  $j$  (both the electron charge and the lattice constant are assumed to be unity). Using the equation of motion for  $\mathbf{c}_j$ , the particle current operator



between sites  $j - 1$  and  $j$  can be cast as

$$J_j^c(t) = i \left[ \mathbf{c}_j^\dagger(t) \boldsymbol{\tau}_{j-1} \mathbf{c}_{j-1}(t) - \mathbf{c}_{j-1}^\dagger(t) \boldsymbol{\tau}_{j-1} \mathbf{c}_j(t) \right]. \quad (4.34)$$

One advantage of dynamical spin injection compared to other technique is that the net charge current is zero, see Fig. 4.4.

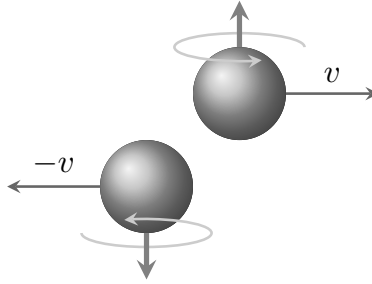


Figure 4.4: Two electrons with opposite spin states travel in opposite direction. The net charge current is zero, but two units of angular momentum are transferred to the right.

The zero charge current in this technique lift the large impedance between FM and NM and makes this technique very efficient for the spin current generation.

To define the spin current, we start first with the case when no spin-orbit coupling is present in the chain, namely, when  $\boldsymbol{\tau}$  is diagonal. Equation (4.34) gives us the total charge current as a sum of spin up and down currents at the site  $j$ . However, to obtain the local spin current we need to keep in mind that when an electron with spin up is moving to left, it produces an effect equivalent to an electron with spin down moving to the right as far as the transfer of angular momentum is concerned. In both cases, up spin angular momentum is transferred to the right. A general expression for spin continuity can be introduced by using the rate of change of magnetization and

the conservation of angular momentum,[45]

$$\frac{\partial \mathbf{s}_j}{\partial t} + (\mathbf{J}_{j+1} - \mathbf{J}_j) = 0, \quad (4.35)$$

where the spin density at the site  $j$  is defined as  $\mathbf{s}_j = \frac{1}{2} \mathbf{c}_j^\dagger \boldsymbol{\sigma} \mathbf{c}_j(t)$  and  $\mathbf{J}_j$  is the spin current operator between sites  $j - 1$  and  $j$ ,

$$\mathbf{J}_j(t) = \frac{i}{2} \left[ \mathbf{c}_j^\dagger(t) \boldsymbol{\sigma} \boldsymbol{\tau}_{j-1} \mathbf{c}_{j-1}(t) - \mathbf{c}_{j-1}^\dagger(t) \boldsymbol{\tau}_{j-1} \boldsymbol{\sigma} \mathbf{c}_j(t) \right], \quad (4.36)$$

which is Hermitian:  $[\mathbf{J}_j(t)]^\dagger = \mathbf{J}_j(t)$ .

Now let us consider the case when there is spin-orbit coupling in the chain. In general, an external torque acting on the spin density at each site has to be included. The source torque can be due to on-site spin scattering process or to spin-orbit terms that cannot be reduced to the divergence of a current. Equation (4.36) still holds for a system with spin-orbit interactions, but an extra source torque term due to on-site spin scattering processes is needed in the continuity equation (4.35), which must be replaced by

$$\frac{\partial \mathbf{s}_j}{\partial t} + (\mathbf{J}_{j+1} - \mathbf{J}_j) = \mathbf{T}_j, \quad (4.37)$$

where the torque at site  $j$  is defined as

$$\mathbf{T}_j = \frac{i}{2} \mathbf{c}_j^\dagger [\boldsymbol{\sigma}, \mathbf{V}_j] \mathbf{c}_j. \quad (4.38)$$

In Ref. [46] it was pointed out that the proper definition of spin current at the macroscopic level requires adding a contribution from the local external torque, such that Eq. (4.35) is restored. In other words, the external torque must be absorbed into the current expression. However, the microscopic nature of our model enables us to distinguish between the transfer of angular momentum either as spin currents or as a conversion to the other degrees of freedom. Therefore, we

will adopt Eq. (4.36) even when spin-orbit coupling is present. In fact, the proper definition of the spin current in the presence of spin-dependent processes has been a source of debate in the literature [47, 48, 49, 50]. One aspect that makes the definition nontrivial is the existence of intrinsic nondissipative background currents. In such systems, even without any dynamical source of current or spin chemical potential difference, a spin current can flow. As Sonin [49, 50] pointed out, regardless of the definition of the spin current, a source torque term is needed to compensate for the transfer of spin angular to orbital angular momentum. In this paper we adopt Eq. (4.36) as the spin current expression. We return to discuss this definition in Sec. 4 when we deriving an expression for the current in presence of spin-orbit interaction.

The Fourier transform of the spin current between sites  $j - 1$  and  $j$  of the chain takes the form

$$\mathbf{J}_j(\omega) = \frac{i}{2} \int \frac{d\omega'}{2\pi} \left[ \mathbf{c}_j^\dagger(\omega') \boldsymbol{\sigma} \boldsymbol{\tau}_{j-1} \mathbf{c}_{j-1}(\omega' + \omega) - \mathbf{c}_{j-1}^\dagger(\omega' - \omega) \boldsymbol{\tau}_{j-1} \boldsymbol{\sigma} \mathbf{c}_j(\omega') \right]. \quad (4.39)$$

Notice that, in Fourier space, the current is no longer Hermitian; instead, it satisfies  $[\mathbf{J}_j(\omega)]^\dagger = \mathbf{J}_j(-\omega)$ . In particular, the  $z$  components of the current can be written as

$$J_j^z(\omega) = J_{j,\uparrow}(\omega) - J_{j,\downarrow}(\omega), \quad (4.40)$$

where

$$J_{j,s}(\omega) = \frac{i}{2} \sum_{s'} \tau_{j-1;s,s'} \int \frac{d\omega'}{2\pi} \left[ c_{j,s}^\dagger(\omega') c_{j-1,s'}(\omega' + \omega) - \eta_s \eta_{s'} c_{j-1,s}^\dagger(\omega' - \omega) c_{j,s'}(\omega') \right], \quad (4.41)$$

and  $\eta_{\uparrow,\downarrow} = \pm 1$ .

Because of the harmonic nature of the precessing magnetization at the  $j = 0$  site, the expecta-

tion value of the Fourier transform of the spin current can be cast as a sum over multiples of the oscillation frequency  $\Omega$ , namely,

$$\langle \mathbf{J}_j(\omega) \rangle = 2\pi \sum_k \mathbf{I}_j(\omega_k) \delta(\omega - \omega_k), \quad (4.42)$$

where  $\omega_k = k\Omega$  and  $k$  is an integer. The stationary (dc) spin current can then be directly related to the zeroth harmonic component,

$$\overline{\langle \mathbf{J}_j(t) \rangle} \equiv \lim_{T \rightarrow \infty} \frac{1}{T} \int_t^{t+T} dt' \langle \mathbf{J}_j(t') \rangle \quad (4.43)$$

$$= \sum_k \mathbf{I}_j(\omega_k) \lim_{T \rightarrow \infty} \frac{e^{-i\omega_k(t+T/2)} \sin\left(\frac{\omega_k T}{2}\right)}{\omega_k T/2} \quad (4.44)$$

$$= \mathbf{I}_j(0). \quad (4.45)$$

### Spin Pumping in the Absence of a Chain

For the sake of simplicity, we first evaluate the spin current for the case  $N = 0$ , when the reservoir is directly connected to the magnetic site. The study of the zero-length chain gives us some insight into the behavior of spin pumping currents and serves to guide us in derivations involving finite-length chains. Following Eq. (4.41), the spin- $s$  component of current in Fourier space reads (the site index can be dropped)

$$J_s(\omega) = \frac{i\gamma}{4\pi} \int d\omega' [d_{\alpha,s}^\dagger(\omega') a_s(\omega' + \omega) - a_s^\dagger(\omega' - \omega) d_{\alpha,s}(\omega')], \quad (4.46)$$

where  $\gamma = \gamma_0 = \gamma_\alpha$ . The equations of motion for the chainless case can be obtained from Eqs. (4.27) and (4.31),

$$(\omega - \Omega_{\parallel} \sigma^z) \mathbf{a}(\omega) - \int d\omega' \mathcal{H}_1(\omega, \omega') \mathbf{a}(\omega') = -\gamma \mathbf{d}_\alpha(\omega), \quad (4.47)$$

and

$$\mathbf{d}_\alpha(\omega) = \mathbf{h}(\omega) - \gamma g_{\alpha\alpha}^r(\omega) \mathbf{a}(\omega). \quad (4.48)$$

We can use Eq. (4.48) to eliminate  $d_{\alpha,s}$  from the expression of the spin- $s$  component of the current,  $J_s(\omega) = J_{j,s}(\omega)$ , by replacing  $c_{j+1,s}$  with  $d_{\alpha,s}$  and  $c_{j,s}$  with  $a_s$  in Eq. (4.41),

$$\begin{aligned} J_s(\omega) = & \frac{i\gamma}{2} \int d\omega' [h_s^\dagger(\omega') a_s(\omega' + \omega) - a_s^\dagger(\omega' - \omega) h_s(\omega')] \\ & - i\gamma^2 \int d\omega' a_s^\dagger(\omega') a_s(\omega' + \omega) \times \{g_{\alpha\alpha}^a(\omega') - g_{\alpha\alpha}^r(\omega' + \omega)\}, \end{aligned} \quad (4.49)$$

recalling that  $[g_{\alpha\alpha}(\omega)]^* = g_{\alpha\alpha}^a(\omega)$ . We can also substitute Eq. (4.48) into the the right-hand side of Eq. (4.47) to get

$$\int d\omega' \{ \omega \sigma^0 \delta(\omega - \omega') - [\mathcal{H}_0 + \mathcal{H}_1 + \Sigma^r](\omega, \omega') \} \mathbf{a}(\omega') = -\gamma \mathbf{h}(\omega), \quad (4.50)$$

where the static and the dynamic parts of Hamiltonian are

$$\mathcal{H}_0(\omega, \omega') = \Omega_{\parallel} \sigma^z \delta(\omega - \omega') \quad (4.51)$$

and

$$\mathcal{H}_1(\omega, \omega') = \Omega_{\perp} [\sigma^+ \delta(\omega - \omega' - \Omega) + \sigma^- \delta(\omega - \omega' + \Omega)], \quad (4.52)$$

respectively. The self energy due to the reservoir is given by

$$\Sigma^r(\omega, \omega') = \gamma^2 g_{\alpha\alpha}^r(\omega) \sigma^0 \delta(\omega - \omega') \quad (4.53)$$

and  $\sigma^0$  denotes the identity operator in spin space. Further simplification is possible by treating the right-hand side of Eq. (4.50) as a nonhomogeneous term and by writing the magnetic-site particle operator in terms of the fully-dressed Green's function of that site,

$$a_s(\omega) = -\gamma \sum_{s'} \int d\omega' G_{ss'}^r(\omega, \omega') h_{s'}(\omega'), \quad (4.54)$$

where

$$\int d\omega'' \{ \omega \sigma^0 \delta(\omega - \omega'') - [\mathcal{H}_0 + \mathcal{H}_1 + \Sigma^r](\omega, \omega'') \} G^r(\omega'', \omega') = \sigma^0 \delta(\omega - \omega'). \quad (4.55)$$

Thus, we can express the magnetic-site operator  $c_{0,s}$  entirely in terms of the noise-like operator  $h_s$ . In the limit of  $t_0 \rightarrow -\infty$ , it is possible to show that the correlation function for  $h_s(\omega)$  is diagonal in spin and frequency (see Appendix A),

$$\langle h_s^\dagger(\omega) h_{s'}(\omega') \rangle = \delta_{s,s'} \delta(\omega' - \omega) I_\alpha(\omega), \quad (4.56)$$

where  $I_\alpha(\omega) = \rho_\alpha(\omega) f(\omega)$  and  $\rho_\alpha(\omega)$  is the reservoir's density of states at the site  $\alpha$ ,

$$\rho_\alpha(\omega) = -\frac{1}{\pi} \Im [g_{\alpha\alpha}^r(\omega)] \quad (4.57)$$

$$= \sum_n |\phi_n(\alpha)|^2 \delta(\omega - E_n). \quad (4.58)$$

Using Eqs. (4.56) and (4.54), one arrives at the following expression for the expectation value of

the spin- $s$  component of the current:

$$\langle J_s(\omega) \rangle = \frac{i\gamma^2}{2} \int d\omega' \{ \mathcal{F}_s(\omega, \omega') + \mathcal{I}_s(\omega, \omega') [g_{\alpha\alpha}^r(\omega' + \omega) - g_{\alpha\alpha}^a(\omega')] \}, \quad (4.59)$$

where  $\mathcal{F}$  and  $\mathcal{I}$  are functions of the magnetic-site Green's functions  $G^{r,a}$ , with  $G^a = (G^r)^\dagger$ ,

$$\mathcal{F}_s(\omega, \omega') = [G_{ss}^a(\omega', \omega' - \omega) - G_{ss}^r(\omega' + \omega, \omega')] I_\alpha(\omega') \quad (4.60)$$

and

$$\mathcal{I}_s(\omega, \omega') = \gamma^2 \int d\omega'' \sum_{s'} G_{ss'}^a(\omega'', \omega') G_{s's}^r(\omega' + \omega, \omega'') I_\alpha(\omega''). \quad (4.61)$$

As we argue in Sec. 4, from the perturbative expansion of the Green's function in powers  $\Omega_\perp$ , we know that even terms are diagonal in both spin and frequency, while odd terms are only nonzero when they involve opposite spin indices. Therefore, in general, one can write

$$G_{ss}(\omega, \omega') = \delta(\omega - \omega') D_s(\omega), \quad (4.62)$$

leading to

$$\mathcal{F}_s(\omega, \omega') = \delta(\omega) \Im [D_s^r(\omega')] I_\alpha(\omega'). \quad (4.63)$$

It is then useful to rewrite  $\mathcal{I}_s$  in terms of same-spin-state and opposite-spin-state Green's functions, namely,

$$\begin{aligned} \mathcal{I}_s(\omega, \omega') &= \gamma^2 \int d\omega'' [G_{ss}^a(\omega'', \omega') G_{ss}^r(\omega' + \omega, \omega'') \\ &\quad + G_{s\bar{s}}^a(\omega'', \omega') G_{s\bar{s}}^r(\omega' + \omega, \omega'')] I_\alpha(\omega''). \end{aligned} \quad (4.64)$$

Using the Green's function relation

$$G^r - G^a = G^r [\Sigma^r - \Sigma^a] G^a, \quad (4.65)$$

it is possible to show that the first term in the integrand on the right-hand side of Eq. (4.64) cancels  $\mathcal{F}_s$  exactly, leading to

$$\begin{aligned} \langle J_s(\omega) \rangle &= -\frac{i\gamma^4}{2} \int d\omega' \int d\omega'' G_{\bar{s}s}^a(\omega'', \omega') G_{s\bar{s}}^r(\omega' + \omega, \omega'') \\ &\quad \times I_\alpha(\omega'') [g_{\alpha\alpha}^a(\omega') - g_{\alpha\alpha}^r(\omega' + \omega)], \end{aligned} \quad (4.66)$$

which is the central result of this Section.

Following similar steps, one can derive expressions for the other spin components of the current.

The results can be combined into a single expression that generalizes Eq. (4.59), namely,

$$\langle \mathbf{J}(\omega) \rangle = \frac{i\gamma^2}{2} \int \frac{d\omega'}{2\pi} \{ \mathbf{F}(\omega, \omega') + \mathbf{I}(\omega, \omega') [g_{\alpha\alpha}^r(\omega' + \omega) - g_{\alpha\alpha}^a(\omega')] \}, \quad (4.67)$$

where

$$\mathbf{F}(\omega, \omega') = \sum_{s,s'} \boldsymbol{\sigma}_{ss'} [G_{s's}^a(\omega', \omega' - \omega) - G_{s's}^r(\omega' + \omega, \omega')] I_\alpha(\omega') \quad (4.68)$$

and

$$\mathbf{I}(\omega, \omega') = \gamma^2 \int d\omega'' \sum_{s,s',s_1} G_{s_1s}^a(\omega'', \omega') \boldsymbol{\sigma}_{ss'} G_{s's_1}^r(\omega' + \omega, \omega'') I_\alpha(\omega''). \quad (4.69)$$



*Perturbative Expansion in  $\Omega_{\perp}$*

In most situations of experimental relevance,[51, 52] the transverse amplitude of time-dependent field driving the magnetization precession in the FM is much smaller than the longitudinal static component, resulting in  $\Omega_{\perp} \ll \Omega_{\parallel}$ . We consider this regime and expand the magnetic-site Green's function in powers of  $\Omega_{\perp}$ , namely, in powers of the time-dependent Hamiltonian term  $\mathcal{H}_1$ :

$$G = G^{(0)} + G^{(0)} \mathcal{H}_1 G^{(0)} + G^{(0)} \mathcal{H}_1 G^{(0)} \mathcal{H}_1 G^{(0)} + \dots \quad (4.70)$$

The zeroth-order (static) magnetic-site Green's function  $G^{(0)}$  is obtained by solving Eq. (4.55) when  $\mathcal{H}_1$  is absent, yielding

$$G_{ss'}^{(0)}(\omega, \omega') = \delta_{s,s'} \delta(\omega - \omega') \mathcal{G}_s(\omega), \quad (4.71)$$

where

$$\mathcal{G}_s(\omega) = \frac{1}{\omega - \eta_s \Omega_{\parallel} - \gamma^2 g_{\alpha\alpha}(\omega)} \quad (4.72)$$

and  $\eta_{\uparrow,\downarrow} = \pm 1$ . Thus, the zeroth-order Green's function is diagonal in spin space.

The first-order Green's function has only off-diagonal spin terms,

$$G_{\uparrow\uparrow}^{(1)}(\omega, \omega') = 0, \quad (4.73)$$

$$G_{\uparrow\downarrow}^{(1)}(\omega, \omega') = \Omega_{\perp} \delta(\omega' - \omega - \Omega) G_{\uparrow}^{(0)}(\omega) G_{\downarrow}^{(0)}(\omega + \Omega), \quad (4.74)$$

$$G_{\downarrow\uparrow}^{(1)}(\omega, \omega') = \Omega_{\perp} \delta(\omega' - \omega + \Omega) G_{\downarrow}^{(0)}(\omega) G_{\uparrow}^{(0)}(\omega - \Omega), \quad (4.75)$$

$$G_{\downarrow\downarrow}^{(1)}(\omega, \omega') = 0, \quad (4.76)$$

while the second-order Green's function recovers the spin-diagonal structure of the zeroth-order

case,

$$G_{\uparrow\uparrow}^{(2)}(\omega, \omega') = \Omega_{\perp}^2 \delta(\omega' - \omega) G_{\uparrow}^{(0)}(\omega) G_{\uparrow}^{(0)}(\omega) G_{\downarrow}^{(0)}(\omega + \Omega), \quad (4.77)$$

$$G_{\uparrow\downarrow}^{(2)}(\omega, \omega') = 0, \quad (4.78)$$

$$G_{\downarrow\uparrow}^{(2)}(\omega, \omega') = 0, \quad (4.79)$$

$$G_{\downarrow\downarrow}^{(2)}(\omega, \omega') = \Omega_{\perp}^2 \delta(\omega' - \omega) G_{\downarrow}^{(0)}(\omega) G_{\downarrow}^{(0)}(\omega) G_{\uparrow}^{(0)}(\omega - \Omega). \quad (4.80)$$

The spin dependence of higher order contributions to the Green's function repeats this pattern: diagonal for even orders and off-diagonal for odd orders. In addition, even orders are also diagonal in the frequency variables.

### *Spin Current Components*

From the final expression for the spin- $s$  state component of the current, Eq. (4.66), and the expansion of the Green's function up to second order in  $\Omega_{\perp}$ , one finds the following expression for the  $z$ -component of the spin current:

$$\begin{aligned} \langle J^z(\omega) \rangle &= \delta(\omega) \pi \gamma^4 \Omega_{\perp}^2 \int d\omega' \rho_{\alpha}(\omega') \\ &\times \left[ |\mathcal{G}_{\uparrow}^r(\omega')|^2 |\mathcal{G}_{\downarrow}^r(\omega' + \Omega)|^2 I_{\alpha}(\omega' + \Omega) - |\mathcal{G}_{\downarrow}^r(\omega')|^2 |\mathcal{G}_{\uparrow}^r(\omega' - \Omega)|^2 I_{\alpha}(\omega' - \Omega) \right] \\ &+ O(\Omega_{\perp}^4). \end{aligned} \quad (4.81)$$

Since only the zero-frequency component is nonzero, upon returning to the time representation and utilizing Eq. (4.45), this relation yields a nonzero dc current, namely,

$$\begin{aligned} \overline{\langle J^z(t) \rangle} &= \frac{\gamma^4 \Omega_{\perp}^2}{2} \int d\omega \rho_{\alpha}(\omega - \Omega/2) \rho_{\alpha}(\omega + \Omega/2) \\ &\quad \times |\mathcal{G}_{\uparrow}^r(\omega - \Omega/2)|^2 |\mathcal{G}_{\downarrow}^r(\omega + \Omega/2)|^2 [f(\omega + \Omega/2) - f(\omega - \Omega/2)] \\ &\quad + O(\Omega_{\perp}^4), \end{aligned} \tag{4.82}$$

where we have symmetrized the frequency integrand for convenience.

We notice that inverting the static magnetic field and the direction of precession (e.g.,  $\Omega \rightarrow -\Omega$  and  $\Omega_{\parallel} \rightarrow -\Omega_{\parallel}$ ) flips the spin of the zeroth-order Green's function  $\mathcal{G}_{\uparrow}(\omega) \rightarrow \mathcal{G}_{\downarrow}(\omega)$ . As a result, the spin current reverses its direction. This is expected on the basis of time-reversal symmetry. Moreover, at zero precession or zero transverse magnetic field, the spin current vanishes.

Considering now the  $x$  component of the integral  $\mathbf{F}$  in Eq. (4.68), we obtain

$$F^x = -\gamma [G_{\downarrow\uparrow}^a(\omega', \omega' - \omega) - G_{\downarrow\uparrow}^r(\omega' + \omega, \omega') + G_{\uparrow\downarrow}^a(\omega', \omega' - \omega) - G_{\uparrow\downarrow}^r(\omega' + \omega, \omega')] I_{\alpha}(\omega'). \tag{4.83}$$

Notice that all terms contain opposite-spin-state Green's functions, thus vanish in even powers in  $\Omega_{\perp}$  but are  $\Omega$ -dependent in odd powers of  $\Omega_{\perp}$ . As a result, in the time domain,  $F^x$  oscillates and, upon averaging over one precession period, it vanishes. A similar argument can be used to show that  $I^x$  vanishes as well. Therefore, all transverse components of the spin current vanish when averaged over time.

### *Interface Parameters*

The dynamics of the FM magnetization in the adiabatic approximation is governed by the Landau-Lifshitz-Gilbert (LLG) equation,

$$\frac{d\mathbf{m}}{dt} = \gamma \mathbf{m} \times \mathbf{H}_{\text{eff}} + \alpha \mathbf{m} \times \frac{d\mathbf{m}}{dt}, \quad (4.84)$$

where  $\mathbf{m}$  is the magnetization unit vector,  $\gamma$  is the gyromagnetic ratio,  $\mathbf{H}_{\text{eff}}$  is the effective magnetic field (including the external magnetic field and the local demagnetization field), and  $\alpha$  is the Gilbert damping parameter. In the absence of any contact between the FM and a NM, the relaxation of the magnetization occurs entirely through processes internal to the FM, which are phenomenologically accounted for by the parameter  $\alpha$ . When a NM is brought in contact with the FM, the magnetization relaxation can also happen through angular momentum leaking into the NM as a spin current. To account for this contribution, consider that the effective magnetic field applied to the FM to be of the form

$$\mathbf{H}_{\text{eff}} = h_x(t) \hat{\mathbf{x}} + h_y(t) \hat{\mathbf{y}} + H_{\parallel} \hat{\mathbf{z}}, \quad (4.85)$$

where  $H_{\parallel}$  is the static component of the field while  $h_x$  and  $h_y$  are the time-dependent components. Following the scattering theory of spin pumping,[8] the spin current can be expressed as

$$\mathbf{I}_{\text{spin}} = \frac{1}{4\pi} g_{\uparrow\downarrow} \mathbf{m} \times \frac{d\mathbf{m}}{dt}, \quad (4.86)$$

where the mixing conductance  $g_{\uparrow\downarrow}$  is defined in terms of reflection matrices as

$$g^{\uparrow\downarrow} = \sum_{m,n} (\delta_{m,n} - r_{mn}^{\uparrow} r_{mn}^{\downarrow}), \quad (4.87)$$

with the sum taken over transverse conducting channels. Notice the similarity of the right-hand side of Eq. (4.86) with the The Gilbert damping term in Eq. (4.84). One can absorb the angular momentum leakage contribution on the magnetization relaxation due to the spin current by substituting  $\alpha$  with  $\alpha'$  in Eq. (4.84), where

$$\alpha' = \alpha + \frac{g_L A_r}{4\pi M}. \quad (4.88)$$

Here,  $g_L$  is the Landé factor,  $M$  is the total (bulk) magnetization of the FM, and  $A_r = \Re g^{\uparrow\downarrow}$  (in most practical situations, the imaginary component of the mixing conductance can be neglected).

In the small precessing field approximation,  $h_{\perp} = \sqrt{h_x^2 + h_y^2} \ll |H_{\parallel}|$ , one can solve the LLG equation for the stationary solution of the dynamics of magnetization to get

$$m_{\perp}(t) = |m_{\perp}| e^{-i(\Omega t + \delta)}, \quad (4.89)$$

where

$$|m_{\perp}| = \frac{\gamma M h_{\perp}}{\sqrt{(\alpha' M \Omega)^2 + (\gamma H_{\parallel} + \Omega)^2}} \quad (4.90)$$

and

$$\tan \delta = \frac{\alpha' M \Omega}{\gamma H_{\parallel} + \Omega}. \quad (4.91)$$

After substituting  $m_{\perp}(t)$  in Eq. (4.86), we arrive at

$$I_{\text{spin}}^z = \frac{1}{4\pi} \Omega |m_{\perp}|^2 g_{\uparrow\downarrow}. \quad (4.92)$$

We can combine this expression with that obtained in Sec. 4 for the spin current in terms of the system's Green's function, Eq. (4.82) to obtain an expression for the mixing conductance in terms

of Green's functions,

$$g^{\uparrow\downarrow} = \frac{\pi J^2 \gamma^4}{2\hbar} \int d\omega \rho_\alpha^2(\omega) |\mathcal{G}_\uparrow^r(\omega)|^2 |\mathcal{G}_\downarrow^r(\omega)|^2 \frac{df(\omega)}{d\omega}. \quad (4.93)$$

In experiments, there are two standard approaches to quantify the spin pumping current and both are indirect. The first and most common consists of measuring the broadening of the FMR spectrum and utilizing Eqs. (4.88) and (4.92).[53, 52, 54] The second is to infer the current magnitude through the observation of the *inverse spin Hall effect* (ISHE) in the NM when a sufficiently strong spin-orbit coupling is present.[55, 56, 57] Although, the latter seems more direct, the relation between the measured ISHE voltage and the actual spin current depends on various materials parameters which are often not accurately known.[58] Equation (4.93) provides a useful relation between the physical properties of medium where the spin current is generated propagates to the enhanced broadening of FMR due to the angular momentum leakage.

### Spin Pumping with a Finite Chain

The formulation developed for the  $N = 0$  chain in Sec. 4 can be extended to a finite-length chain. The equivalent to the equation of motion (4.50) for the particle operators in the chain can be written as

$$\sum_{j'=0}^N \sum_{s'} \int d\omega' \mathcal{Z}_{j,s;j',s'}^r(\omega, \omega') c_{j',s'}(\omega') = -\gamma_\alpha \delta_{j,N} h_s(\omega), \quad (4.94)$$

where  $0 \leq j \leq N$  and we introduced  $c_{0,s} \equiv a_s$ . The matrix  $\mathcal{Z}^r$  can be split into two contributions,

$$\mathcal{Z}^r = \mathcal{Z}_0^r + \mathcal{Z}_1^r, \quad (4.95)$$

where

$$\begin{aligned}
[\mathcal{Z}_0^r]_{j,s;j',s'}(\omega, \omega') &= \delta_{s,s'} \delta(\omega - \omega') \{ \delta_{j,j'} \delta_{j,0} [(\omega - \Omega_{\parallel}) \delta_{s,\uparrow} + (\omega + \Omega_{\parallel}) \delta_{s,\downarrow}] \\
&\quad + (\omega - V_{j,s}) \delta_{j,j'} - \delta_{j,j'} \delta_{j,N} \gamma_{\alpha}^2 g_{\alpha\alpha}^r(\omega) \} \\
&\quad + \delta(\omega - \omega') (\delta_{j,j'+1} \tau_{j-1;s,s'} + \delta_{j,j'-1} \tau_{j;s,s'}).
\end{aligned} \tag{4.96}$$

and

$$[\mathcal{Z}_1^r]_{j;j'}(\omega, \omega') = \delta_{j,0} \delta_{j',0} \Omega_{\perp} [\sigma^+ \delta(\omega' - \omega - \Omega) + \sigma^- \delta(\omega' - \omega + \Omega)]. \tag{4.97}$$

Let us define the retarded Green's function of the finite chain as  $G^r \equiv (\mathcal{Z}^r)^{-1}$ . We can then solve Eq. (4.94) for the particle operator and write

$$c_{j,s}(\omega) = -\gamma_{\alpha} \sum_{s'} \int d\omega' G_{j,s;N,s'}^r(\omega, \omega') h_{s'}(\omega'), \tag{4.98}$$

where  $0 \leq j \leq N$ . The Green's function can be expanded in powers of  $\Omega_{\perp}$  similarly to Eq. (4.70).

Since  $\mathcal{Z}^{(0)}$  is diagonal in frequency, one can write the zeroth order term as

$$G_{j,s;j',s'}^{(0)}(\omega, \omega') = \delta(\omega - \omega') \mathcal{G}_{j,s;j',s'}(\omega). \tag{4.99}$$

Using this expression, the first-order contribution is found to be

$$\begin{aligned}
G_{j,s;j',s'}^{(1)}(\omega, \omega') &= \Omega_{\perp} [\mathcal{G}_{j,s;0,\uparrow}(\omega) \mathcal{G}_{0,\downarrow;j',s'}(\omega + \Omega) \delta(\omega' - \omega - \Omega) \\
&\quad + \mathcal{G}_{j,s;0,\downarrow}(\omega) \mathcal{G}_{0,\uparrow;j',s'}(\omega - \Omega) \delta(\omega' - \omega + \Omega)].
\end{aligned} \tag{4.100}$$

Similarly, for the second-order contribution we have

$$\begin{aligned}
G_{j,s;j',s'}^{(2)}(\omega, \omega') &= \Omega_{\perp}^2 [\delta(\omega' - \omega - 2\Omega) \mathcal{G}_{j,s;0,\uparrow}(\omega) \mathcal{G}_{0,\downarrow;0,\uparrow}(\omega + \Omega) \mathcal{G}_{0,\downarrow;j's'}(\omega') \\
&\quad + \delta(\omega' - \omega + 2\Omega) \mathcal{G}_{j,s;0,\downarrow}(\omega) \mathcal{G}_{0,\uparrow;\downarrow,0}(\omega - \Omega) \mathcal{G}_{0,\uparrow;j's'}(\omega') \\
&\quad + \delta(\omega' - \omega) \mathcal{G}_{j,s;0,\uparrow}(\omega) \mathcal{G}_{0,\downarrow;0,\downarrow}(\omega + \Omega) \mathcal{G}_{0,\uparrow;j's'}(\omega') \\
&\quad + \delta(\omega' - \omega) \mathcal{G}_{j,s;0,\downarrow}(\omega) \mathcal{G}_{0,\uparrow;0,\uparrow}(\omega - \Omega) \mathcal{G}_{0,\downarrow;j's'}(\omega')]. \tag{4.101}
\end{aligned}$$

Notice that in the absence of spin-orbit coupling in the chain,  $\mathcal{G}_{0,\downarrow;\uparrow,0} = \mathcal{G}_{0,\uparrow;\downarrow,0} = 0$  and the inelastic (off diagonal in frequency) contribution to the second-order Green's function vanishes.

### *Current in the Presence of Spin-Orbit Coupling*

If electrons experience no spin scattering in the chain, the spin  $s$ -state current flows homogeneously from the magnetic site, along the chain, and into the reservoir without spin-orbit coupling. Thus, It can be shown that the spin current will remain the same as Eq. (4.82).

When spin-orbit is present, the spin current will vary along the chain. In this case, one is required to use Eq. (4.39) to compute the three components of the spin current at a given site  $j$ . Let us focus on the  $z$  component. Substituting Eq. (4.98) and its Hermitian conjugate into Eq. (4.39), we obtain

$$\begin{aligned}
J_j^z(\omega) &= \frac{i\gamma_{\alpha}^2}{4\pi} \int d\omega' \int d\omega'' \int d\omega''' \\
&\quad \times \mathbf{h}^{\dagger}(\omega'') [\mathbf{G}_{N;j}^a(\omega'', \omega') \sigma^z \boldsymbol{\tau}_{j-1} \mathbf{G}_{j-1;N}^r(\omega' + \omega, \omega''') \\
&\quad - \mathbf{G}_{N;j-1}^a(\omega'', \omega' - \omega) \boldsymbol{\tau}_{j-1} \sigma^z \mathbf{G}_{j;N}^r(\omega', \omega''')] \mathbf{h}(\omega'''), \tag{4.102}
\end{aligned}$$

where  $0 \leq j \leq N$  and  $\mathbf{G}_{j;j}^{r(a)}$  denotes the  $2 \times 2$  retarded (advanced) Green's function connecting



sites  $j$  and  $j'$ . Using the correlation function introduced in Eq. (4.56), we can take the expectation value of Eq. (4.102) to obtain

$$\begin{aligned} \langle J_j^z(\omega) \rangle &= \frac{i\gamma_\alpha^2}{4\pi} \int d\omega' \int d\omega'' I_\alpha(\omega'') \\ &\times \text{tr} \left[ \mathbf{G}_{N;j}^a(\omega'', \omega') \sigma^z \boldsymbol{\tau}_{j-1} \mathbf{G}_{j-1;N}^r(\omega' + \omega, \omega'') \right. \\ &\left. - \mathbf{G}_{N;j-1}^a(\omega'', \omega' - \omega) \boldsymbol{\tau}_{j-1} \sigma^z \mathbf{G}_{j;N}^r(\omega', \omega'') \right]. \end{aligned} \quad (4.103)$$

where the trace is over spin variables. Equation (4.103) is one of the main results of this paper. It provides a framework for computing the  $z$  component of the spin current at any site within the chain that connects the magnetic site and the reservoir. Unfortunately, any further simplification of this expression is daunting. Similarly to the case where the reservoir is connected directly to the magnetic site, Sec. 4, we can use the perturbative expansion of the Green's function in powers of  $\Omega_\perp$ . The result is still rather involved if the spin-dependent hopping amplitude  $\boldsymbol{\tau}$  is kept general and is not presented here.

A more compact expression can be obtained for the spin current between the last site of the chain and the reservoir, even in the presence of a general spin-orbit hopping amplitude. For that purpose, we take a step back, set  $j = \alpha$  in Eq. (4.39), and consider the  $z$  component of the spin current operator,

$$J_\alpha^z(\omega) = \frac{i\gamma_\alpha}{4\pi} \int d\omega' \sum_s \eta_s \left[ d_s^\dagger(\omega') c_{N,s}(\omega' + \omega) c_{N,s}^\dagger(\omega' - \omega) d_s(\omega') \right].$$

Using Eqs. (4.31) and (4.98), taking the expectation value, and using Eq. (4.56), we can rewrite

Eq. (4.104) as

$$\begin{aligned} \langle J_\alpha^z(\omega) \rangle &= -\frac{i\gamma_\alpha^2}{4\pi} \int d\omega' \sum_s \eta_s \left\{ I_\alpha(\omega') [G_{N,s;N,s}^r(\omega' + \omega, \omega') - G_{N,s;N,s}^a(\omega', \omega' - \omega)] \right. \\ &\quad \left. - \gamma_\alpha^2 \int d\omega'' \sum_{s'} I_\alpha(\omega'') [g_{\alpha\alpha}^r(\omega') - g_{\alpha\alpha}^a(\omega' + \omega)] G_{N,s';N,s}^a(\omega'', \omega') G_{N,s;N,s'}^r(\omega' + \omega, \omega'') \right\}. \end{aligned} \quad (4.104)$$

The absence of a spin-dependent hopping amplitude in Eq. (4.104) makes it more amenable to an analytical treatment. Focusing on the dc component of the spin current, as shown in Eqs. (4.42) and (4.45), we expand the Green's function harmonics of the precessing frequency  $\Omega$ , namely,

$$G(\omega, \omega') = \delta(\omega' - \omega) D_0(\omega) + \sum_{k \neq 0} \delta(\omega' - \omega - k\Omega) D_k(\omega). \quad (4.105)$$

Inserting this expansion into Eq. (4.104) and keeping only the terms corresponding to the dc limit, we obtain

$$\begin{aligned} \langle J_\alpha^z(\omega) \rangle_{\text{dc}} &= -\frac{i\gamma_\alpha^2}{4\pi} \delta(\omega) \int d\omega' \sum_s \eta_s \left\{ I_\alpha(\omega') [D_{0;N,s;N,s}^r(\omega') - D_{0;N,s;N,s}^a(\omega')] \right. \\ &\quad - \gamma_\alpha^2 [g_{\alpha\alpha}^r(\omega') - g_{\alpha\alpha}^a(\omega')] I_\alpha(\omega') \sum_{s'} D_{0;N,s;N,s'}^r(\omega') D_{0;N,s';N,s}^a(\omega') \\ &\quad \left. - \gamma_\alpha^2 [g_{\alpha\alpha}^r(\omega') - g_{\alpha\alpha}^a(\omega')] \sum_{k \neq 0} I_\alpha(\omega' + k\Omega) \sum_{s'} D_{k;N,s;N,s'}^r(\omega') D_{-k;N,s';N,s}^a(\omega' + k\Omega) \right\}. \end{aligned} \quad (4.106)$$

We can now use the relations

$$G^r - G^a = [Z^r]^{-1} - [Z^a]^{-1} = G^r (Z^a - Z^r) G^a, \quad (4.107)$$

where

$$[Z^a - Z^r]_{j,s;j',s'}(\omega, \omega') = -\gamma_\alpha^2 \delta_{j,j} \delta_{j,N} \delta_{s,s'} \delta(\omega - \omega') [g_{\alpha\alpha}^a(\omega) - g_{\alpha\alpha}^r(\omega)], \quad (4.108)$$

to find

$$\begin{aligned} D_{0;N,s;N,s}^r(\omega) - D_{0;N,s;N,s}^a(\omega) &= \gamma_\alpha^2 [g_{\alpha\alpha}^r(\omega) - g_{\alpha\alpha}^a(\omega)] \sum_{s'} D_{0;N,s;N,s'}^r(\omega) D_{0;N,s';N,s}^a(\omega) \\ &+ \gamma_\alpha^2 \sum_{k \neq 0} [g_{\alpha\alpha}^r(\omega + k\Omega) - g_{\alpha\alpha}^a(\omega + k\Omega)] \\ &\times \sum_{s'} D_{k;N,s;N,s'}^r(\omega) D_{-k;N,s',N,s}^a(\omega + k\Omega). \end{aligned} \quad (4.109)$$

Combing Eqs. (4.106) and (4.109), recalling that  $g_{\alpha\alpha}^r(\omega) - g_{\alpha\alpha}^a(\omega) = -2\pi i \rho_\alpha(\omega)$  and using Eq. (4.57), we arrive at

$$\begin{aligned} \langle J_\alpha^z(\omega) \rangle_{\text{dc}} &= -\frac{\gamma_\alpha^4}{2} \delta(\omega) \int d\omega' \sum_{k \neq 0} \rho_\alpha(\omega') \rho_\alpha(\omega' + k\Omega) [f(\omega') - f(\omega' + k\Omega)] \\ &\times \sum_{s,s'} \eta_s D_{k;N,s;N,s'}^r(\omega') D_{-k;N,s',N,s}^a(\omega' + k\Omega). \end{aligned} \quad (4.110)$$

Symmetrizing the frequency integration, we finally obtain the following expression for the dc spin current at the interface with the reservoir:

$$\begin{aligned} \overline{\langle J_\alpha^z(t) \rangle} &= \frac{\gamma_\alpha^4}{2} \int d\omega \sum_{k > 0} \rho_\alpha(\omega + k\Omega/2) \rho_\alpha(\omega - k\Omega/2) [f(\omega + k\Omega/2) - f(\omega - k\Omega/2)] \\ &\times \text{tr} \left\{ \sigma^z \left[ D_{k;N;N}^r(\omega - k\Omega/2) D_{-k;N;N}^a(\omega + k\Omega/2) \right. \right. \\ &\left. \left. - D_{-k;N;N}^r(\omega + k\Omega/2) D_{k;N;N}^a(\omega - k\Omega/2) \right] \right\}, \end{aligned} \quad (4.111)$$

where the trace is over spin indices. Notice that in the limit of zero pumping frequency ( $\Omega \rightarrow 0$ ), the spin current goes to zero.

At this point, we can go back to the perturbative expansion of the Green's functions in powers of  $\Omega_\perp$  and notice the following:

$$D_{-1;j,s;j',s'}(\omega) = \Omega_\perp \mathcal{G}_{j,s;0,\downarrow}(\omega) \mathcal{G}_{0,\uparrow;j',s'}(\omega - \Omega) + O(\Omega_\perp^3), \quad (4.112)$$

and

$$D_{1;j,s;j',s'}(\omega) = \Omega_\perp \mathcal{G}_{j,s;0,\uparrow}(\omega) \mathcal{G}_{0,\downarrow;j',s'}(\omega + \Omega) + O(\Omega_\perp^3). \quad (4.113)$$

Since  $D_k \sim O(\Omega_\perp^k)$ , by keeping only the leading term in powers of  $\Omega_\perp$  we obtain

$$\begin{aligned} \overline{\langle J_\alpha^z(t) \rangle} &= \frac{\gamma_\alpha^4 \Omega_\perp^2}{2} \int d\omega \rho_\alpha(\omega + \Omega/2) \rho_\alpha(\omega - \Omega/2) [f(\omega + \Omega/2) - f(\omega - \Omega/2)] \\ &\times \sum_{s,s'} \eta_s \left[ |\mathcal{G}_{N,s;0,\uparrow}^r(\omega - \Omega/2)|^2 |\mathcal{G}_{0,\downarrow;N,s'}^r(\omega + \Omega/2)|^2 \right. \\ &\left. - |\mathcal{G}_{N,s;0,\downarrow}^r(\omega + \Omega/2)|^2 |\mathcal{G}_{0,\uparrow;N,s'}^r(\omega - \Omega/2)|^2 \right] + O(\Omega_\perp^4). \end{aligned} \quad (4.114)$$

It is straightforward to verify that setting  $N = 0$  in Eq. (4.114) leads to Eq. (4.82). Notice that for  $\Omega \ll T, \mu$ , the current is proportional to  $\Omega$ ,

$$\begin{aligned} \overline{\langle J_\alpha^z(t) \rangle} &\approx \frac{\gamma_\alpha^4 \Omega_\perp^2 \Omega}{2} \int d\omega [\rho_\alpha(\omega)]^2 \left[ \frac{df(\omega)}{d\omega} \right] \\ &\sum_{s,s'} \eta_s \left[ |\mathcal{G}_{N,s;0,\uparrow}^r(\omega)|^2 |\mathcal{G}_{0,\downarrow;N,s'}^r(\omega)|^2 - |\mathcal{G}_{N,s;0,\downarrow}^r(\omega)|^2 |\mathcal{G}_{0,\uparrow;N,s'}^r(\omega)|^2 \right]. \end{aligned} \quad (4.115)$$

To illustrate the results obtained so far, we performed numerical calculations of the chain Green's function for chains of various lengths in the presence and absence of spin-dependent on-site potentials.

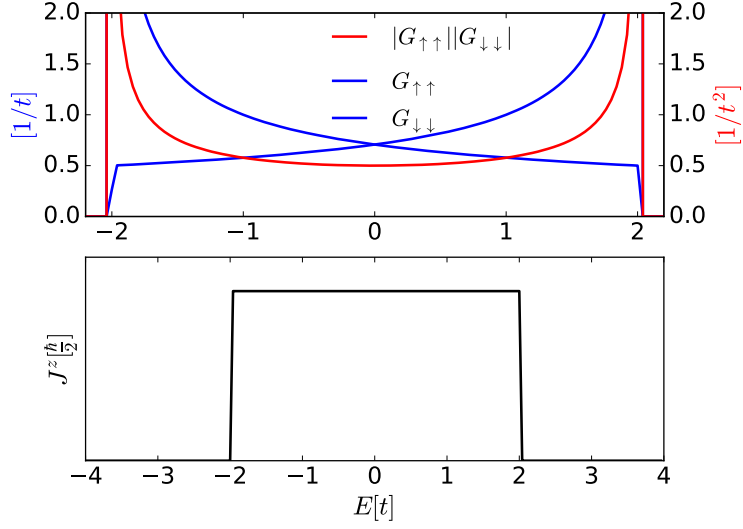


Figure 4.5: (upper panel) Spin-diagonal components of the Green's function across the chain,  $G_{N,s;0,s}$ , in a clean (translation invariant) chain in the absence of spin-orbit coupling as a function of energy. (lower panel) The dependence of the  $z$ -component of the spin current on the reservoir's Fermi energy. Both plots were obtained using parameters value such that  $\gamma_{\alpha}^2 \Omega_{\perp}^2 \Omega = 2$ .

In Fig. 4.5, the spin-diagonal components of the Green's function across the chain,  $G_{N,s;0,s}^{(0)}(E)$ , and the total spin pumping current,  $\langle J_{\alpha}^z(E) \rangle$ , are plotted as functions of energy. A constant spin current over energy confirms that, in the absence of spin-scattering centers, the chain is a spin-degenerate ballistic propagating channel so long as the energy  $E$  is within the energy band. In this case, the spin current is independent of the length of the chain.

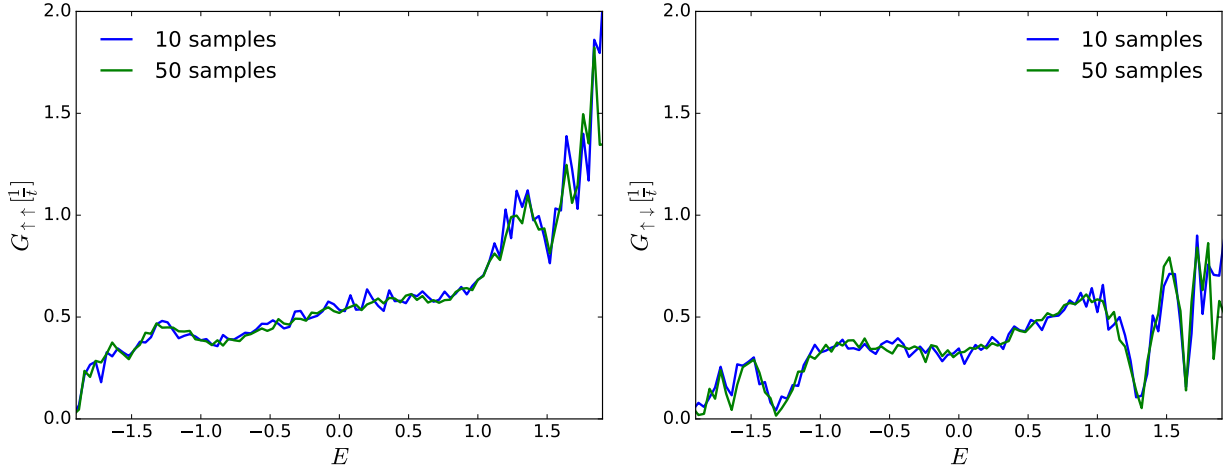


Figure 4.6: (left) Diagonal spin component of the Green's function across the chain,  $G_{N,\uparrow;0,\uparrow}$ , as a function of energy, in the presence of a random spin-dependent site potential. The chain length is 300 sites and the Green's function is averaged over 10 and 50 realizations of the random potential. (right) The off-diagonal spin component of the Green's function,  $G_{N,\uparrow;0,\downarrow}$ .

Figures 4.6 show the energy dependence of the spin components of the chain's average Green's function when spin-polarized impurities are introduced but no spin-dependent hopping is present. In these simulation,  $N = 200$  and  $V_j = a_j^x \sigma^x + a_j^z \sigma^z$ , where the amplitudes  $a_j^x$  and  $a_j^z$  are randomly and uniformly chosen in the intervals  $[0, 0.01t]$  and  $[0, 0.05t]$ , respectively. Here  $t$  denotes the hopping amplitude in the lattice.

The dependence of the average dc spin pumping current on the length of the chain is shown in Fig. 4.7 for the same random spin-dependent potential. Even after averaging over 300 samples, oscillations over the length due to interference remains. However, a clear exponential decay emerges, with a decay length of 4.5, 2.7, and 2.4 lattice units for the three increasing disorder ranges of  $a_x$  shown in the plot.

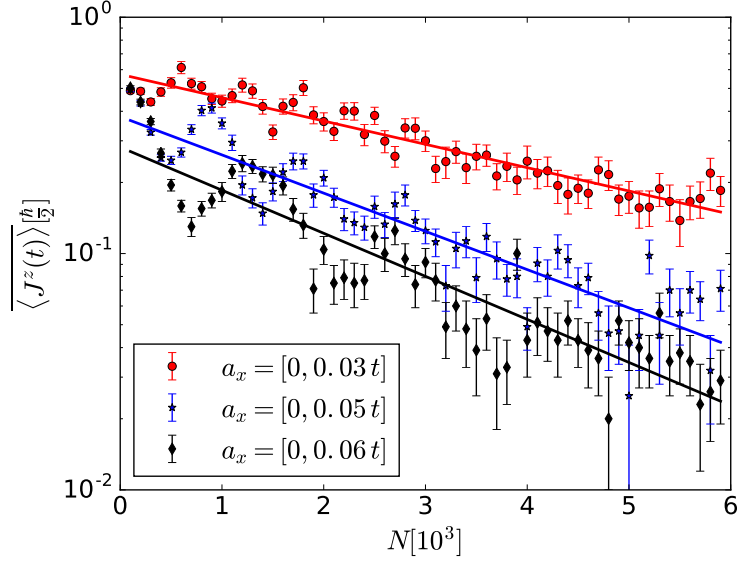


Figure 4.7: Average dc spin current current injected into the reservoir as a function of chain length in the presence of spin-dependent, random on-site potential. The data points are obtained after averaging over 300 samples to minimize quantum interference fluctuations. The solid lines are fittings to the data. The field  $a_z$  varied within the range  $[0, 0.1t]$  while the  $a_x$  field range changed for each data set, as indicated in the legend. The simulations are performed at  $E = 0$  (middle of the band).

### Extension to Two-Dimensional Systems

The spin pumping formulation developed in Secs. 4, 4, and 4 can be extended to 2D systems. To do so, we imagine the magnetic region as a column of magnetic sites whose magnetizations precess in synchronized way, corresponding to a single magnetic domain. The two-dimensional nonmagnetic region is sliced into  $N$  columns and connected to a reservoir, see Fig. 4.8. We keep the same notation used for the one-dimensional finite-chain case and write the Hamiltonians of the different regions as

$$\mathcal{H}_{\text{mag}} = -\frac{J}{2} \mathbf{M}(t) \mathbf{a}^\dagger (\boldsymbol{\sigma} \otimes \mathbf{I}_M) \mathbf{a} \quad (4.116)$$

for the magnetic region,

$$\begin{aligned} \mathcal{H}_{\text{sheet}} = & - \sum_{j=1}^{N-1} \left( \mathbf{c}_{j+1}^\dagger \boldsymbol{\tau}_j \mathbf{c}_j + \mathbf{c}_j^\dagger \boldsymbol{\tau}_j^\dagger \mathbf{c}_{j+1} \right) \\ & + \sum_{j=1}^N \mathbf{c}_j^\dagger \mathbf{V}_j \mathbf{c}_j \end{aligned} \quad (4.117)$$

for the nonmagnetic region, and

$$\mathcal{H}_{\text{res}} = - \sum_{\lambda, \eta} \sum_s T_{\lambda\eta} d_{\lambda,s}^\dagger d_{\eta,s} \quad (4.118)$$

for the reservoir. The Hamiltonians describing the coupling between magnetic and nonmagnetic regions (hereafter referred as sheet), and between the nonmagnetic region and the reservoir are given by

$$\mathcal{H}_{\text{mag-sheet}} = - \left( \mathbf{a}^\dagger \boldsymbol{\gamma}_0 \mathbf{c}_1 + \mathbf{c}_1^\dagger \boldsymbol{\gamma}_0^\dagger \mathbf{a} \right) \quad (4.119)$$

and

$$\mathcal{H}_{\text{sheet-res}} = - \left( \mathbf{c}_N^\dagger \boldsymbol{\gamma}_\alpha \mathbf{d}_\alpha + \mathbf{d}_\alpha^\dagger \boldsymbol{\gamma}_\alpha^\dagger \mathbf{c}_N \right), \quad (4.120)$$

respectively, where  $\mathbf{a}^\dagger = \begin{pmatrix} a_1 & a_2 & \dots & a_M \end{pmatrix}$  is the particle operator at the column containing the magnetic region ( $j = 0$ ),  $\boldsymbol{\gamma}_0$  is a  $2L \times 2L$  matrix that describes the coupling between the magnetic region and the sheet,  $\mathbf{c}_j^\dagger = \begin{pmatrix} c_{j,1} & c_{j,2} & \dots & c_{j,d_j} \end{pmatrix}$  is the particle operator at the  $j$ th sheet slice, which is connected to the neighboring  $j + 1$ -th slice by the matrix  $\boldsymbol{\tau}_i$ ,  $d_j$  is the number of sites in  $j$ th slice, and  $\boldsymbol{\gamma}_\alpha$  is coupling matrix between the  $N$ th sheet slice and the reservoir. Finally, the particle operator acting on the sites in reservoir that are connected directly to the sheet is given by  $\mathbf{d}_\alpha^\dagger = \begin{pmatrix} d_{\alpha,1} & d_{\alpha,2} & \dots & d_{\alpha,d_\alpha} \end{pmatrix}$ .



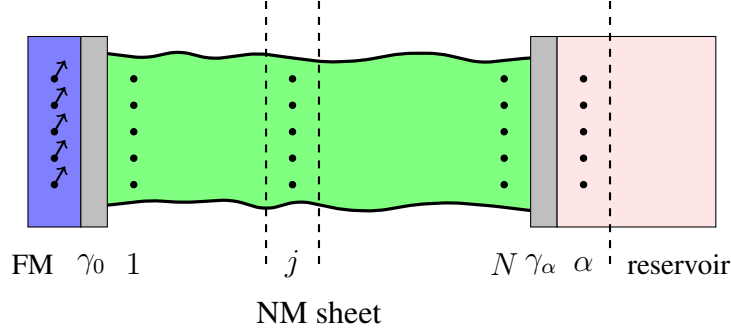


Figure 4.8: The two-dimensional FM/NM/reservoir system. The magnetic region comprises a column of sites whose magnetizations are synchronized. The nonmagnetic sheet is decomposed in  $N$  slices.

The equations of motion read

$$\dot{\mathbf{a}}(t) = i\Omega_{\parallel}(\sigma_z \otimes I_M) \mathbf{a}(t) + i\Omega_{\perp} [(\sigma^+ \otimes I_M) e^{i\Omega t} + (\sigma^- \otimes I_M) e^{-i\Omega t}] \mathbf{a}(t) + i\gamma_0 \mathbf{c}_1(t) \quad (4.121)$$

$$\dot{\mathbf{c}}_1(t) = -i\mathbf{V}_1 + i\gamma_0^{\dagger} \mathbf{a} + i\tau_1 \mathbf{c}_2(t), \quad (4.122)$$

$\vdots$

$$\dot{\mathbf{c}}_j(t) = -i\mathbf{V}_j + i\tau_{j-1}^{\dagger} \mathbf{c}_{j-1} + i\tau_j \mathbf{c}_{j+1}(t), \quad (4.123)$$

$\vdots$

$$\dot{\mathbf{c}}_N(t) = -i\mathbf{V}_N + i\tau_N^{\dagger} \mathbf{c}_{N-1}(t) + i\gamma_{\alpha} \mathbf{d}_{\alpha}(t), \quad (4.124)$$

and

$$\dot{\mathbf{d}}_{\alpha}(t) = i\gamma_{\alpha} \mathbf{c}_N(t) + i \sum_{\nu} T_{\alpha\nu} \mathbf{d}_{\nu}(t). \quad (4.125)$$

The Fourier transforms of the equations of motion result in expressions similar those obtained in

Sec. 4, namely,

$$[(\omega\sigma_0 - \Omega_{\parallel}\sigma_z) \otimes I_M] \mathbf{a}(\omega) - \int \mathcal{H}_1(\omega, \omega') \mathbf{a}(\omega) = -\boldsymbol{\tau}_M \mathbf{c}_1(\omega), \quad (4.126)$$

$$\omega \mathbf{c}_1(\omega) = \mathbf{V}_1 - \boldsymbol{\gamma}_0^\dagger \mathbf{a} - \boldsymbol{\tau}_1 \mathbf{c}_2(\omega), \quad (4.127)$$

$\vdots$

$$\omega \mathbf{c}_j(\omega) = \mathbf{V}_j - \boldsymbol{\tau}_{j-1}^\dagger \mathbf{c}_{j-1} - \boldsymbol{\tau}_j \mathbf{c}_{j+1}, \quad (4.128)$$

$\vdots$

$$\omega \mathbf{c}_N(\omega) = \mathbf{V}_N - \boldsymbol{\tau}_{N-1}^\dagger \mathbf{c}_{N-1} - \boldsymbol{\gamma}_\alpha \mathbf{d}_\alpha, \quad (4.129)$$

and

$$\mathbf{d}_\alpha(\omega) = \mathbf{h}(\omega) - \mathbf{g}_{\alpha\alpha}^r \boldsymbol{\gamma}_\alpha^\dagger(\omega) \mathbf{c}_N(\omega), \quad (4.130)$$

where  $\mathbf{h}$  is a vector with dimension of the surface sites  $\alpha$  in the reservoir and the Green's function of the decoupled reservoir for slice  $\alpha$  reads

$$[\mathbf{g}_{\alpha\alpha}^r]_{i,i'}(t-t') = -i\theta(t-t') \sum_n \phi_n^*(\alpha_i) \phi_n(\alpha_{i'}) e^{-iE_n(t-t')}. \quad (4.131)$$

In order to expand the Green's function in powers of  $\Omega_\perp$ , we notice that, in spin space,

$$\mathcal{H}'_{j,j'} = \delta_{j,j'} \delta_{j,0} \Omega_\perp \begin{pmatrix} 0 & \delta(\omega' - \omega - \Omega) \\ \delta(\omega' - \omega + \Omega) & 0 \end{pmatrix}, \quad (4.132)$$

which leads us to analogous relations to those derived in Sec. 4 for the finite chain.

In order to calculate the spin current along the sheet, we can use an expression identical to that

introduced in Sec. 4, namely,

$$J_j^z(\omega) = \frac{i}{2} \int \frac{d\omega'}{2\pi} \left[ \mathbf{c}_j^\dagger(\omega') (\sigma^z \otimes I_{d_j}) \boldsymbol{\tau}_{j-1}^\dagger \mathbf{c}_{j-1}(\omega' + \omega) - \mathbf{c}_{j-1}^\dagger(\omega' - \omega) \boldsymbol{\tau}_{j-1}^\dagger (\sigma^z \otimes I_{d_j}) \mathbf{c}_j(\omega') \right]. \quad (4.133)$$

The only difference between this relation and Eq. (4.39) is that here there is an implicit sum over transverse sites. Using the orthogonality relation of  $\mathbf{h}(\omega)$  one can derive an expression for the expectation value of the total spin current between the  $(j-1)$ th and  $j$ th slices as

$$\langle J_j^z(\omega) \rangle = \frac{i}{4\pi} \int d\omega' \int d\omega'' \text{Tr} [\mathcal{M}_{ss'}(\omega, \omega', \omega'')] \quad (4.134)$$

where the trace is over spin and transverse site variables,

$$\begin{aligned} \mathcal{M}_{ss'}(\omega, \omega', \omega'') &= \left[ \gamma_\alpha^\dagger \mathbf{G}_{N;j}^a(\omega'', \omega) (\sigma^z \otimes I_{d_j}) \boldsymbol{\tau}_{j-1}^\dagger \mathbf{G}_{j-1;N}^r(\omega + \omega', \omega'') \gamma_\alpha \mathbf{I}(\omega'') \right. \\ &\quad \left. - \gamma_\alpha^\dagger \mathbf{G}_{N;j-1}^a(\omega'', \omega) \boldsymbol{\tau}_{j-1} (\sigma^z \otimes I_{d_j}) \mathbf{G}_{j-1;N}^r(\omega + \omega', \omega'') \gamma_\alpha \mathbf{I}(\omega'') \right] \end{aligned} \quad (4.135)$$

and  $\mathbf{G}_{j,j'}^{r(a)}$  denotes the  $2d_j \times 2d_{j'}$  retarded (advanced) Green's function connecting the  $j$  and  $j'$  slices. A detailed derivation of Eq. (4.134) is provided in Appendix A. Equations (4.134) and (4.135) are also main results of this paper.

Similar to the 1D chain, we can go further to calculate the current at the chain-reservoir interface and expand the Green's function harmonics of the precessing frequency  $\Omega$ ,

$$\mathbf{G}(\omega, \omega') = \delta(\omega' - \omega) \mathbf{D}_0(\omega) + \sum_{k \neq 0} \delta(\omega' - \omega - k\Omega) \mathbf{D}_k(\omega), \quad (4.136)$$

to derive

$$\begin{aligned} \overline{\langle J_\alpha^z(t) \rangle} &= \frac{1}{2} \int d\omega \sum_{k \neq 0} [f(\omega + k\Omega) - f(\omega)] \\ &\times \text{Tr} [\boldsymbol{\rho}_\alpha(\omega + k\Omega) \boldsymbol{\gamma}_\alpha \mathbf{D}_{k;N;N}^r(\omega') \boldsymbol{\gamma}_\alpha^\dagger (\boldsymbol{\sigma}^z \otimes \mathbf{I}_L) \boldsymbol{\rho}_\alpha(\omega) \boldsymbol{\gamma}_\alpha \mathbf{D}_{-k;N;N}^a(\omega' + k\Omega) \boldsymbol{\gamma}_\alpha^\dagger] \end{aligned} \quad (4.137)$$

The formalism developed in this section has several advantages over the scattering formulation: (i) The detailed geometry of the FM/NM systems and physical properties of the NM can be taken into account by computing the appropriate Green's function. (ii) Since the final expression for the spin current is written in terms of the surface Green's functions, the recursive Green's function technique [27] can be utilized for an efficient computational approach to the problem. (iii) Furthermore, since a spatial representation of the system is used in this formalism, systems with higher dimension and arbitrary geometry can be readily simulated.

## Summary and Discussion

In this Chapter we developed an atomistic model of spin pumping in hybrid ferromagnetic heterostructures. The spin current expression is given in terms of the Green's function of the nonmagnetic portion. Motivated by the fact that, in experimental settings, the time-dependent component of the driving magnetic field is small and slow, we use a perturbative expansion to obtain a relation between the mixing conductance and the physical properties of spin-carrying medium. Among the advantages of this formalism are: (i) it provides a framework for including the atomic structure and geometry of the heterostructure, as well as local disorder and spin-orbit coupling mechanism; (ii) it yields an expression for the spin current in terms of Green's function, which can be computed using efficient recursive computational methods; (iii) it allows to model spin relaxation and the ferromagnet-nonmagnetic metal interface; and (iv) when applied to graphene, it is not limited to

high doping.

In a future work we plan to apply this new computational tool to study dynamical spin injection in realistic ferromagnet-graphene heterostructures, and to extend the calculations to include a determination of the spin-Hall voltage across the graphene channel when spin-orbit coupling is included.

## **APPENDIX A: SUPPLEMENTARY MATERIALS**

## Reservoir Green's Function

The retarded Green's function of the decoupled reservoir is defined as

$$g_{\lambda\eta}^r(t, t') = -i\theta(t - t') \langle \{d_\lambda^\dagger(t), d_\eta(t')\} \rangle. \quad (\text{A.1})$$

Expanding the field operators in terms of single-particle energy eigenfunctions

$$d_\lambda(t) = \sum_n \phi_n(\lambda) d_n(t) = \sum_n \phi_n(\lambda) e^{-iE_n t} d_n(0), \quad (\text{A.2})$$

the retarded Green's function of reservoir can be written as

$$g_{\lambda\eta}^r(t, t') = -i\theta(t - t') \sum_n \phi_m^*(\lambda) \phi_n(\eta) e^{iE_n(t-t')}. \quad (\text{A.3})$$

## Noise-Like Correlator

We can rewrite the correlation function of the noise-like term in frequency space in terms of the fermionic operators in time using Eq (4.19),

$$\langle h_s^\dagger(\omega) h_{s'}(\omega') \rangle = \int_{-\infty}^{\infty} dt \int_{-\infty}^{\infty} dt' e^{-i(\omega t - \omega' t')} \langle h_\alpha^\dagger(t) h_{\alpha'}(t') \rangle \quad (\text{A.4})$$

$$\begin{aligned} &= \sum_{\eta, \eta'} \int_{-\infty}^{\infty} dt \int_{-\infty}^{\infty} dt' e^{-i(\omega t - \omega' t')} [g_{\alpha\eta}^r(t - t_0)]^* g_{\alpha\eta'}^r(t' - t_0) \\ &\times \langle d_{\eta, s}^\dagger(t_0) d_{\eta', s'}(t_0) \rangle. \end{aligned} \quad (\text{A.5})$$

After substituting the expansion of decoupled reservoir's Green's function in term of the reservoir's eigenfunction, Eq. (4.20), we get

$$\begin{aligned} \langle h_s^\dagger(\omega) h_{s'}(\omega') \rangle &= \sum_{\eta, \lambda} \sum_{n, m} \phi_n(\alpha) \phi_n^*(\eta) \phi_m^*(\alpha) \phi_m(\eta') \langle d_{\eta, s}^\dagger(t_0) d_{\eta', s'}(t_0) \rangle \\ &\times \int_{t_0}^{\infty} dt e^{-i(\omega - E_n)t} \int_{t_0}^{\infty} dt' e^{-i(E_m - \omega')t'}. \end{aligned} \quad (\text{A.6})$$

Using the reservoir's eigenfunction basis,

$$d_{\eta, s}(t_0) = \sum_n \phi_n(\eta) d_{n, s}(t_0), \quad (\text{A.7})$$

and the orthogonality of the reservoir's eigenfunctions, we obtain

$$\begin{aligned} \langle h_s^\dagger(\omega) h_{s'}(\omega') \rangle &= \sum_{n, m} \phi_n(\alpha) \phi_m^*(\alpha) \langle d_{n, s}^\dagger(t_0) d_{m, s'}(t_0) \rangle \\ &\times \int_{t_0}^{\infty} dt e^{-i(\omega - E_n)t} \int_{t_0}^{\infty} dt' e^{-i(E_m - \omega')t'}. \end{aligned} \quad (\text{A.8})$$

Using Eq. (4.21) and taking the limit  $t_0 \rightarrow -\infty$  we arrive at Eq. (4.56).

For 2D systems, the correlation function  $\langle \mathbf{h}_{s_1}^\dagger(\omega_1) \mathbf{h}_{s_2}(\omega_2) \rangle$  can be obtained in the same way:

$$\langle h_{s_1, i_1}^\dagger(\omega_1) h_{s_2, i_2}(\omega_2) \rangle = \int_{-\infty}^{\infty} dt_1 \int_{-\infty}^{\infty} dt_2 e^{-i(\omega_1 t_1 - \omega_2 t_2)} \langle h_{s_1, i_1}^\dagger(t_1) h_{s_2, i_2}(t_2) \rangle \quad (\text{A.9})$$

$$\begin{aligned} &= \sum_{\eta_1, \eta_2} \int_{-\infty}^{\infty} dt_1 \int_{-\infty}^{\infty} dt_2 e^{-i(\omega_1 t_1 - \omega_2 t_2)} \left[ g_{\alpha_{i_1} \eta_1}^r(t_1 - t_0) \right]^* g_{\alpha_{i_2} \eta_2}^r(t_2 - t_0) \\ &\times \langle d_{\eta_1, s_1}^\dagger(t_0) d_{\eta_2, s_2}(t_0) \rangle \end{aligned} \quad (\text{A.10})$$

$$\begin{aligned} &= \sum_{\eta_1, \eta_2} \sum_{n_1, n_2} \phi_{n_1}(\alpha_{i_1}) \phi_{n_1}^*(\eta_1) \phi_{n_2}^*(\alpha_{i_2}) \phi_{n_2}(\eta_2) \langle d_{\eta_1, s_1}^\dagger(t_0) d_{\eta_2, s_2}(t_0) \rangle \\ &\times \int_{t_0}^{\infty} dt_1 e^{-i(\omega_1 - E_{n_1})t_1} \int_{t_0}^{\infty} dt_2 e^{-i(E_{n_2} - \omega_2)t_2}. \end{aligned} \quad (\text{A.11})$$



Using the orthonormal set of eigenfunctions of the reservoir,

$$d_{\eta,s}(t_0) = \sum_n \phi_n(\eta) d_{n,s}(t_0), \quad (\text{A.12})$$

we can write

$$\begin{aligned} \langle h_{s_1, i_1}^\dagger(\omega_1) h_{s_2, i_2}(\omega_2) \rangle &= \sum_{n_1, n_2} \phi_{n_1}(\alpha_{i_1}) \phi_{n_2}^*(\alpha_{i_2}) \langle d_{n_1, s_1}^\dagger(t_0) d_{n_2, s_2}(t_0) \rangle \\ &\times \int_{t_0}^{\infty} dt_1 e^{-i(\omega_1 - E_{n_1})t_1} \int_{t_0}^{\infty} dt_2 e^{-i(E_{n_2} - \omega_2)t_2} \end{aligned} \quad (\text{A.13})$$

$$= \delta(\omega_1 - \omega_2) \delta_{s_1, s_2} \sum_{n_1} \phi_{n_1}(\alpha_{i_1}) \phi_{n_1}^*(\alpha_{i_2}) \delta(\omega_1 - E_{n_1}) \quad (\text{A.14})$$

when we set  $t_0 \rightarrow \infty$ . We finally arrive at

$$\langle \mathbf{h}_{s_1}^\dagger(\omega_1) \mathbf{h}_{s_2}(\omega_2) \rangle = \delta_{s_1, s_2} \delta(\omega_1 - \omega_2) \mathbf{I}_\alpha(\omega_1), \quad (\text{A.15})$$

where  $\mathbf{I}_\alpha(\omega) = \boldsymbol{\rho}_\alpha(\omega) f(\omega)$  and  $\boldsymbol{\rho}_\alpha(\omega)$  is the density of states matrix at the  $\alpha$  slice,

$$[\boldsymbol{\rho}_\alpha]_{i_1, i_2} = \sum_{n_1} \sum_{n_1} \phi_{n_1}(\alpha_{i_1}) \phi_{n_1}^*(\alpha_{i_2}) \delta(\omega_1 - E_{n_1}). \quad (\text{A.16})$$

### $s$ -Component of the Spin Current

Substituting Eq. (4.48) into Eq. (4.46), we obtain

$$\begin{aligned}
\langle J_s(\omega) \rangle &= \frac{i\gamma}{2} \int \frac{d\omega'}{2\pi} \langle \{ h_s^\dagger(\omega') - \gamma [g_{\alpha\alpha}^r(\omega')]^* a_s^\dagger(\omega') \} a_s(\omega' + \omega) \\
&\quad - a_s^\dagger(\omega') [h_s(\omega' + \omega) - \gamma g_{\alpha\alpha}^r(\omega' + \omega) a_s(\omega' + \omega)] \rangle \\
&= \frac{i\gamma}{2} \int \frac{d\omega'}{2\pi} ( [\langle h_s^\dagger(\omega') a_s(\omega' + \omega) \rangle - \langle a_s^\dagger(\omega') h_s(\omega' + \omega) \rangle] \\
&\quad - \gamma \langle a_s^\dagger(\omega') a_s(\omega' + \omega) \rangle \{ [g_{\alpha\alpha}^r(\omega')]^* - g_{\alpha\alpha}^r(\omega' + \omega) \} ). \tag{A.17}
\end{aligned}$$

Employing Eq. (4.54), we can derive the following relations:

$$\langle h_s^\dagger(\omega') a_s(\omega) \rangle = -\gamma G_{ss}^r(\omega, \omega') I_\alpha(\omega'), \tag{A.18}$$

$$\langle a_s^\dagger(\omega') h_s(\omega' + \omega) \rangle = -\gamma G_{ss}^r(\omega', \omega' + \omega) I(\omega' + \omega), \tag{A.19}$$

and

$$\langle a_s^\dagger(\omega') a_s(\omega) \rangle = \gamma^2 \sum_{s'} \int d\omega'' [G_{ss'}^r(\omega', \omega'')]^* G_{ss'}^r(\omega, \omega'') I_\alpha(\omega''). \tag{A.20}$$

Putting these relations together with Eq. (A.17) one arrives at Eq. (4.59).

## Spin Current for 2D Systems

The fermionic particle operator in terms of the system Green's function reads

$$\mathbf{c}_{j,s}^\dagger(\omega) = - \sum_{s';m,n} d\omega' h_{ns'}^\dagger(\omega_1) \gamma_{n,m}^* \times \left[ G_{N,m,s';j,1,s}(\omega_1, \omega) \quad G_{N,m,s';j,2,s}(\omega_1, \omega) \quad \dots \quad G_{N,m,s';j,d_j,s}(\omega_1, \omega) \right], \quad (\text{A.21})$$

where  $d_j$  is the number of sites in the slice  $j$ . After substituting it into the current expression

$$J_j^z(\omega) = \frac{i}{2} \int \frac{d\omega'}{2\pi} \left[ \mathbf{c}_j^\dagger(\omega') (\sigma^z \otimes I_{d_j}) \boldsymbol{\tau}_{j-1}^\dagger \mathbf{c}_{j-1}(\omega' + \omega) - \mathbf{c}_{j-1}^\dagger(\omega') \boldsymbol{\tau}_{j-1} (\sigma^z \otimes I_{d_j}) \mathbf{c}_j(\omega' + \omega) \right], \quad (\text{A.22})$$

the expectation value of the first term in Eq. (A.22) becomes

$$\frac{i}{2} \int \frac{d\omega'}{2\pi} \sum_{s_1,s_2} \sum_{n,n';m,m'} \int d\omega_1 \gamma_{m',m}^* \left[ G_{N,m,s_1;j,1}^a(\omega_1, \omega) \quad G_{N,m,s_1;j,2}^a(\omega_1, \omega) \quad \dots \quad G_{N,m,s_1;j,d_j}^a(\omega_1, \omega) \right] \times \left[ (\sigma^z \otimes I_{d_j}) \boldsymbol{\tau}_{j-1}^\dagger \right] \int d\omega_2 \begin{bmatrix} G_{j-1,1;N,n,s_2}^r(\omega' + \omega, \omega_2) \\ G_{j-1,2;N,n,s_2}^r(\omega' + \omega, \omega_2) \\ \vdots \\ G_{j-1,d_j;N,n,s_2}^r(\omega' + \omega, \omega_2) \end{bmatrix} \gamma_{n,n'} \langle h_{m',s_1}^\dagger(\omega_1) h_{n',s_2}(\omega_2) \rangle. \quad (\text{A.23})$$

By applying the  $h_{m,s}(\omega)$  correlator we find

$$\langle J_j^z(\omega) \rangle = \frac{i}{2} \int \frac{d\omega'}{2\pi} \int d\omega_1 \text{Tr} \left[ \gamma_\alpha^\dagger \mathbf{G}_{N;j}^a(\omega_1, \omega) (\sigma^z \otimes \mathbf{I}_{d_j}) \boldsymbol{\tau}_{j-1}^\dagger \mathbf{G}_{j-1;N}^r(\omega + \omega', \omega_1) \gamma_\alpha \mathbf{I}(\omega_1) \right] - \frac{i}{2} \int \frac{d\omega'}{2\pi} \int d\omega_1 \text{Tr} \left[ \gamma_\alpha^\dagger \mathbf{G}_{N;j-1}^a(\omega_1, \omega) \boldsymbol{\tau}_{j-1} (\sigma^z \otimes \mathbf{I}_{d_j}) \mathbf{G}_{j-1;N}^r(\omega + \omega', \omega_1) \gamma_\alpha \mathbf{I}(\omega_1) \right]. \quad (\text{A.24})$$

We can follow the same approach to calculate the current at the chain-reservoir interface:

$$J_\alpha^z(\omega) = \frac{i}{2} \int \frac{d\omega'}{2\pi} \left[ \mathbf{d}^\dagger(\omega')(\sigma_z \otimes \mathbf{I}_L) \gamma_\alpha \mathbf{c}_N(\omega' + \omega) - \mathbf{c}_N^\dagger(\omega') \gamma_\alpha^\dagger (\sigma_z \otimes \mathbf{I}_L) \mathbf{d}_s(\omega' + \omega) \right]. \quad (\text{A.25})$$

The current expression can be written as

$$J_\alpha^z(\omega) = \frac{i}{2} \int \frac{d\omega'}{2\pi} \left\{ \left[ \mathbf{h}^\dagger(\omega') - \mathbf{c}_N^\dagger(\omega') \gamma_\alpha^\dagger \mathbf{g}_{\alpha\alpha}^a(\omega') \right] (\sigma_z \otimes \mathbf{I}_L) \gamma_\alpha \mathbf{c}_N(\omega' + \omega) - \mathbf{c}_N^\dagger(\omega') \gamma_\alpha^\dagger (\sigma_z \otimes \mathbf{I}_L) \left[ \mathbf{h}(\omega' + \omega) - \mathbf{g}_{\alpha\alpha}^r(\omega' + \omega) \gamma_\alpha \mathbf{c}_N(\omega' + \omega) \right] \right\}, \quad (\text{A.26})$$

which can be simplified to

$$J_\alpha^z(\omega) = \frac{i}{2} \int \frac{d\omega'}{2\pi} \left[ \mathbf{h}^\dagger(\omega')(\sigma_z \otimes \mathbf{I}_L) \gamma_\alpha \mathbf{c}_N(\omega' + \omega) - \mathbf{c}_N^\dagger(\omega') \gamma_\alpha^\dagger (\sigma_z \otimes \mathbf{I}_L) \mathbf{h}(\omega' + \omega) \right] - \frac{i}{2} \int \frac{d\omega'}{2\pi} \mathbf{c}_N^\dagger(\omega') \gamma_\alpha^\dagger \left[ \mathbf{g}_{\alpha\alpha}^a(\omega') - \mathbf{g}_{\alpha\alpha}^r(\omega' + \omega) \right] (\sigma_z \otimes \mathbf{I}_L) \gamma_\alpha \mathbf{c}_N(\omega' + \omega). \quad (\text{A.27})$$

After substituting the fermionic operator in terms of the system's Green's function, the expectation value of the spin current becomes

$$\begin{aligned} \langle J_\alpha^z(\omega) \rangle &= \frac{i}{2} \int \frac{d\omega'}{2\pi} \left\{ \text{Tr} \left[ \mathbf{I}_\alpha(\omega' + \omega) \gamma_\alpha (\sigma_z \otimes \mathbf{I}_L) \mathbf{G}_{N;N}^a(\omega', \omega' + \omega) \gamma_\alpha^\dagger \right] \right. \\ &\quad \left. - \text{Tr} \left[ \mathbf{I}_\alpha(\omega') \gamma_\alpha (\sigma_z \otimes \mathbf{I}_L) \mathbf{G}_{N;N}^r(\omega' + \omega, \omega') \gamma_\alpha^\dagger \right] \right\} \\ &\quad + \frac{i}{2} \int \frac{d\omega'}{2\pi} \text{Tr} \left\{ \mathbf{I}_\alpha(\omega'') \gamma_\alpha \mathbf{G}_{N;N}^a(\omega', \omega'') \gamma_\alpha^\dagger \left[ \mathbf{g}_{\alpha\alpha}^r(\omega' + \omega) - \mathbf{g}_{\alpha\alpha}^a(\omega') \right] \right. \\ &\quad \left. \times (\sigma_z \otimes \mathbf{I}_L) \gamma_\alpha \mathbf{G}_{N;N}^r(\omega' + \omega, \omega'') \gamma_\alpha^\dagger \right\} \end{aligned} \quad (\text{A.28})$$

Similar to the 1D case, we expand the Green's function in terms of the frequency difference,

$$G(\omega, \omega') = \delta(\omega' - \omega) D_0(\omega) + \sum_{k \neq 0} \delta(\omega' - \omega - k\Omega) D_k(\omega), \quad (\text{A.29})$$

and following the same approach used in the 1D case, we get

$$\begin{aligned}
\langle J_\alpha^z \rangle &= \frac{i}{2} \delta(\omega) \int \frac{d\omega'}{2\pi} \text{Tr} \left\{ \mathbf{I}_\alpha(\omega') \gamma_\alpha (\sigma_z \otimes \mathbf{I}_L) [\mathbf{D}_{0;N;N}^a(\omega') - \mathbf{D}_{0;N;N}^r(\omega')] \gamma_\alpha^\dagger \right\} \\
&+ \frac{i}{2} \delta(\omega) \int \frac{d\omega'}{2\pi} \text{Tr} \left\{ \mathbf{I}_\alpha(\omega') \gamma_\alpha \mathbf{D}_{0;N;N}^a(\omega') \gamma_\alpha^\dagger [\mathbf{g}_{\alpha\alpha}^r(\omega') - \mathbf{g}_{\alpha\alpha}^a(\omega')] \right. \\
&\quad \left. (\sigma_z \otimes \mathbf{I}_L) \gamma_\alpha \mathbf{D}_{0;N;N}^r(\omega') \gamma_\alpha^\dagger \right\} \\
&+ \frac{i}{2} \delta(\omega) \int \frac{d\omega'}{2\pi} \sum_{k \neq 0} \text{Tr} \left\{ \mathbf{I}_\alpha(\omega' - k\Omega) \gamma_\alpha \mathbf{D}_{k;N;N}^a(\omega' - k\Omega) \gamma_\alpha^\dagger [\mathbf{g}_{\alpha\alpha}^r(\omega') - \mathbf{g}_{\alpha\alpha}^a(\omega')] \right. \\
&\quad \left. \times (\sigma_z \otimes \mathbf{I}_L) \gamma_\alpha \mathbf{D}_{-k;N;N}^r(\omega') \gamma_\alpha^\dagger \right\}
\end{aligned} \tag{A.30}$$

which leads to

$$\begin{aligned}
\langle J_\alpha^z \rangle &= -\frac{i}{2} \delta(\omega) \int \frac{d\omega'}{2\pi} \sum_{k \neq 0} \text{Tr} \left\{ \mathbf{I}_\alpha(\omega') \gamma_\alpha \mathbf{D}_{k;N;N}^r(\omega') \gamma_\alpha^\dagger [\mathbf{g}_{\alpha\alpha}^r(\omega' + k\Omega) - \mathbf{g}_{\alpha\alpha}^a(\omega' + k\Omega)] \right. \\
&\quad \left. \times (\sigma_z \otimes \mathbf{I}_L) \gamma_\alpha \mathbf{D}_{-k;N;N}^a(\omega' + k\Omega) \gamma_\alpha^\dagger \right\} \\
&+ \frac{i}{2} \delta(\omega) \int \frac{d\omega'}{2\pi} \sum_{k \neq 0} \text{Tr} \left\{ \mathbf{I}_\alpha(\omega' + k\Omega) \gamma_\alpha \mathbf{D}_{k;N;N}^r(\omega') \gamma_\alpha^\dagger [\mathbf{g}_{\alpha\alpha}^r(\omega') - \mathbf{g}_{\alpha\alpha}^a(\omega')] \right. \\
&\quad \left. \times (\sigma_z \otimes \mathbf{I}_L) \gamma_\alpha \mathbf{D}_{-k;N;N}^a(\omega' + k\Omega) \gamma_\alpha^\dagger \right\},
\end{aligned} \tag{A.31}$$

leading to

$$\begin{aligned}
\overline{\langle J_\alpha^z(t) \rangle} &= \frac{1}{2} \int d\omega \sum_{k \neq 0} [f(\omega + k\Omega) - f(\omega)] \\
&\quad \times \text{Tr} \left[ \boldsymbol{\rho}_\alpha(\omega + k\Omega) \gamma_\alpha \mathbf{D}_{k;N;N}^r(\omega') \gamma_\alpha^\dagger (\sigma^z \otimes \mathbf{I}_L) \boldsymbol{\rho}_\alpha(\omega) \right. \\
&\quad \left. \gamma_\alpha \mathbf{D}_{-k;N;N}^a(\omega' + k\Omega) \gamma_\alpha^\dagger \right].
\end{aligned} \tag{A.32}$$

## LIST OF REFERENCES

- [1] R. Tsuchikawa, D. Heligman, B. T. Blue, Z. Y. Zhang, A. Ahmadi, E. R. Mucciolo, J. Hone, and M. Ishigami. Scattering strength of potassium on a carbon nanotube with known chirality. *Phys. Rev. B*, 94:045408, 2016.
- [2] A. B. Fowler, F. Fang, W. E. Howard, and P. J. Stiles. Magneto-oscillatory conductance in silicon surfaces. *Phys. Rev. Lett.*, 16(20):901, 1966.
- [3] K. S. Novoselov, A. K. Geim, S. V. Morozov, D. Jiang, Y. Zhang, S. V. Dubonos, I. V. Grigorieva, and A. A. Firsov. Electric field effect in atomically thin carbon films. *Science*, 306(5696):666–669, 2004.
- [4] S. Iijima. Helical microtubules of graphitic carbon. *Nature*, 354(6348):56, 1991.
- [5] T. W. Odom, J. L. Huang, P. Kim, and C. M. Lieber. Atomic structure and electronic properties of single-walled carbon nanotubes. *Nature*, 391(6662):62–64, 1998.
- [6] P. G. Collins, K. Bradley, M. Ishigami, and A. Zettl. Extreme oxygen sensitivity of electronic properties of carbon nanotubes. *Science*, 287(5459):1801–1804, 2000.
- [7] R. Landauer. Irreversibility and heat generation in the computing process. *IBM J. Res. Dev.*, 5(3):183–191, 1961.
- [8] A. Brataas, Y. Tserkovnyak, G. E. W. Bauer, and B. I. Halperin. Spin battery operated by ferromagnetic resonance. *Phys. Rev. B*, 66:060404, 2002.
- [9] S. Mizukami, Y. Ando, and T. Miyazaki. The study on ferromagnetic resonance linewidth for NM/80NiFe/NM (NM= Cu, Ta, Pd and Pt) films. *Jap. J. Appl. Phys.*, 40(2R):580, 2001.
- [10] E. Saitoh, M. Ueda, H. Miyajima, and G. Tatara. Conversion of spin current into charge current at room temperature: Inverse spin-hall effect. *Appl. Phys. Lett.*, 88(18):182509, 2006.
- [11] A. Azevedo, L. H. Vilela Leo, R. L. Rodriguez-Suarez, A. B. Oliveira, and S. M. Rezende. dc effect in ferromagnetic resonance: Evidence of the spin-pumping effect? *J. Appl. Phys.*, 97(10), 2005.

- [12] B. Heinrich, C. Burrowes, E. Montoya, B. Kardasz, E. Girt, Y. Song, Y. Sun, and M. Wu. Spin pumping at the magnetic insulator (YIG)/normal metal (Au) interfaces. *Phys. Rev. Lett.*, 107(6):066604, 2011.
- [13] O. Mosendz, J. Pearson, F. Fradin, G. E. W. Bauer, S. Bader, and A. Hoffmann. Quantifying spin hall angles from spin pumping: Experiments and theory. *Phys. Rev. Lett.*, 104(4):046601, 2010.
- [14] A. K. Patra, S. Singh, B. Barin, Y. Lee, J.-H. Ahn, E. del Barco, E. R. Mucciolo, and B. zyilmaz. Dynamic spin injection into chemical vapor deposited graphene. *Appl. Phys. Lett.*, 101(16), 2012.
- [15] Y. Tserkovnyak, A. Brataas, and G. E. W. Bauer. Enhanced gilbert damping in thin ferromagnetic films. *Phys. Rev. Lett.*, 88:117601, 2002.
- [16] A. Brataas, Y. Tserkovnyak, and G. E. W. Bauer. Scattering theory of gilbert damping. *Phys. Rev. Lett.*, 101:037207, 2008.
- [17] S. Singh, A. Ahmadi, C. T. Cherian, E. R. Mucciolo, E. del Barco, and B. zyilmaz. Dynamical spin injection at a quasi-one-dimensional ferromagnet-graphene interface. *Appl. Phys. Lett.*, 106(3), 2015.
- [18] L. X. Benedict, S. G. Louie, and M. L. Cohen. Static polarizabilities of single-wall carbon nanotubes. *Phys. Rev. B*, 52:8541–8549, 1995.
- [19] K. Sasaki. Charge screening effect in metallic carbon nanotubes. *Phys. Rev. B*, 65:195412, 2002.
- [20] P. Kim, T. W. Odom, J. L. Huang, and C. M. Lieber. Electronic density of states of atomically resolved single-walled carbon nanotubes: Van hove singularities and end states. *Phys. Rev. Lett.*, 82:1225–1228, 1999.
- [21] C. H. Lewenkopf and E. R. Mucciolo. The recursive green’s function method for graphene. *J. Comput. Elect.*, 12(2):203–231, 2013.
- [22] R. Landauer. Spatial variation of currents and fields due to localized scatterers in metallic conduction. *IBM J. Res. Dev.*, 32(3):306–316, 1988.
- [23] M. Büttiker, Y. Imry, R. Landauer, and S. Pinhas. Generalized many-channel conductance formula with application to small rings. *Phys. Rev. B*, 31:6207–6215, 1985.

- [24] D. S. Fisher and P. A. Lee. Relation between conductivity and transmission matrix. *Phys. Rev. B*, 23(12):6851, 1981.
- [25] H. Schomerus. Effective contact model for transport through weakly-doped graphene. *Phys. Rev. B*, 76(4):045433, 2007.
- [26] M. L. Sancho, J. L. Sancho, and J Rubio. Highly convergent schemes for the calculation of bulk and surface green functions. *J. Phys. F: Metal Physics*, 15(4):851, 1985.
- [27] C. H. Lewenkopf and E. R. Mucciolo. The recursive green’s function method for graphene. *J. Comput. Electron.*, 12(2):203–231, 2013.
- [28] J. M. Ziman. *Elements of advanced quantum theory*. Cambridge University Press, 1969.
- [29] R. Saito, G. Dresselhaus, M. S. Dresselhaus, et al. *Physical properties of carbon nanotubes*, volume 35. World Scientific, 1998.
- [30] R. Saito, M. Fujita, G. Dresselhaus, and M. S. Dresselhaus. Electronic structure of graphene tubules based on c60. *Phys. Rev. B*, 46(3):1804, 1992.
- [31] M. Ouyang, J. Huang, C. L. Cheung, and C. M. Lieber. Energy gaps in” metallic” single-walled carbon nanotubes. *Science*, 292(5517):702–705, 2001.
- [32] D. D. Awschalom and M. E. Flatté. Challenges for semiconductor spintronics. *Nat. Phys.*, 3(3):153–159, 2007.
- [33] A. K. Geim and K. S. Novoselov. The rise of graphene. *Nat. Mater.*, 6(3):183–191, 2007.
- [34] R. H. Baughman, A. A. Zakhidov, and W. A. de Heer. Carbon nanotubes—the route toward applications. *Science*, 297(5582):787–792, 2002.
- [35] T. Y. Yang, J. Balakrishnan, F. Volmer, A. Avsar, M. Jaiswal, J. Samm, S. R. Ali, A. Pachoud, M. Zeng, M. Popinciuc, et al. Observation of long spin-relaxation times in bilayer graphene at room temperature. *Phys. Rev. Lett.*, 107(4):047206, 2011.



- [36] D. Huertas-Hernando, F. Guinea, and A. Brataas. Spin-orbit-mediated spin relaxation in graphene. *Phys. Rev. Lett.*, 103:146801, 2009.
- [37] C. L. Kane and E. J. Mele. Quantum spin hall effect in graphene. *Phys. Rev. Lett.*, 95:226801, 2005.
- [38] F. S. M. Guimarães, A. T. Costa, R. B. Muniz, and M. S. Ferreira. Graphene-based spin-pumping transistor. *Phys. Rev. B*, 81:233402, 2010.
- [39] Y. G. Semenov, K. W. Kim, and J. M. Zavada. Spin field effect transistor with a graphene channel. *Appl. Phys. Lett.*, 91(15):153105, 2007.
- [40] M. Moskalets and M. Büttiker. Dissipation and noise in adiabatic quantum pumps. *Phys. Rev. B*, 66:035306, 2002.
- [41] T. Inoue, G. E. W. Bauer, and K. Nomura. Spin pumping into two-dimensional electron systems, 2016.
- [42] M. J. Hurben and C. E. Patton. Theory of two magnon scattering microwave relaxation and ferromagnetic resonance linewidth in magnetic thin films. *J. Appl. Phys.*, 83(8):4344–4365, 1998.
- [43] P. W. Brouwer. Scattering approach to parametric pumping. *Phys. Rev. B*, 58:R10135–R10138, 1998.
- [44] A. Dhar and S. B. Sriram. Quantum transport using the ford-kac-mazur formalism. *Phys. Rev. B*, 67:195405, 2003.
- [45] S. Maekawa, S. O. Valenzuela, E. Saitoh, and T. Kimura. *Spin Current*, volume 17. Oxford University Press, 2012.
- [46] J. Shi, P. Zhang, D. Xiao, and Q. Niu. Proper definition of spin current in spin-orbit coupled systems. *Phys. Rev. Lett.*, 96:076604, 2006.
- [47] E. I. Rashba. Spin currents in thermodynamic equilibrium: The challenge of discerning transport currents. *Phys. Rev. B*, 68(24):241315, 2003.
- [48] I. V. Tokatly. Equilibrium spin currents: non-abelian gauge invariance and color diamagnetism in condensed matter. *Phys. Rev. Lett.*, 101(10):106601, 2008.

- [49] E. B. Sonin. Equilibrium spin currents in the rashba medium. *Phys. Rev. B*, 76(3):033306, 2007.
- [50] E. B. Sonin. Proposal for measuring mechanically equilibrium spin currents in the rashba medium. *Phys. Rev. Lett.*, 99(26):266602, 2007.
- [51] K. Ando, S. Takahashi, J. Ieda, H. Kurebayashi, T. Trypiniotis, C. Barnes, S. Maekawa, and E. Saitoh. Electrically tunable spin injector free from the impedance mismatch problem. *Nat. Mat.*, 10(9):655–659, 2011.
- [52] S. Mizukami, Y. Ando, and T. Miyazaki. Effect of spin diffusion on gilbert damping for a very thin permalloy layer in Cu/permalloy/Cu/Pt films. *Phys. Rev. B*, 66(10):104413, 2002.
- [53] O. Mosendz, J. E. Pearson, F. Y. Fradin, G. E. W. Bauer, S. D. Bader, and A. Hoffmann. Quantifying spin hall angles from spin pumping: Experiments and theory. *Phys. Rev. Lett.*, 104(4):046601, 2010.
- [54] B. Heinrich, Y. Tserkovnyak, G. Woltersdorf, A. Brataas, R. Urban, and G. E. W. Bauer. Dynamic exchange coupling in magnetic bilayers. *Phys. Rev. Lett.*, 90(18):187601, 2003.
- [55] E. Saitoh, H. Ueda, M. and Miyajima, and G. Tatara. Conversion of spin current into charge current at room temperature: Inverse spin-hall effect. *Appl. Phys. Lett.*, 88(18):182509, 2006.
- [56] O. Mosendz, V. Vlaminck, J. E. Pearson, F. Y. Fradin, G. E. W. Bauer, S. D. Bader, and A. Hoffmann. Detection and quantification of inverse spin hall effect from spin pumping in permalloy/normal metal bilayers. *Phys. Rev. B*, 82(21):214403, 2010.
- [57] K. Ando, Y. Kajiwara, S. Takahashi, S. Maekawa, K. Takemoto, M. Takatsu, and E. Saitoh. Angular dependence of inverse spin–hall effect induced by spin pumping investigated in a  $\text{Ni}_{81}\text{Fe}_{19}$  / Pt thin film. *Phys. Rev. B*, 78(1):014413, 2008.
- [58] Z. Tang, E. Shikoh, H. Ago, K. Kawahara, Y. Ando, T. Shinjo, and M. Shiraishi. Dynamically generated pure spin current in single-layer graphene. *Phys. Rev. B*, 87(14):140401, 2013.